DISSERTATION

Titel der Dissertation

Part I: Expression and reconstitution of the
Trypanosoma brucei IFT complex B core

Part II: Structural analysis of the coiled-coil domain of
the cytolinker protein plectin

Verfasserin

Mag.rer.nat. Clara Pleban

angestrebter akademischer Grad

Doktorin der Naturwissenschaften (Dr.rer.nat.)

Wien, 2012

Acknowledgements

First, I want to thank my supervisor **Dr. Gang Dong** for giving me the opportunity to do my PhD studies in his lab. I am deeply grateful for his constant support and guidance during the last 4 years.

I want to thank my fellow lab members **Renping Qiao**, **Keni Vidilaseris**, **Ekaterina Shimanovskaya** and **Johannes Lesigang** for generating a great lab atmosphere.

I want to thank my family – my parents **Eveline** and **Rainer**, my siblings **Karin** and **Clemens** as well as **Linn** and **Flo**. Thanks for your help during the last 4 years and for having the patience to endure me during two times moving.

Thousand thanks to **Elli**, **Fabi**, **Rene**, **Ivan** and **Patti** - for their support, help and time we spent together. You were always there when I needed someone to talk to and cheered me up on a daily basis. Vielen, vielen Dank!

Table of Contents

Part I: Expression and reconstitution of *Trypanosoma brucei* IFT complex B core

Part II: Structural analysis of the coiled-coil domain of the cytolinker protein plectin

Abbreviations

Å	Angstrom
aa	Amino acids
Amp	Ampicillin
β-ME	Beta-mercaptoethanol
b-OG	n-octyl-beta-D-glucoside
Cam	Chloramphenicol
°C	Degree Celsius
Ce	Caenorhabditis elegans
Cr	Chlamydomonas reinhardtii
Da	Dalton
DEER	Double electron-electron resonance
Dm	Drosophila melanogaster
DMBC	Dimethyl-borane complex
DMP	Dimethylpipelimidate
DTT	Dithiothreitol
Dr	Danio rerio
EB (S)	Epidermolysis bullosa (simplex)
EDTA	Ethylenediaminetetraacetic acid
EM	Electron microscopy
EPR	Electron paramagnetic resonance
cw-EPR	Continuous wave EPR
GA	Glutaraldehyde
HIS	Histidine
HD	Hemidesmosomes

Hsp	Heat-shock protein
IFT	Intraflagellar transport
IPTG	Isopropyl β-D-1-thiogalactopyranoside
Kan	Kanamycin
K	Kelvin
kHz	Kilo-Hertz
Mm	Mus musculus
MAP	Microtubule associated protein
MBP	Maltose binding protein
MCS	Multiple cloning cassette
MD	Muscular dystrophy
MS	Mass spectrometry
MTOC	Microtubule organizing center
MTSSL	(1-Oxyl-2,2,5,5-tetramethyl-Δ3-pyrroline-3-methyl) Methane-thiosulfonate
MTS	(1-Acetyl-2,2,5,5-tetramethyl-Δ3-pyrroline-3-methyl Methane-thiosulfonate
NP-40	Nonidet P-40
PAGE	Polyacrylamide gel electrophoresis
PEG	Polyethylene glycol
PKD	Polycystic kidney disease
PMSF	Phenylmethylsulfonyl fluoride
SEC	Size-exclusion chromatography
SDS	Sodium-dodecyl sulfate
SLS	Static light scattering
Sm	Spectinomycin

T	Tesla
Tb	Trypanosoma brucei
TCA	Trichloroacetic acid
TPR	Tetratricopeptide repeat
TRPV	Transient receptor potential vanilloid
WB	Western blot

Part I.

Expression and reconstitution of *Trypanosoma brucei* IFT complex B core

1   Abstract

Having been neglected as a cellular remnant for nearly a century, the cilium has recently attracted immense interest in current research. Because of the essential roles played by cilia in cell sensing and signalling, the numbers of human pathologies associated with ciliary dysfunctions are increasing.

Cilia are microtubule-based structures protruding from the cell surface, encapsulated by the unique ciliary membrane and separated from the cytoplasm by a transition zone. The basis for a functioning cilium is the well-coordinated, bi-directional transport of both ciliary building blocks and turnover products along the microtubule axoneme, which is carried out by large proteinaceous assemblies. These assemblies are termed intraflagellar transport (IFT) particles and are composed of at least 20 different proteins, separated into two distinct sub-populations, termed IFT complex A and IFT complex B, which are respectively responsible for retrograde and anterograde transport within the cilium. The IFT complex B is composed of at least 14 proteins, with eight of them forming a high-ionic strength stable core complex. To characterize these core proteins, I have reconstituted the eight-polypeptide core complex of *Trypanosoma brucei* in a heterologous bacterial expression system. Analysis of the oligomeric state of the recombinant assembly revealed that the proteins are connected in higher order structures. The reconstituted complex is capable of binding liposomes, but the responsible subunit(s) still needs to be elucidated. The purified complex can be used for further biochemical studies and electron microscopy analyses; for crystallographic approaches a eukaryotic expression system should be used to produce a more homogeneous sample.

2   Zusammenfassung

In den letzten Jahrzehnten ist ein bis dahin kaum charakterisiertes Organell immer mehr in den Blickpunkt neuer Forschungsprojekte gerückt: das Cilium. Dieser Zellfortsatz spielt eine bedeutende Rolle in Signalübertragungswegen und steht in direktem Zusammenhang mit der Entwicklung diverser Krankheiten. Cilien sind aus einem Mikrotubuli-Axonem aufgebaut, welcher von der Plasmamembran umgeben ist, und über die Zelloberfläche hinaus wächst. Die Grundlage aller funktionierende Cilien ist der bidirektionale Transport der verschiedenen ciliaren Moleküle entlang des Axonems, der von großen Proteinkomplexen durchgeführt wird. Diese Einheiten werden als Intraflagellarer Transport (IFT) - Partikel bezeichnet, der in zwei Subpopulationen unterteilt werden kann: zum einen IFT Komplex A, der für den retrograden Transport verantwortlich ist und ausserdem IFT Komplex B, der unerlässlich für den anterograden Transport ist. IFT Komplex B besteht aus mindestens 14 verschiedenen Proteinen, von denen 8 auch bei hoher Ionenstärke miteinander verbunden bleiben und den Kern des Komplex B bilden. Die vorliegende Studie beschäftigt sich mit den acht Proteinen des IFT-B Kernes aus dem Organismus *Trypanosoma brucei*. Um alle Untereinheiten gemeinsam in einem heterologen bakteriellem System zu exprimieren, wurde das pETDuet System verwendet. Um den Komplex aufreinigen zu können, wurden zwei der acht IFT-B Kern Proteine mit einem Affinitäts-Tag fusioniert. Der rekombinante Kern von IFT Komplex B wurde auf eine Chromatographie-Säule geladen, wo er unterschiedliche oligomere Einheiten aufweist; von Aggregaten bis hin zu dem einzelnen Komplex. Die nachfolgenden Versuche fokussierten sich auch die Reinigung einer homogeneren Probe. Biochemische Analysen zeigten, dass wenigstens eine oder mehrere Untereinheiten an Liposomen binden, wobei es noch ungeklärt ist, welche das sind. Der partiell aufgereinigte Komplex kann für biochemische Studien und elektronenmikroskopische Analysen verwendet werden, kristallographische Ansätze sollten in Zukunft mit einem eukaryotischen Expressionssystem verfolgt werden, um eine homogenere Probe zu erhalten.

3 Introduction

3.1 Cilia

In 1676, van Leeuwenhoek for the first time described the organelle that was, after the initial interest faded, going to be scientifically neglected for most of the following centuries and, just in recent years, re-gained immense attention: *the cilium* (Haimo and Rosenbaum, 1981; Ringo, 1967; Satir, 1995). Originally distinguished from eukaryotic flagellum by means of copy numbers per cell, length, and beat modes, both terms are now used interchangeably since both describe basically an identical structure (Fisch and Dupuis-Williams, 2011). It has to be mentioned though that the eukaryotic flagellum should not be confused with the bacterial flagellum, which differs not only on a structural but also on a mechanistic level with its namesake (Macnab, 2003). The bacterial flagellum is a rather rigid structure that rotates clock- or anti-clockwise in contrast to the bending or whip-like motion of the eukaryotic flagellum (Macnab, 2003). Moreover, while the eukaryotic flagellar axoneme is assembled from microtubules, dyneins, and other accessory proteins, the bacterial flagellum is composed of multiple units of the protein flagellin (Alberts et al., 2002; Macnab, 2003).

Two examples of cilia in different organisms can be seen in Figure 1. Cilia and flagella have since been detected on numerous types of cells, ranging from protists to higher eukaryotes. Most of the initial ciliary research has been conducted in the green algae *Chlamydomonas reinhardtii (Cr)*; other prominent model organisms include *Caenorhabditis elegans (Ce), Trypanosoma brucei (Tb), Danio rerio (Dr) and Mus musculus (Mm)*.

Due to the increasing numbers of human disorders associated with ciliary dysfunctions, this organelle represents a fascinating object for scientific investigation. The following chapter will introduce both the structural composition of the cilium and how the structure is maintained, and will also give an overview of some of its important components within.
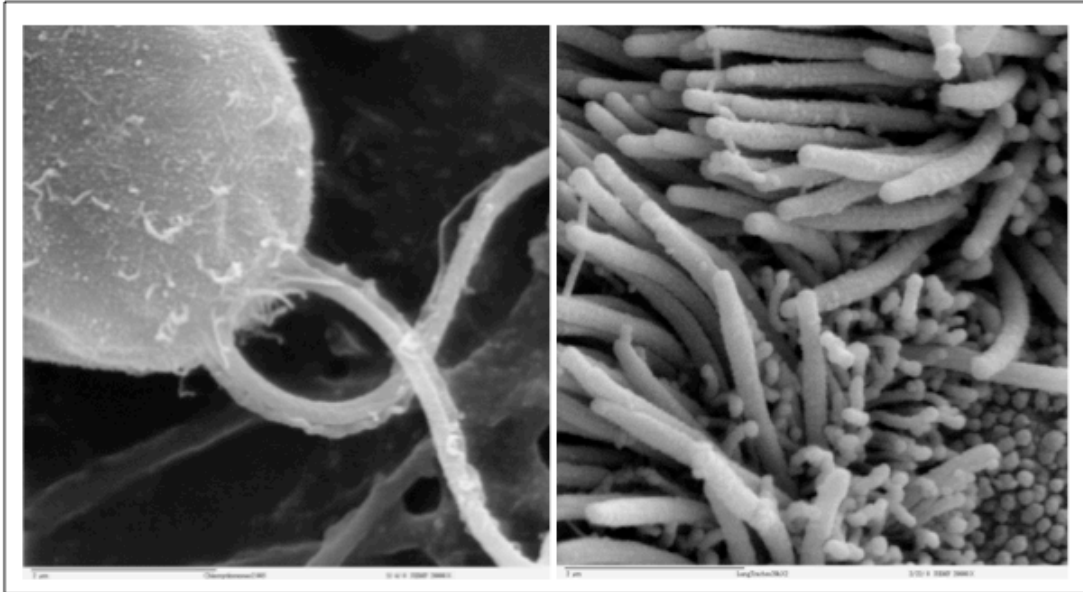
Figure 1 Scanning electron microscope images of cilia. The left panel shows a *Chlamydomonas reinhardtii* cell with two flagella. The right panel displays the multi-ciliated epithelial cells of mammalian lung trachea. Both images were taken at 20,000× magnification by the Dartmouth electron microscopy facility (http://remf.dartmouth.edu/imagesindex.html).

3.2   Ciliary architecture

The cilium is a membrane-encapsulated protrusion from the cell surface of almost all eukaryotic cell types. Its core structure is the ciliary axoneme, a microtubule based formation that extends from the basal body. As its precursor - the mother centriole, the basal body is composed of a ring of nine microtubule triplets. This circular structure is continued by the ciliary axoneme with the distinction that only two of the triplet microtubules further elongate. Thus a transition to doublet microtubules is observed (Figure 2). In the most distal part of the cilium a further decline in tubular number can be observed in plenty of organisms, leaving only singlet microtubules behind (singlet zone) (Fisch and Dupuis-Williams, 2011). No well-defined length of this singlet zone has been determined yet; variations in size are observed between different organisms as well as cell types (Fisch and Dupuis-Williams, 2011).
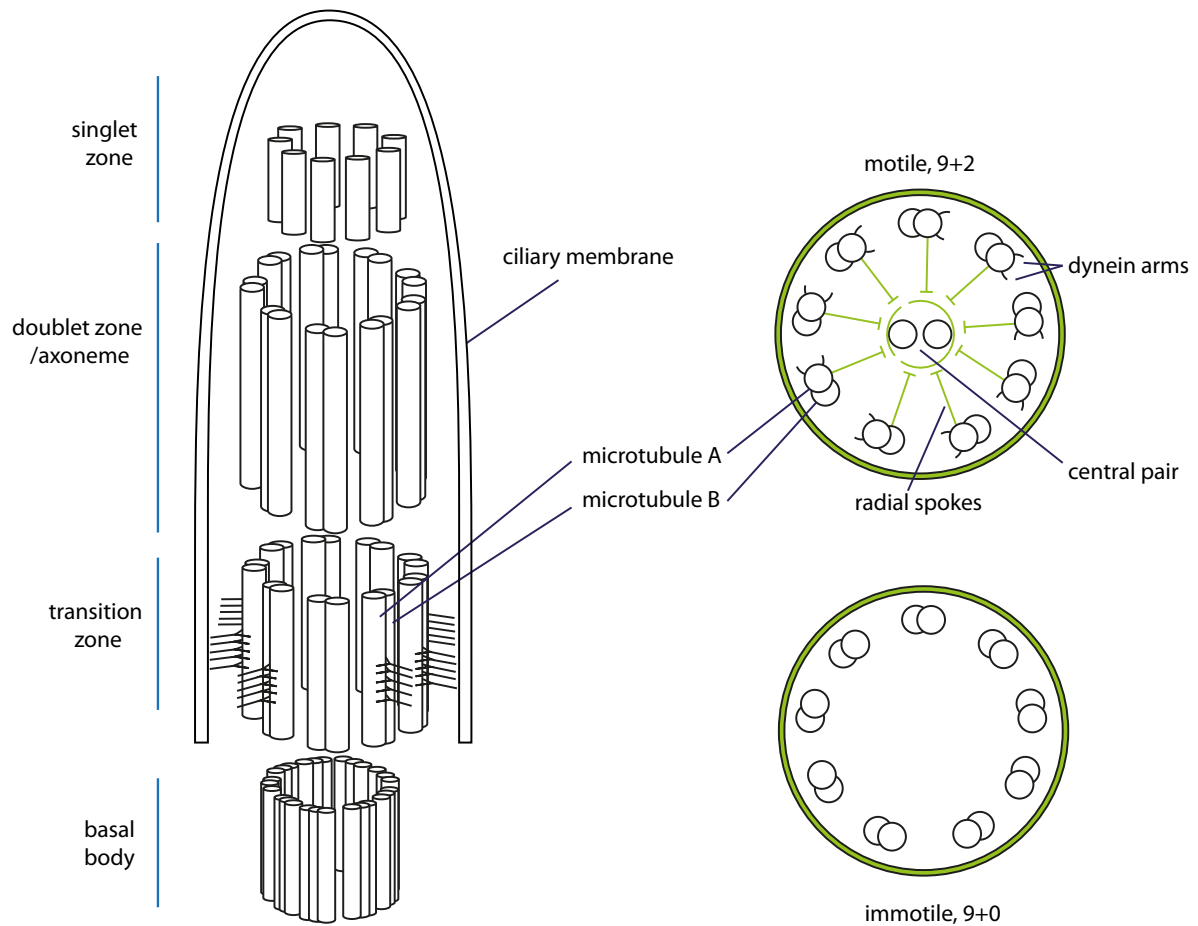
Figure 2 Architecture of the cilium. A schematic representation of the cilium is shown. Side- and cross-section views show the different layers from the basal body to the tip of the cilium, as well as the nine-fold symmetry of the microtubule ring. Motile cilia have additional features besides the central pair, such as the radial spokes complex that attaches to the microtubules (Ishikawa and Marshall, 2011). The figure is adapted from (Czarnecki and Shah, 2012).

The region where the change from triplet to doublet microtubules takes place is termed the transition zone. It is a highly complex region that is thought to represent a barrier between the cytoplasm and the ciliary compartment (Czarnecki and Shah, 2012). The transition zone in some way might act as a "flagellar pore complex" (Rosenbaum and Witman, 2002; Silverman and Leroux, 2009) by restricting and/or regulating the entry of ciliary components, similar to the nuclear pore complex. Recent data further support the existence of a selective diffusion barrier at the transition zone (Kee et al., 2012; Chih et al., 2012). Common features of this section are the transition fibers, projecting from the microtubules to the pericilliary membrane (Ringo, 1967). Although the exact composition of the region is unclear, several studies discovered numerous proteins that localise to the transition zone and

play an important role in regulating the cilium biogenesis. For example, Craige and colleagues identified *C. reinhardtii* protein CEP290 to be part of the transition zone. *Cr*CEP290 is suggested to be a key factor for the assembly of the microtubule-membrane linkers commonly existing in this region. Aberrant levels in flagellar protein content have been observed upon the loss of CEP290, indicating its role in regulating the access to the ciliary compartment (Craige et al., 2010).

Garcia-Gonzalo et al described a heptameric transition zone complex in *M. musculus* that is involved in controlling the content of the ciliary membrane as well as regulating ciliogenesis. Dysfunction of the complex results in different types of ciliopathies (Garcia-Gonzalo et al., 2011).

A recent study demonstrated that members of the nuclear pore complex (nucleoporins) are also located at the ciliary base (Kee et al., 2012). Furthermore, blocking the function of these nucleoporins restricts some proteins from entering the cilium (Kee et al., 2012). Thus, nucleoporins are not only located at the base of the cilium but also exhibit a similar function to that they have in the nuclear pore complex, regulating the entry of biological macromolecules into the flagellum. Although the ciliary membrane originates from the cellular membrane, studies have shown a different composition of lipid as well as polypeptide content compared to the plasma membrane (Pazour and Bloodgood, 2008; Emmer et al., 2010). For example, the flagellar membrane of *T. brucei* is enriched in sterols and sphingolipids (Tyler et al., 2009). Also, polycystin-2, a membrane protein associated with polycystic kidney disease (PKD), is found with elevated levels at cilia of human and mouse kidney cells. Interestingly, its transport into the organelle is independent of intraflagellar transport (IFT; part I, chapter 1.3), but probably not its recycling back into the cytoplasm (Pazour et al., 2002b). On the other hand, TRPV-channel proteins of *C. elegans* cilia move only in dependence of IFT (Qin et al., 2005). This indicates the existence of different pathways for transporting membrane proteins into the cilium. Nevertheless, how they work and/or are regulated is still a key question for future studies.

Cilia can be separated into two sub-groups termed 9+2 and 9+0, depending on whether they enclose a central pair of microtubule singlets within their microtubule ring (9+2) or not (9+0). In general, the 9+0 cilia are immotile, whereas the 9+2

flagella are motile (Figure 2) and responsible for liquid flow and cellular movement. In addition to missing the central pair, non-motile cilia normally lack the motor proteins that are essential for ciliary motility (Satir and Christensen, 2007). Nevertheless, exceptions to the rule have been published. Studies have identified non-motile 9+2 (Flock and Duvall, 1965; Reese, 1965) as well as motile 9+0 axonemes (Nonaka et al., 1998; Kramer-Zucker et al., 2005). Figure 2 shows a summary of the substructures found in cilia (Czarnecki and Shah, 2012).

The non-motile 9+0 flagellum frequently occurs as a single copy on the cell surface. It is called the primary cilium and plays a major role in signal transduction and sensing the cells environment (Pazour and Witman, 2003; Berbari et al., 2009). It has to be mentioned that besides their mechanistic properties, motile cilia also possess sensory functions (Shah et al., 2009). Additionally to the central pair, radial spokes (Figure 2) and dynein arms are attached to the microtubule doublets of 9+2 cilia, enabling the bending/beating of the cilium (Satir and Christensen, 2008). Flagella missing certain components of the radial spokes are characterised by an inability to move normally or even at all (Witman et al., 1978). Recently, a cryoelectron tomography study of the radial spoke complex of *C. reinhardtii* (composed of 23 proteins) was able to localise subsets of the involved proteins in the whole spoke complex and their possible contact with other axonemal constituents (Pigino et al., 2011), delivering further insight into the structural complexity of the ciliary skeleton.

3.3   Centrosome and basal body

As mentioned above, cilia emerge from the basal body, which originates from the mother centriole. The cilium and the basal body exhibit similar structures with the most prominent one being the nine-fold symmetry of the microtubules. Centrioles are observed as pairwise structures within the cells and have two distinct roles, (a) to organise the centrosomes, and (b) to nucleate the cilium as the basal body. The centriole is duplicated via a conserved pathway in which the existing centriole acts as a template for the newly formed daughter centriole. Only one of the two centrioles - the mother centriole - transforms into the basal body that gives rise to the cilium (Hoyer-Fender, 2010). On the other hand, it has been observed that centrioles can

also form *de novo* from fibrogranular assemblies when no templating centrioles exist. This pathway is commonly used in cells displaying multiple cilia on their surface (Sorokin, 1968; Brito et al., 2012). Ciliogenesis starts with the addition of a golgi-derived vesicle to the distal end of the centriole, followed by the formation of the ciliary axoneme (Sorokin, 1962). More vesicles will integrate to the initial one until a fusion between the centriole-vesicle and the plasma membrane takes place (Sorokin, 1962). Further elongation of the cilium is mediated by the integration of axonemal components at the tip of the flagellum by means of intraflagellar transport (part I, chapter 1.3). Prior to mitosis, the cilium is resorbed in order to free the basal body for its role as the microtubule-organising center (MTOC) during the cell cycle. Studies suggest that the flagella do not have to be completely resorbed for the release of the centriole (Parker et al., 2010). Due to this rather close relationship between the centrosome and the basal body, it is not surprising that some proteins fundamental for ciliogenesis have been identified to play important roles during the cell cycle, as will be described later.

3.4   Intraflagellar transport

Since no proteins are synthesised within the cilium, a mechanism for transporting ciliary building blocks and other molecules into and within the organelle is required. The process of transporting molecules to the tip as well as recycling turnover products is called intraflagellar transport (IFT). This bi-directional movement was first described two decades ago by Kozminski and colleagues (Kozminski et al., 1993) when they visualised an intra-ciliary motility in *Chlamydomonas* unrelated to flagellar kinetics by using differential interference-contrast microscopy. This marked the starting point for a new direction in ciliary research, focusing on unravelling the underlying mechanistic of IFT as well as its association with signal transduction processes and subsequently diverse ciliopathies.

IFT is carried out by an intricate machinery composed of a vast number of different proteins that possess distinguished roles in the whole process. In general, IFT is a bi-directional movement of ciliary molecules along the axoneme. The main component is the IFT particle, a multi-subunit polypeptide assembly (Figure 3).
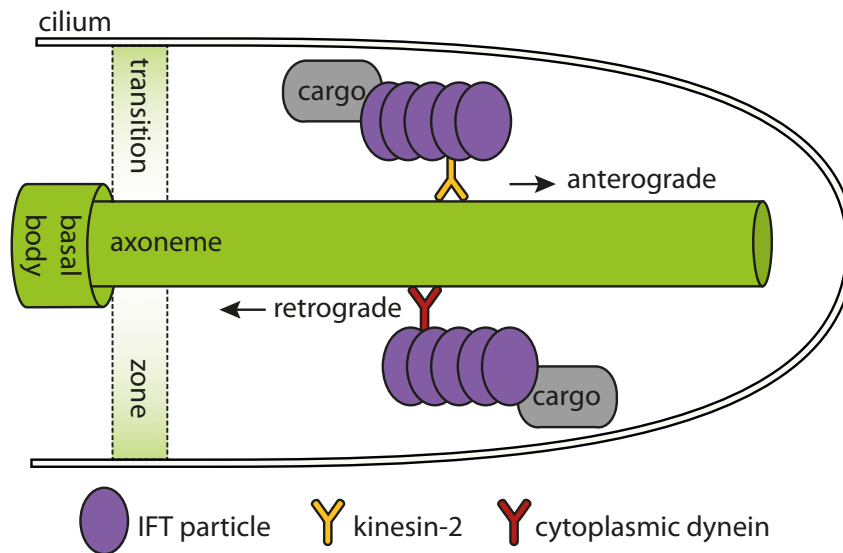
Figure 3 Intraflagellar transport. A simplified representation of IFT within the flagellum. Trains of IFT particles are moving with different velocities along the ciliary axoneme with the coordinated help of the respective motor proteins. At the tip, a remodelling of the particles and cargo-exchange take place in order to recycle the turnover products back to the ciliary compartment.

Members of the IFT complex were initially identified by Piperno and Mead over a decade ago (Piperno and Mead, 1997). They analysed flagellar extracts of *C. reinhardtii* and discovered a protein complex composed of at least 13 different subunits. Shortly afterwards, Cole and colleagues (Cole et al., 1998) also reported the purification of the particle from *Chlamydomonas* and the detection of 15 different subunits within. They named the different polypeptides regarding their apparent molecular weights on an SDS-PAGE gel as p172, p144, p140, p139, p122, p88, p81, p80, p74, p72, p57/55, p52, p46, p27, and p20 (the ***p*** was later replaced by ***IFT***, which until now is the commonly used nomenclature for IFT particle components). Additionally, they managed to further distinguish two stable sub-populations of the complex, termed complex A (IFT-A; part I, chapter 3.4.1) and complex B (IFT-B; part I, chapter 3.4.2) (Cole et al., 1998).

To date, IFT complex A has been confirmed to consist of IFT144, IFT140, IFT139 and IFT122 plus the later identified IFT121 (Blacque et al., 2006) and IFT43 (Piperno et al., 1998). IFT-B consists of IFT172, IFT88, IFT81, IFT80, IFT74/72, IFT57/55, IFT52 IFT46, IFT27, IFT20 and the more recently discovered subunits IFT25 (Follit et al., 2009; Lechtreck et al., 2009), IFT22 (Schafer et al., 2006), putative IFT54/Dyf-11 (Li et al., 2008; Omori et al., 2008; Follit et al., 2009), and IFT70 (Fan et al.,

2010). These novel subunits have been identified in various organisms, ranging from *Chlamydomonas reinhardtii* over *Caenorhabditis elegans* to *Mus musculus*.

Table 1 Overview of the various names of IFT components in different organisms. Adapted from (Ishikawa and Marshall, 2011; Follit et al., 2009)

IFT component	*Chlamydomonas reinhardtii (Cr)*	*Caenorhabditis elegans (Ce)*	*Homo sapiens*	**Other**
IFT complex A	IFT144	DYF-2	WDR19	
	IFT140	CHE-11	IFT140	
	IFT139	ZK328.7	THM1, TTC21B	
	IFT122	DAF-10	IFT122, WDR10	
	IFT121	IFTA-1	WDR35	
	IFT43	-	IFT43, C14orf179	

IFT component	*Chlamydomonas reinhardtii (Cr)*	*Caenorhabditis elegans (Ce)*	*Homo sapiens*	**Other**
IFT complex B	IFT172	OSM-1	IFT172	
	IFT88	OSM-5	IFT88	Tg737, Polaris
	IFT81	IFT-81	IFT81	
	IFT80	CHE-2	IFT80, WDR56	
	IFT74 IFT72	IFT-74	IFT74, IFT72	
	IFT70	DYF-1	TTC30A, TTC30B	Fleer
	IFT57	CHE-13	IFT57	
	IFT54, FAP116	DYF-11	IFT54, TRAF3IP1	Elipsa
	IFT52	OSM-6	IFT52, NGD5	
	IFT46, FAP32	DYF-6	IFT46, C11orf60	
	IFT27, FAP156	-	IFT27, RABL4	
	IFT25, FAP232	-	IFT25, HSPB11	
	IFT22, FAP9	IFTA-2	RABL5	
	IFT20	Y110A7A.20	IFT20	

Table 1 shows an overview of the naming conventions in different organisms. Since most of the groundbreaking work on IFT has been conducted in *Chlamydomonas,* I will by default refer to their nomenclature for IFT components.

Most of the proteins involved in IFT have been identified as conserved among ciliated organisms (for complex B see (Fan et al., 2010)). Outside the flagellar compartment, members of IFT particle are predominantly localised at the basal body of the cilium (Qin et al., 2004). Interestingly, IFT complexes A and B localise at different positions around the basal body (Hou et al., 2007), indicating that they are not necessarily in physical contact outside the flagellum.

Although both IFT complexes travel together from the basal body to the tip and vice versa, different roles have been established for them, with IFT-B mainly responsible for the anterograde transport and IFT-A essential for a functioning retrograde transport. Nevertheless, some data suggests that this classic view might oversimplify the real situation; rather individual subunits of both complexes are linked to the motor proteins or cargo (Keady et al., 2012). To enable movement along the axoneme, microtubular motor proteins are needed. Studies have identified the anterograde motor to be heterotrimeric kinesin-II (Kozminski et al., 1995; Cole et al., 1998), and the retrograde movement to be mediated by cytoplasmic dynein 1b (DHC1b) (Pazour et al., 1999). Interestingly, whereas in *Chlamydomonas* heterotrimeric kinesin-II alone is sufficient for ciliogenesis, other organisms possess a second homodimeric kinesin, such as OSM-3 in *C. elegans* (Signor et al., 1999). Closer examination of the particle movement of the anterograde and retrograde transport revealed a difference in the travel velocities of both motilities. While the anterograde transport is moving with approximately 2 μm/sec, the retrograde transport advances with ~3 μm/sec (Cole and Snell, 2009). In *Chlamydomonas,* depletion of kinesin-II results in the interruption of IFT and consequently flagellar resorption (Kozminski et al., 1995), whereas cells harboring a deletion mutant of the DHC1b gene exhibit short flagella with bulgy tips (Pazour et al., 1999). Aside from these effects on ciliary integrity, other phenotypes can be observed upon disruptions in IFT motors and particles and will be explained in later (part I, chapter 3.5).
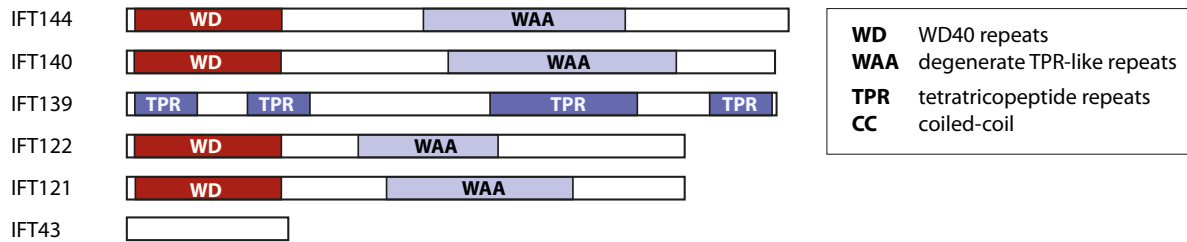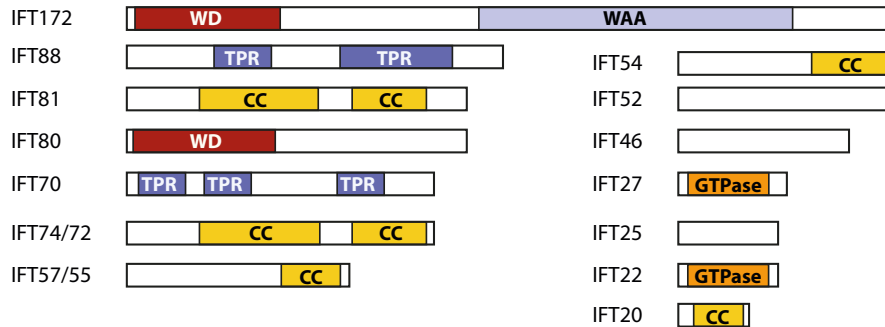
Figure 4 Domain arrangements of the IFT complexes. Different protein-protein interaction motifs found in *C. reinhardtii* IFT particle components. Adapted from Cole (Cole, 2003) and (Behal et al., 2012).

Analysis of conserved domains within the IFT particles showed that most of the subunits have multiple putative protein-protein interaction motifs such as the WD-40 repeat, the tetratricopeptide repeat (TPR) and coiled-coil domains (Figure 4). Additionally, degenerate TPR-like repeats (WAA) were identified in most of complex A proteins, which were initially termed degenerative repeats (Cole, 2003; Behal et al., 2012). Interestingly, four subunits of the IFT complex A and IFT172 of the complex B share a rather similar domain organisation. Furthermore, IFT27 and IFT22 of complex B both contain a small GTPase domain (Qin et al., 2007; Schafer et al., 2006).

To date, the most detailed ultra-structural examination of the IFT particle in *Chlamydomonas* is presented in the work of Pigino and colleagues (Pigino et al., 2009). By means of transmission electron microscopy and electron-tomography, they observed trains of IFT particles between the flagellar membrane and the axoneme, with linkages to both the membrane and the axoneme. A closer look at these trains revealed two different types: short, thick trains with a periodicity of 16 nm and long, thin trains with 40 nm periodicity (Pigino et al., 2009). However, due to resolution limits, no individual subunits could be localised within the observed structures,

making it still a subject of further investigation. In order to unravel the intricate network underlying intraflagellar transport and its regulation, functional and structural studies of each single component are of immense interest.

3.4.1 IFT complex A

As described above, the IFT complex A consists of six different subunits. Except for IFT43, all other subunits of the IFT-A are rather large polypeptides, with molecular weights of higher than 120 kDa (Taschner et al., 2011). Due to this, less advances in studying these proteins in a recombinant system have been made compared to the IFT complex B (Behal et al., 2012).

IFT144, IFT140 and IFT122 are capable of assembling into a stable sub-complex in the absence of IFT139 and IFT121 (Mukhopadhyay et al., 2010; Behal et al., 2012). Further analyses suggest that IFT121 is required for the integration of IFT139 and IFT43 into the complex (Behal et al., 2012), and IFT121 in turn requires IFT140 for proper association with the IFT machinery (Blacque et al., 2006). IFT43, the smallest and least conserved member of the IFT complex A, directly interacts with the C-terminal part of IFT121 (Behal et al., 2012). Interestingly, in contrast to flagellar extracts, analysis of *Chlamydomonas* whole cell or cell body extracts indicates that only a subset of the IFT43 population is associated with the other subunits of IFT-A (Behal et al., 2012).

Deficiencies in IFT-A complex proteins – similar to mutations affecting the retrograde motor - result in malformed and malfunctioning (Blacque et al., 2006), short or even absent cilia (Behal et al., 2012). Common for most of these IFT-A mutants are the bulges along the formed cilia that are in general enriched in IFT-B proteins (Piperno et al., 1998; Iomini et al., 2009) (also reviewed in (Ishikawa and Marshall, 2011; Taschner et al., 2011)).

3.4.2 IFT complex B

Current data show that the IFT complex B is composed of at least 15 different subunits. It has been demonstrated that under increasing ionic strengths, some

proteins dissociate from the complex (Lucker et al., 2005). Thus, a sub-classification of IFT-B into a salt-stable IFT-B core complex plus weakly associated proteins (Figure 5) has been made. The salt-stable core of IFT-B contains nine different subunits, namely IFT88, IFT81, IFT74, IFT70, IFT52, IFT46, IFT27, IFT25 and IFT22.
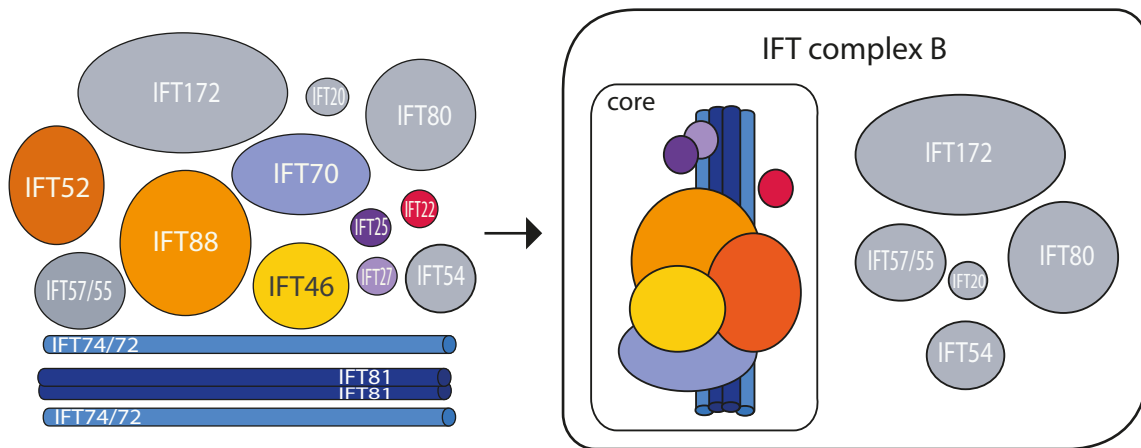
Figure 5 Composition and assembly of the IFT complex B. Nine IFT-B proteins are able to form a core-complex even under the ionic strength of 300 mM NaCl (Lucker et al., 2005). Proteins in grey easily dissociate from the complex B under high-salt conditions. Chemical cross-linking, *in vivo* binding assays and yeast-two-hybrid studies have been conducted to identify contacts between the core members. Adapted from (Lucker et al., 2010) and (Taschner et al., 2011).

Depletion of certain members of IFT-B results in small, stumpy or even absent flagella (Brazelton et al., 2001; Haycraft et al., 2001), (further reviewed in (Ishikawa and Marshall, 2011; Taschner et al., 2011)) due to the fact that the required building blocks cannot be transported into the cilium. This phenotype is similar to mutations affecting the anterograde motor kinesin-2, as mentioned earlier.

The largest subunit of the core complex is IFT88, which has been shown to contain several TPR repeats (Pazour et al., 2000), (Figure 4). *Cr*IFT88 is homologous to mouse and human Tg737 (Table 1), a protein associated with polycystic kidney disease, (Pazour et al., 2000) and *C. elegans* OSM-5 (Haycraft et al., 2001; Qin et al., 2001). IFT88 is essential for the formation of cilia both in *Chlamydomonas* (Pazour et al., 2000) and in vertebrates (Pazour et al., 2002a). In *C. elegans*, mutations in OSM-5 lead to significantly shorter cilia in chemosensory neurons (Haycraft et al., 2001). Different studies established a role of IFT88 outside ciliogenesis in the cell

cycle. In mammalian cells, centriole-associated IFT88 controls the G1-S phase transition (Robert et al., 2007) and is involved in maintaining the correct spindle orientation during mitosis (Delaval et al., 2011).

IFT74 and IFT72 are two isoforms of the same gene (Qin et al., 2004) and are often referred to as IFT74/72. IFT81 and IFT74 are both composed of a long coiled-coil region. Cross-linking experiments followed by yeast-two-hybrid (Y2H) studies of *C. reinhardtii* constructs demonstrated that both proteins interact via their coiled-coil domains (Lucker et al., 2005). Furthermore, IFT81 is able to homodimerise in the Y2H studies, as opposed to IFT74, thus suggesting that the polypeptides form a hetero-tetramer composed of each two copies IFT81 and IFT74 (Lucker et al., 2005). Studies in *C. elegans* revealed that mutations in the IFT81 and IFT74 genes result in chemosensory deficiencies but lead to less ciliogenetic defects than other IFT-B mutants (Kobayashi et al., 2007).

The most recent addition to the IFT complex B was IFT70, which represents one of the most conserved subunits of the complex (Fan et al., 2010). Initially identified in *C. elegans* as Dyf-1, IFT70 was shown to contain several TPR and prenyltransferase motifs; previous studies suggested that it mediates the interaction between the motor subunit OSM-3 and the IFT-particle (Ou et al., 2005). However, no direct interaction between IFT70 and OSM-3 could be detected, indicating an indirect link between the two (Ou et al., 2005). *Chlamydomonas* cells depleted of IFT70 show a decrease in their flagellar length as well as in the expression levels of other IFT-B components (Fan et al., 2010), whereas *Tetrahymena termophila* IFT70 mutants are characterised by de-stabilised, short axonemes (Dave et al., 2009).

Similarly to IFT88, deletion of IFT52 has severe effects on ciliogenesis. *Chlamydomonas* deficient in IFT52 are not able to assemble cilia (Brazelton et al., 2001). By means of immunoelectron microscopy it was established that *Cr*IFT52 localises to the basal body in addition to the transitional fibers close to the membrane (Deane et al., 2001). It is suggested that these fibers serve as a docking point for the IFT particles (Deane et al., 2001), before they enter the ciliary compartment.

IFT46 is highly conserved among ciliated organisms, and *Chlamydomonas* null-mutants are not able to assemble full-length, motile flagella, but only short, immotile

ones (Hou et al., 2007). Interestingly, comparing the axonemes of wild-type and *ift46*-mutant flagella revealed an absence of dynein arms within the axoneme, although normal levels of it are observed in the cell lysate (Hou et al., 2007). It was shown that IFT46 is crucial for the transport of the outer dynein into the flagellum (Hou et al., 2007), which it does with the help of another protein, ODA16 (Ahmed et al., 2008). As can be observed for other IFT-B proteins, deletion of IFT46 reduces the levels of other complex members, with the notable exception of IFT172 (Hou et al., 2007).

A detailed study by Qin and colleagues (Qin et al., 2007) demonstrates that *Cr*IFT27 is a Rab-like small GTPase, with no homologs in either *C. elegans* or *Drosophila*. Its association with the IFT complex B is independent of its GTP/GDP bound state (Qin et al., 2007). Interestingly, partial knockdown of IFT27 results in failing cell division and elongated cell cycle, whereas a complete knockdown is lethal (Qin et al., 2007). This indicates that IFT27, like IFT88, plays an important role outside the intraflagellar transport.

One of the more recently identified member of the complex B-core is IFT25, which was identified both in *C. reinhardtii* (Lechtreck et al., 2009; Wang et al., 2009) and in *M. musculus* (Follit et al., 2009). As for IFT27, no homologs in *C. elegans* and *D. melanogaster* were detected for IFT25 (Lechtreck et al., 2009). Wang et al (Wang et al., 2009) identified IFT25 as a phosphoprotein, a modification shown to be important for its integration into IFT-B. IFT25 is not crucial for ciliary assembly but rather for functioning hedgehog signaling (Keady et al., 2012). Immunofluorescence studies reveal that IFT25 localises to the basal body as well as to areas around the transition zone (Wang et al., 2009). In the latter region, it overlaps with IFT27 distribution, which goes in line with pull-down studies verifying a direct interaction between the two proteins (Wang et al., 2009). Notably, in the cytoplasm but not in the flagellum, fractions of IFT25 and IFT27 can be found as a separate entity from the IFT complex B (Wang et al., 2009). The crystal structure of the recombinant *Cr*IFT27-IFT25 complex was recently published (Bhogaraju et al., 2011), showing an elongated shape with the interface mostly between the C-terminus of IFT27 and two loop regions of IFT25.

Besides IFT27, IFT22 is the second Rab-like protein of the IFT complex B. Interestingly it is indispensable for flagella formation in *T. brucei* (Adhiambo et al., 2009) but not in *C. elegans* (Schafer et al., 2006). A recent study by Silva and colleagues (Silva et al., 2011) analysed the role of IFT22 in *C. reinhardtii* in more details. Intriguingly, although RNAi depletion of IFT22 resulted in a decrease (with varying extent) of the cellular pools of both IFT-A and −B proteins, an increase in flagellar amounts of IFT particle polypeptides was observed (Silva et al., 2011). Thus it was hypothesised that IFT22 is a key player in regulating the number of IFT particles within the cilium, hence the quantity of material transported into the flagellum. Remarkably, both Rab-like proteins, IFT22 and IFT27, have been found to lack the lipid modifications that are common for most Rab-like proteins (Qin et al., 2007; Silva et al., 2011).

Aside from the 9 core-components, the IFT complex B contains the herein mentioned peripheral subunits IFT172, IFT80, IFT57, IFT54 and IFT20. Previous studies in *Chlamydomonas* suggest that IFT172 collaborates with EB1 (microtubule end binding protein 1) to facilitate the reversal of the IFT particles at the flagellar tip (Pedersen et al., 2005).

Studies in mouse show that expression of IFT80 at hypomorphic levels is embryonic lethal although no significant ciliary degenerations but rather hedgehog signaling defects are observed, suggesting that low levels of the protein are sufficient to maintain the cilium but not to continue its signaling functionality (Rix et al., 2011). Upon knockdown of IFT80 in *D. rerio*, defects of photoreceptors (Hudak et al., 2010) or formation of kidney cysts (Beales et al., 2007) can be observed.

IFT57 is associated with less severe ciliogenetic defects than other IFT-B components; zebrafish depleted in IFT57 are still able to assemble cilia, although they are shorter than their wild-type counterparts (Krock and Perkins, 2008).

Another IFT complex B member - IFT54, also known as elipsa in *Danio rerio* or DYF-11 in *C. elegans*, contains two coiled-coil regions (Omori et al., 2008). In *C. elegans,* the C-terminal coiled-coil region was identified to be essential*,* whereas the N-terminal domain was negligible for IFT54 function in cilia (Kunitomo and Iino, 2008). Yeast two-hybrid studies indicate IFT20 and rabaptin 5, a polypeptide

involved in endocytic vesicle fusion, as potential binding partners of *Dr*IFT54 (Omori et al., 2008). Further tandem affinity purifications using *Dr*IFT54 as bait identified IFT20, IFT57, IFT80, IFT81, IFT172 and Qilin as its binding partners (Omori et al., 2008).

IFT20 is the smallest member of the IFT complex B and has been established to be unique among IFT-B members due to its additional localisation to the Golgi complex in mammalian systems (Follit et al., 2006). Interestingly, in T-lymphocytes, which are non-ciliated cells, IFT20 is expressed and localises to the Golgi, the MTOC and the immune synapse (Finetti et al., 2009).

Yeast-two hybrid and pull-down studies identified *Mm*IFT20 to bind to IFT57 (Baker et al., 2003; Follit et al., 2006) and kinesin-2 (Baker et al., 2003). IFT particles deficient in *Dr*IFT57 do not contain IFT20 but are still able to bind to kinesin-2 subunit (Krock and Perkins, 2008), suggesting a linkage between the motor and the IFT particle independent of IFT20. Further studies established *Mm*IFT20 to be essential for transporting the membrane protein polycystin-2 into the ciliary membrane (Follit et al., 2006).

Accordingly, Follit and colleagues (Follit et al., 2009) proposed a model in which IFT20 together with its Golgi-binding partner GMAP210 (Follit et al., 2008) localises to the Golgi network to sort the vesicles destined for the flagellar compartment. IFT20 associates with these vesicles and transports them to the ciliary base, where its interaction with IFT54 and subsequently the remaining IFT complex B takes place.

Until now, extensive studies have been conducted to identify the binding partners/regions within the IFT complex B in order to understand how the complex is assembled and to define possible regulatory mechanisms of the assembly. For the core complex, following binding partners and/or sub-complexes have been established. As described previously, IFT74 and IFT81 are known to interact and, more precisely, they are thought to form a hetero-tetramer (Lucker et al., 2005). Chemical cross-linking experiments identified associations between IFT52 and IFT88 as well as between IFT81 and IFT27 (Lucker et al., 2010). Tandem affinity chromatography studies showed that even in the absence of other IFT-B core components, IFT52, IFT46 and IFT88 are capable of forming a sub-core complex

(Lucker et al., 2010). Pull-down experiments demonstrated that *Cr*IFT46 and *Cr*IFT70 are capable of forming a dimer (Fan et al., 2010). As already mentioned, direct interaction of *Cr*IFT27 and *Cr*IFT25 has been shown via *in vitro* binding assays (Wang et al., 2009) and co-crystallisation (Bhogaraju et al., 2011). Taken the previous results together, it is likely that the IFT-B core assembles via 3 sub-core complexes, namely the tetrameric IFT81-74, the trimeric IFT88-52-46, and the dimeric IFT27-25. The order of their recruitment to built-up the final core complex still awaits further studies, so as when and how the associated subunits come into play. It was shown that the IFT-B is pre-assembled prior to entering the ciliary compartment (Wang et al., 2009). However, it remains unknown to which subunit IFT22 binds. Pull-down studies with the peripheral subunit *Mm*IFT20 identified IFT52, IFT57 and IFT88 as its binding partners (Follit et al., 2006).

Taken together all these data on the individual IFT-B subunits, it can be concluded that in most cases removal of any single component has severe effects on ciliogenesis by disrupting the integrity of the whole transport particle. Probably due to the close relationship between the basal body and centrosomes, some of the IFT proteins play an additional role during the cell cycle, even in non-ciliated organisms. Increasing evidence of a role of IFT and its constituents outside the classical ciliary compartment (Finetti et al., 2009; Baldari and Rosenbaum, 2009; Sedmak and Wolfrum, 2010) and the intimate relationship with signal transduction cascades like the hedgehog and the Wnt signaling pathways (reviewed in (Gerdes et al., 2009; May-Simera and Kelley, 2012)) emphasises the immense importance of the cilium.

3.4.3 IFT and Chaperones

Chaperone proteins play a critical role in the folding of cellular proteins or degradation of denatured proteins if refolding attempts fail (reviewed in (Hartl et al., 2011)). Hsp70 chaperones represent a well-conserved class of chaperones (Hartl and Hayer-Hartl, 2002) and previous studies suggest a stabilising role of the Hsp70 proteins on cytoplasmic microtubules (Silflow et al., 2011). Interestingly, some Hsp70s were first identified as microtubule-associated proteins (MAPs) before their function as chaperones were established (Liang and MacRae, 1997). Aside from stress-induced Hsp70 homologs, higher eukaryotes also contain constitutively

expressed Hsp70, termed Hsc70 (Hartl et al., 2011). In *Chlamydomonas,* Hsp70 can be found – aside from the cytosol – in the flagellum, concentrated at the flagellar tip; additionally it co-localises with the anterograde motor kinesin-2 (Shapiro et al., 2005). Interactions between Hsc70 or DnaJ with IFT components such as IFT88 have been published (Bhowmick et al., 2009). Initial investigations suggested Hsp70 to be part of the IFT particle (Piperno and Mead, 1997), but subsequent experiments did not come to the same conclusion (Cole et al., 1998). Overall, the specific role of chaperones/Hsp70 within the flagellum and their connection with intraflagellar transport is still nebulous and remains a topic for future research.

3.5   Ciliopathies

One of the main reasons that research started to regain its interest in cilia and flagella was the occurrence of human pathologies connected with defects in ciliogenesis and its associated molecules. The diverse ciliary disorders are collectively described as "ciliopathies".   Prominent ciliopathies include primary cilia dyskinesia (PCD), polycystic kidney disease (PKD, (Pazour et al., 2000; Yoder et al., 2002)), Meckel-Gruber syndrome (MKS, (Dawe et al., 2007)), nephronophthisis (NPHP, (Otto et al., 2003)), Joubert syndrome (JS, (Parisi et al., 2007)), and Bardet-Biedl syndrome (BBS, (Kulaga et al., 2004; Mykytyn et al., 2004)). These disorders have been traced to cilia either losing their motile function (Afzelius, 1976) or incapable of continuing signal transduction. Various mutations directly involved in the onset of ciliopathies in human proteins have now been identified, (for reviews see (Badano et al., 2006; Oh and Katsanis, 2012)). A mutation of IFT80 in human patients correlates with the development of Jeune asphyxiating thoracic dystrophy (JATD) (Beales et al., 2007). Interestingly, although accumulating data suggest that dysfunction of most IFT-B proteins causes strong defects in ciliogenesis, there are not a lot of IFT-B gene mutations directly linked to human ciliopathies. A recent publication by Keady and colleagues (Keady et al., 2012) suggests that this could be due to prenatal lethality upon loss of cilia. Thus, most of these mutations are hypothesised to lead to miscarriage rather than the development of postnatal ciliopathies.

4   Aim

Intraflagellar transport is vital for a functioning cilium, as can be seen from the diverse set of pathologies associated with components of this intracellular movement. The importance of the IFT complex B can be recognised by the fact that abolishing single subunits is in most cases detrimental for the functionality of the whole transport. To date, protein crystal structures have only been published for two small subunits of the IFT complex B. Low resolution electron tomography pictures have given an idea about the rough architecture of the complete IFT particle, but very little is known about the intricate machinery at the structural level.

To shed light on the complex network and elaborate interactions within a part of the IFT machinery, I will try to reconstitute the IFT complex B core from *T. brucei*. The eight IFT proteins (IFT88, IFT81, IFT74, IFT52, IFT46, IFT27, IFT25 and IFT22) will be co-expressed with the final goal being to obtain pure sample of the protein complex and to characterise its assembly by various biophysical techniques and, if possible, to co-crystallise this recombinant IFT-B core complex. Additionally, various sub-core complexes such as the IFT74/IFT81 heterotetramer will be examined separately. Furthermore, I will also try to structurally investigate the peripheral subunit IFT20 that has been implicated to be important in sorting the vesicles destined for the cilium. Accompanying biochemical studies will provide further insights into the functionality of the complex.

5 Materials and Methods

5.1 Cloning

For all DNA purification and clean-up steps different commercial kits from Qiagen were used according to the respective manuals (QIAprep Spin Miniprep kit, QIAquick PCR purification, QIAquick gel extraction). All centrifugation steps were carried out at room temperature using a tabletop centrifuge 5424 (Eppendorf) at 13,000 rmp (15,871 x g). DNA concentrations were measured on a NanoDrop spectrophotometer ND-1000 (PeQlab). *E. coli* strain DH5α was used to amplify all used commercial vectors as well as our generated plasmids. Standard protocols for transformation into chemically competent cells were used. DNA sequencing was exclusively done by LGC Genomics (Germany).

The full-length ORF of the eight different IFT complex B subunits were PCR amplified using *T. brucei* cDNA as template (gift from the Warren lab, MFPL, Vienna) and Phusion polymerase (NEB Biolabs).

Table 2 Constructs of IFT complex B.

Protein	Restriction sites (protein)	Vector	MCS	Affinity Tag
IFT46	NcoI/BamHI	**petDuet**/Amp^R	1	C-terminal 6x His
IFT52	NdeI/BamHI		2	-
IFT74	NcoI/BglII	**pCDF**/Sm^R	1	-
IFT81	NdeI/BamHI		2	N-terminal 6xHis
IFT27	NcoI/BamHI	**pCOLA**/Kan^R	1	-
IFT22	NdeI/XhoI		2	-
IFT88		**pACYC**/Cam^R	1	-
IFT25	NdeI/BglII		2	-
Hsp70	NdeI/BamHI	**KiM2a**/Amp^R	-	N-terminal MBP
IFT20	NcoI/BamHI	**HM15b**/ Amp^R	-	N-terminal 6xHis

The Duet Vector System (Novagen) was chosen to enable co-expression of all different subunits. Each vector carries two multiple cloning sites (MCS). For all constructs, MCS1 was cut using NcoI and BamHI and MCS2 using NdeI and BglII. Additionally, homemade vectors with a maltose binding protein (MBP) (KiM2a) or 6×His affinity tag (HM15b) were used. Table 2 summarises the generated constructs of the IFT complex B core and Hsp70 and IFT20.

DNA sequencing result of the IFT46 construct showed an N-terminal mutation (M45I). This mutation was present in all IFT46 clones, which is likely pre-existing substitution in the cDNA used for amplification. We have observed such discrepancy from the deposited gene data when cloning other *T. brucei* genes and believe it is due to the difference between the two different forms of the parasite, i.e. procyclic and bloodstream forms. The mutation lies in a region predicted to be unstructured and does not change the charge of the protein.

During initial cloning of IFT27 a mutation of the first amino acid from M1 to H was overlooked, resulting in no expression of this construct. To re-establish the sequence, the quickchange mutagenesis kit (Stratagene) was used to change the incorrect amino acid back to methionine. IFT22 was cloned into the second MCS of the precloned IFT27-pCOLA using the In-Fusion protocol (Clontech).

Hsp70 was cloned into a homemade vector KiM2a that provides an N-terminal MBP tag. Sequence analysis showed an insertion of T after nucleotide No. 1895, leading to an earlier stop codon. The translated protein has a length of only 661 amino acids (aa) instead of 690 aa. This insertion was present in all constructs sent for sequencing, independent of the used genomic DNA. Interestingly, analysis of Hsp70 within other *Trypanosoma* species showed that the homolog from *T. brucei gambiense* DAL972 has this T-insertion occurring naturally. As explained above, this could be due to the two different forms of the parasite. It could be possible that the published sequence of *T. brucei* Hsp70 is not correct.

5.2   Expression & Purification

For the expression of recombinant proteins, *E. coli* strain BL21 (DE3) was used. In addition, *E. coli* strain EN2 (gift from Nadia Benaroudj, Institute Pasteur) was used, which is a DnaK deletion strain. EN2 cells are kanamycin resistant and need to be grown at ≤ 30°C.

Given the difficulties in cotransforming all four vectors at once, I used a two-step transformation strategy. In the first step, two of the vectors (either petDuet and pCDF or pACYC and pCOLA) were co-transformed into *E. coli* BL21 (DE3). In the second step, chemical competent cells were prepared from the colonies with two plasmids and used for the co-transformation of the remaining two plasmids, pACYC/pCOLA or petDUET/pCDF, respectively. As suggested by the Novagen protocol, the antibiotic concentration was halved when expressing all four plasmids together.

To co-express the core complex with Hsp70 the following strategy was used: IFT46-IFT52 (petDuet) and IFT74-IFT81 (pCDF) were co-transformed, as were IFT88-IFT25 (pACYC), IFT27-IFT22 (pCOLA) and Hsp70 (KiM2a). Upon harvesting both cell-pellets were pooled for subsequent purification.

All expressions were carried out at low temperature (16-18°C) to increase the amount of soluble proteins. In short, cells were grown to an optical density at 600 nm (OD_{600}) of 0.5-0.8 at 37°C. Prior to shifting to 16°C or 18°C, the cultures were incubated on ice for about 10 minutes ('cold shock'). 45-60 minutes after transferring the cultures to the low temperature protein expression was induced with 0.5 mM IPTG. Cells were harvested 16-20 hours post-induction with a JLA 8.1000 rotor on an Avanti J-26 XP centrifuge (Beckman Coulter).

Pelleted cells were resuspended in lysis buffer (20 mM Tris-HCl pH 8.0, 100-300 mM NaCl, 5% glycerol, 20 mM imidazole, 1 mM PMSF, 2 μg/ml DNAse I) and broken using the Emulsiflex-C3 Homogenizer (Avestin). Cell lysate was cleared by centrifugation at 16000 rpm (30600 rcf) for 25 minutes using a Sorvall RC5C centrifuge (SS34 or F21S -8x50y rotor) with additional filtration of the supernatant through a 0.45 μm membrane (Roth). Metal affinity chromatography was used as the first purification step, capturing the His-tagged subunits of the complex. This was

done either with a gravity column or a HisTrap chelating HP column (GE healthcare) on an Äkta purifier (GE healthcare). In case of gravity purification, either high performance nickel-sepharose (GE healthcare) or perfect pro nickel-NTA-agarose (5-prime) was used. 0.1 M solutions of NiCl2, Zn(CH3COO)2, CuSO4 or Co(CH3COO)2 were used for charging the affinity media. Alternatively, MBP-tagged proteins were purified using amylose resin (New England Biolabs) in our regular lysis buffer with pH adjusted to 7.5.

Bound protein was eluted by an increasing imidazole gradient. In some cases, prior to eluting the bound complex, an extra wash step was added to remove possibly bound liposomes from the proteins. In such cases, either 1% (v/v) Triton X-100 (Sigma) or 30 mM n-octyl-b-D-glucoside (b-OG, Glycon biochemicals) was added to the lysis buffer for wash.

To capture the FLAG-tagged IFT81, Anti-FLAG M2 affinity gel (Sigma) was used in buffer containing 20 mM Tris-HCl pH 8.0, 300 mM NaCl, and 5% glycerol. To elute bound proteins, either FLAG-peptide (Sigma) or 0.1 M glycine pH 3.5 were used according to the manufacture's manual.

For ion-exchange chromatography, affinity-purified protein was diluted with IEX-buffer 1 (20 mM Tris-HCl pH 8.0, 5% glycerol) to obtain a sodium chloride and imidazole concentration of less than 100 mM. The protein was loaded on a MonoQ 5/50 (GE Healthcare) equilibrated with IEX-buffer 2 (IEX-buffer 1 + 50 mM NaCl) and eluted with a linear gradient of up to 1 M NaCl.

The affinity- or ion-exchange-purified proteins were concentrated using Amicon Ultra Centrifugal Filters, (MWCO: 50 kDa or 100 kDa) and loaded on a size exclusion chromatography column (GE healthcare). Depending on the molecular weight of the target protein/target complex either Superdex 75, Superdex 200 or Sephacryl 400 16/60 columns (HiLoad; GE healthcare) were used, which were pre-equilibrated with SEC-buffer 1 (20 mM Tris-HCl pH 8.0, 100 mM NaCl, 5% glycerol) or SEC-buffer 2 (20 mM HEPES pH 7.5, 100 mM NaCl, 5% glycerol). In general, SEC-buffer 1 was used. SEC-buffer 2 was used only if subsequent biochemical analysis was incompatible with the Tris-HCl buffer.

5.3   Chemical cross-linking

25% glutaraldehyde (GA) solution was used for chemical crosslinking experiments. Prior to cross-linking, proteins were transferred into cross-linking buffer (20 mM HEPES, pH 7.5, 100 mM NaCl, 5% glycerol) and diluted to 0.5-1 mg/ml. GA was added with different concentrations in the range of 0.01%-0.1% (v/v) to protein solutions. The reaction was stopped at different time points by the addition of Tris-HCl (pH 8.0) to a final concentration of 100 mM. Cross-linking results were subsequently analysed by SDS-PAGE.

5.4   Electron microscopy

All electron microscopy experiments were carried out by Ekaterina Shimanovskaya (negative staining and image acquisition) and Marlene Brandstetter (rotary metal shadowing and image acquisition).

For all negative staining experiments protein at a concentration of approximately 100 μg/ml was adsorbed to glow-discharged grids and stained for 1 minute using 2% uranyl acetate with unadjusted pH.

Image acquisition was done on a Morgagni 268D electron microscope (FEI) at 80 kV. Image analysis was done using ImageJ (http://rsbweb.nih.gov/ij/).

5.5   Liposome binding assay

Liposomes were generated from Folch Type I lipids (Sigma, gift from the Martens lab at the MFPL), containing phosphatidylinositol, phosphatidylserine and other lipids. In short, 1 mg Folch type 1 lipids were mixed with 100 μl chloroform (Merck) and dried under argon stream. They were resuspended in binding buffer (20 mM Tris-HCl pH 8.0, 100 mM NaCl, 5% glycerol) to give a final concentration of 1 mg/ml, followed by repeated filtration through a 0.4 μm polycarbonate filter (Whatman, Nucleopore track-etch). Purified protein (10 μg) was incubated with freshly generated

liposomes for 30 minutes at room temperature prior to ultracentrifugation. Samples were centrifuged for 10 minutes at 68000 rpm using a TLA100 rotor (Optima TLX Ultracentrifuge, Beckman). The supernatant was collected and pelleted liposomes were resuspended in equal volume of binding buffer. Both supernatant and pellet were analysed on a coomassie-stained SDS-PAGE gel as well as by anti-His Western blot.

5.6   Western blot

Protein bands were transferred to the PROTRAN nitrocellulose membrane (Whatman) using a trans-blot semi-dry transfer cell (BioRad). Primary antibodies used were anti-His (1:1000; Calbiochem) or anti-DnaK (1:10000; Enzo) antibody. Anti-mouse IgG (H+L) alkaline phosphatase (1:10000; Promega) was used as a secondary antibody, using Sigma*FAST* BCIP/NBT tablets (Sigma) to develop the blot.

5.7   N-terminal sequencing

N-terminal sequencing was done at the Tuft Core facility (physiology department, Stearns Bldg. Rm 808 136 Harrison Ave, Boston, USA). The protein of interest was blotted to an Immobilion P-membrane (Milipore) and the respective band was clipped. To increase the blotting efficiency following protocol was used. Prior to blotting, the polyacrylamide gel was equilibrated in cathode buffer (25 mM Tris-HCl pH 9.4, 40 mM glycine, 10% methanol) for 15 minutes. Simultaneously, the membrane was prepared for blotting by soaking in 100% methanol for 15 seconds, washing in water for 2 minutes and equilibrating in anode buffer 2 (25 mM Tris-HCl pH 10.4, 10% methanol) for 5 minutes. The gel and the membrane were assembled between filter paper pre-wetted in anode buffer 1 (0.3 M Tris-HCl pH 10.4, 10% methanol) at the bottom and cathode buffer at the top, and run for 2 hours at 25 V with trans-blot semi-dry transfer cell (BioRad).

5.8   Mass spectrometry

Mass spectrometric analysis was done by the mass spectrometry facility of the Max F. Perutz Laboratories (Dr. Bohr-Gasse 3, 1030 Vienna, Austria). To avoid contamination by other proteinaceous materials, SDS-PAGE gels were prepared from fresh solutions and stained shortly with filtered coomassie staining solution. Desired bands were cut out in a sterile hood. A gel piece of an empty control lane was cut as a control sample.

5.9   TCA precipitation

TCA precipitation was done according to a protocol from Irene Gösler (Blaas lab, MFPL, Vienna). Briefly, 50% trichloroacetic acid (TCA) was mixed with the protein sample at a ratio of 1:4 and incubated on ice for 15 minutes. Protein was pelleted by centrifugation for 5 minutes at 14,000 rpm in a tabletop Eppendorf centrifuge. After discarding the supernatant, the pellet was washed by 300 µl of 20% ethanol and centrifuged again. This step was repeated twice. In the final step, the pellet was dried in a speed vac and resuspended in 10 µl respective sample buffer.

5.10   Linear sucrose gradient

Linear sucrose gradients were prepared using a gradient mixer, gradient station *ip* (BioComp; Marlovits lab, IMP, Vienna), in SW60 tubes. Gradients from 5-25% sucrose in sample buffer (20 mM Tris-HCl pH 8.0, 100-300 mM NaCl, 5% glycerol) were prepared at room temperature and cooled down for 1 hour at 4°C prior to centrifugation. Protein samples (<100 µl) were applied carefully onto the top of the gradient and centrifuged for 3.5 hours at 50000 rpm (TH-660 rotor, Sorvall 90 SE). A peristaltic pump was utilised to collect fractions between 300-400 µl (11 drops). Protein distributions along the gradient were analysed on an SDS-PAGE gel.

5.11 Additive test

Different additives (Table 3) were tested to check their influence on the oligomerisation state of IFT20. Purified protein was incubated with the chemicals for one hour at room temperature prior to loading on a 5% native-PAGE gel.

Table 3 Additive list.

Additives	Final concentration	Additives	Final concentration
Urea	1 M	Np-40	0.5 % (v/v)
Sodium chloride	300 mM,	Ammoniumsulfate	300 mM
	1 M	Potassium chloride	1 M
CHAPS	5 mM	PEG-8K	10%
Dithiotreitol	1 mM,	EDTA	1 mM
	10 mM	Magnesium chloride	200 mM

6   Results

6.1   Cloning of the 8 genes of the *T. brucei* IFT complex B core

Reconstitution of the complex B core from *T. brucei* was done in a bacterial expression system. To avoid the expression of insoluble or aggregated individual subunits, I opted for a strategy that allowed me to co-express all eight subunits together. The pETDuet system (Novagen) consists of four vectors – pETDuet, pCDF, pCOLA and pACYC, each carrying compatible replicons and different selection antibiotics (Figure 6).
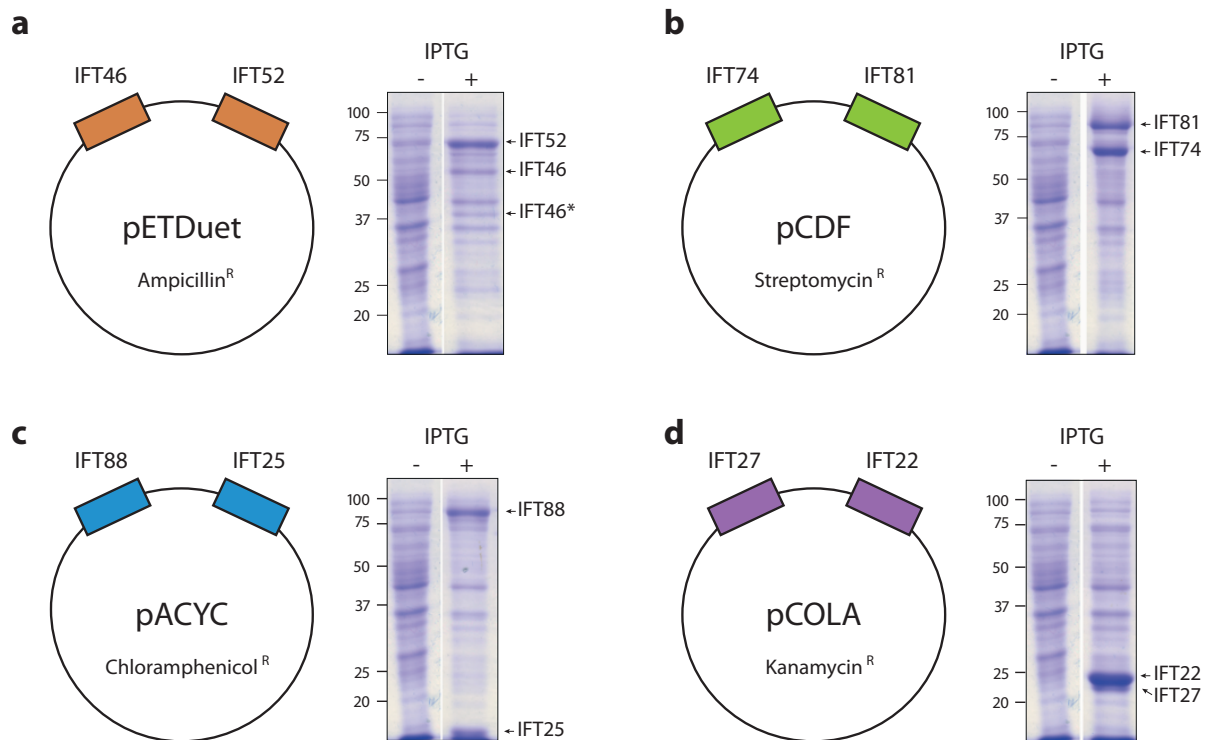
Figure 6 Expression of the *Tb* IFT-B core using the pETDuet system. (a-d) The eight different genes were cloned into the respective vectors as displayed. Expression of each set of subunits was tested separately in a small-scale expression test. The asterisk marks a degradation product of IFT46.

Using a stepwise approach, the IFT genes were cloned into one of the two multiple cloning cassettes (MCS) per vector. IFT74 and IFT81 were cloned into the same vector, based on the known interaction of these two subunits (Lucker et al., 2005). At the time when we designed the experiment, IFT46 and IFT52 were proposed to directly interact with each other, so they were grouped together into the pETDuet

45

vector. The remaining subunits were cloned solely based on available and/or optimal cloning sites for each gene.

Due to a cloning mistake, IFT27 was not expressed during the initial experiments. Even after re-cloning, the expression level of IFT27 was much lower than that of other core members (Figure 6d). It was reported previously that the majority of the sub-complex of IFT27 - IFT25 is not associated with the remaining IFT complex B outside the flagellum (Wang et al., 2009). Since I was able to pull-down the remaining subunits in the absence of IFT27, IFT27 is seemingly not essential for the assembly of the remaining recombinant complex proteins.

For IFT46, in the N-terminal, unstructured region a substitution (M45I) was present in all clones. The *Chlamydomonas* homologue of IFT46 does not depend on its first 89 amino acids in order to be able to bind to its binding partner IFT52 (Lucker et al., 2010). All sequenced clones of IFT74 contained an insertion of a six amino acid motif ('PGSQMR') in the N-terminal region after amino acid R35. While this six-residue motif 'PGSQMR' is repeated three times in the published IFT74 sequence, it is repeated an additional fourth time in the used construct.

In order to co-express all subunits together, the four constructs were co-transformed into one host cell, BL21(DE3). Initially, all co-transformation trials of the four plasmids together did not succeed, even though they were done according to the protocol from Novagen. To circumvent this problem, I opted to co-transform only two vectors at a time. Bacteria containing the two plasmids were used to prepare new chemically competent cells and the remaining two vectors were co-transformed into these cells. This approach proved successful as indicated in the expressions of all proteins together in one host cell shown below (Figure 7a).

6.2 Co-expression in a heterologous bacterial expression system

To purify the core complex from *E. coli* cell lysate, IFT46 and IFT81 were cloned with a C- and an N-terminal 6×His tag, respectively. In a small-scale expression test of each individual vector containing two complex B core members, the expression of all

subunits was observed (Figure 6). With the exceptions of IFT27 and IFT22, the expression levels of other proteins were comparable. IFT22 was much more abundantly expressed than IFT27 (Figure 6d).

For IFT46 and IFT52 (in pETDuet vector) an extra faint band was observed at approximately 38-39 kDa (Figure 6a). This band could also be detected via anti-His Western blot analysis (Figure 7a), suggesting that it represents either an N-terminal degradation product of IFT46 or a C-terminal one of IFT81. To sort this out and to find the proteolysis site, the band was cut and sent for N-terminal sequencing (Figure 7b), which showed that the first six amino acids are 'SLKNNP', with high confidence for the second, third and fifth residue. With the exception of the first residue serine, the other five amino acids are found in the IFT46 sequence from position 98 onwards. Thus, the first 97 amino acids of IFT46 are enzymatically degraded after expression, giving rise to the shorter band of a theoretical molecular weight of 38 kDa, consistent with the observed band. Analysing the secondary structure of IFT46 suggested that the first ~175 amino acids are disordered and likely more accessible for proteolytic degradation.

6.3 Purification and verification of the recombinant complex

To test whether the recombinant proteins are able to form a stable complex, IFT88, IFT74, IFT52, IFT25, IFT22 and, in later experiments, IFT27, were pulled down via their interaction with IFT46-His and His-IFT81 (Figure 7a, c).

Initial purification trials were done using gravity affinity purification. Tests of different metal ions in their ability to bind the 6×His tag indicated that copper and zinc are more effective than nickel and cobalt. Thus, either Zn^{2+} or Cu^{2+} charged affinity media was used in the initial purification step of the recombinant complex.
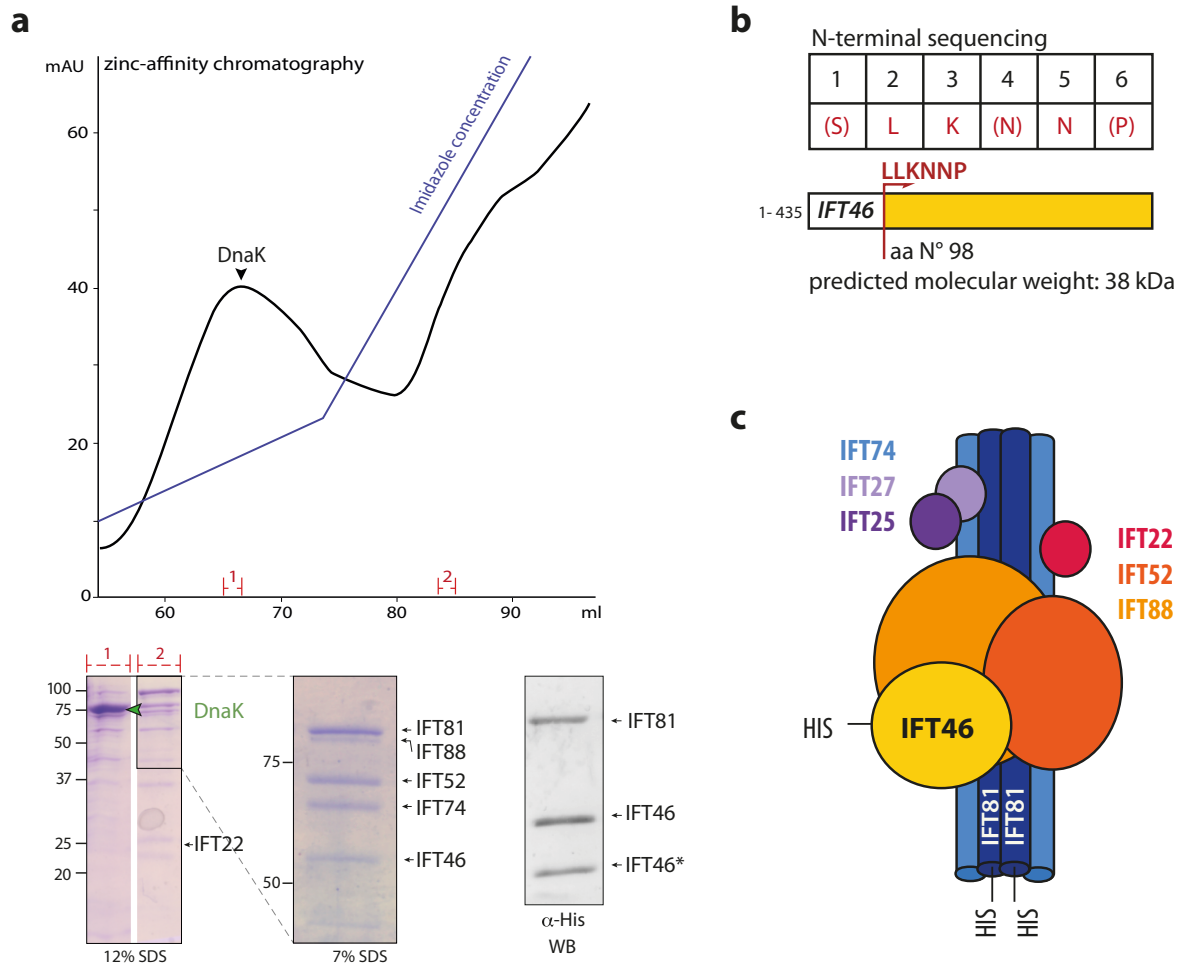
Figure 7 Reconstitution of the IFT complex B core. (a) Zn^{2+} affinity chromatography was used to capture both IFT46-His, His-IFT81 and other 5 core-subunits. Commassie-stained SDS-PAGE and Western blot were used to detect the proteins of interest. (b) N-terminal sequencing identified a degradation product of IFT46. The asterisk marks the degraded IFT46 in (a). (c) Schematic representation of the recombinant complex captured on the affinity matrix.

Due to their similar molecular weights, IFT81 and IFT88 bands are overlapped on the SDS-PAGE gel if acrylamide above 10% (w/v) was used (Figure 7a). A strong band at around 74-75 kDa was observed that was initially suggested to be IFT52 based on its theoretical molecular weight. Surprisingly, however, this band was also detected on an SDS-PAGE gel during the purification of IFT74-IFT81 alone, although it is less intense than in the co-expression experiments of the core proteins. Therefore, I used mass spectrometry (MS) to identify the unknown band as well as to verify the other protein bands of the IFT complex B core. The overlapped IFT88 and IFT81 bands were cut together and both proteins were correctly identified by MS, as were IFT74 and IFT22. The band corresponding to IFT46 was not sent for MS, since it had

already been identified by anti-His Western blot. Interestingly, a few polypeptides matching IFT46 were detected in the IFT22 MS results. Although both proteins have different molecular weights, fragments of IFT46 might have migrated together with IFT22 on the SDS-PAGE, thus giving rise to the identified peptides. MS-analysis of the IFT52/unknown band revealed two prominent proteins. Aside from the expected IFT52, the *E. coli* chaperone protein DnaK (protein ID 15799694) was also detected. As mentioned earlier, chaperones can be found at the flagellar tip and the *Chlamydomonas* chaperone Hsc70 is able to interact with IFT components (Bhowmick et al., 2009). A BLAST search showed a sequence identity between *E. coli* DnaK and *T. brucei* Hsp70 of 49%. It is not clear if the co-purification of DnaK is based on its folding activity of potential unfolded sequences in the target complex or, in the absence of the chaperone Hsp70, DnaK mimics Hsp70 to bind to one or several of the core proteins.

During all purifications, IFT27 and IFT25 were low abundant and could not be verified by MS. Aside from mass spectrometry, IFT46 and IFT81 (as well as the N-terminal degradation product of IFT46) were also verified via Western blot analysis, using anti-His antibody (Figure 7a, lower panel). To further improve the affinity purification, IFT81 was cloned with a FLAG-tag (sequence: DYKDDDDK). Interestingly, it was not possible to elute the majority of the complex from the FLAG-beads. Only minor fractions of the proteins eluted, independently of the used elution method. Therefore, 6×His-tagged IFT81 was used for all subsequent purifications of the complex.

To remove the *E. coli* chaperone protein DnaK from the reconstituted complex, addition of 5 mM Mg^{2+}-ATP, both in the presence and absence of a mixture of denatured *E. coli* proteins, was tested (Rial and Ceccarelli, 2002). Denatured proteins were produced from BL21 cell lysate by heating the supernatant for 10 minutes to 90°C. Both approaches improved the removal of DnaK, suggesting that - at least to some extent - DnaK is associated with the complex via its chaperone function. I also found that a two-step imidazole gradient during the initial affinity chromatography step (carried out on an FPLC system) was effective in removing DnaK (Figure 7a). The chaperone could be mostly removed during a flat gradient from 50-70 mM imidazole, whereas the recombinant complex subsequently eluted together in a

second peak from the affinity matrix containing 150-200 mM of imidazole (Figure 7a).

6.4 Assessment of the oligomeric states

To assess the oligomeric state and the homogeneity of the affinity-purified proteins, size-exclusion chromatography was used. The proteins consistently co-eluted in a shoulder peak, ranging from 5 MDa to approximately 600 kDa (Figure 8). If present, IFT27 seemed to be low abundant and could not be clearly detected on the SDS-PAGE, which was similar to IFT25. A current model suggests that the core complex is composed of two copies of IFT81 and IFT74, and one copy of each of the remaining members. This would correspond to an assembly with a molecular weight of approximately 570 kDa ('single complex'). The data shown here indicates that the complex core has different oligomeric states, ranging from the current working model up to larger particles and potential aggregates. The composition of the higher oligomeric assemblies is unknown. Due to the high heterogeneity of the complex observed on the size-exclusion chromatography, the sample was not suitable for crystallisation trials. To improve the purification, arginine and glutamic acid were added following a protocol that has been shown to work in other protein purifications (Golovanov et al., 2004). However, no change in the elution profile was observed. Interestingly, upon addition of $CaCl_2$ and $MgSO_4$ (Bhogaraju et al., 2011), a small shift towards the 'single complex' was observed (Figure 8b), with less protein in the void volume compared to the normal buffer (Figure 8a).

Aside from the heterogeneity of the complex, expression yields of the eight subunits were not consistent. Different batches of purified core complex had significant variations in the amount of pure proteins. Therefore, low yield and heterogeneity of the reconstituted complex prevented the successful crystallisation of the core complex.
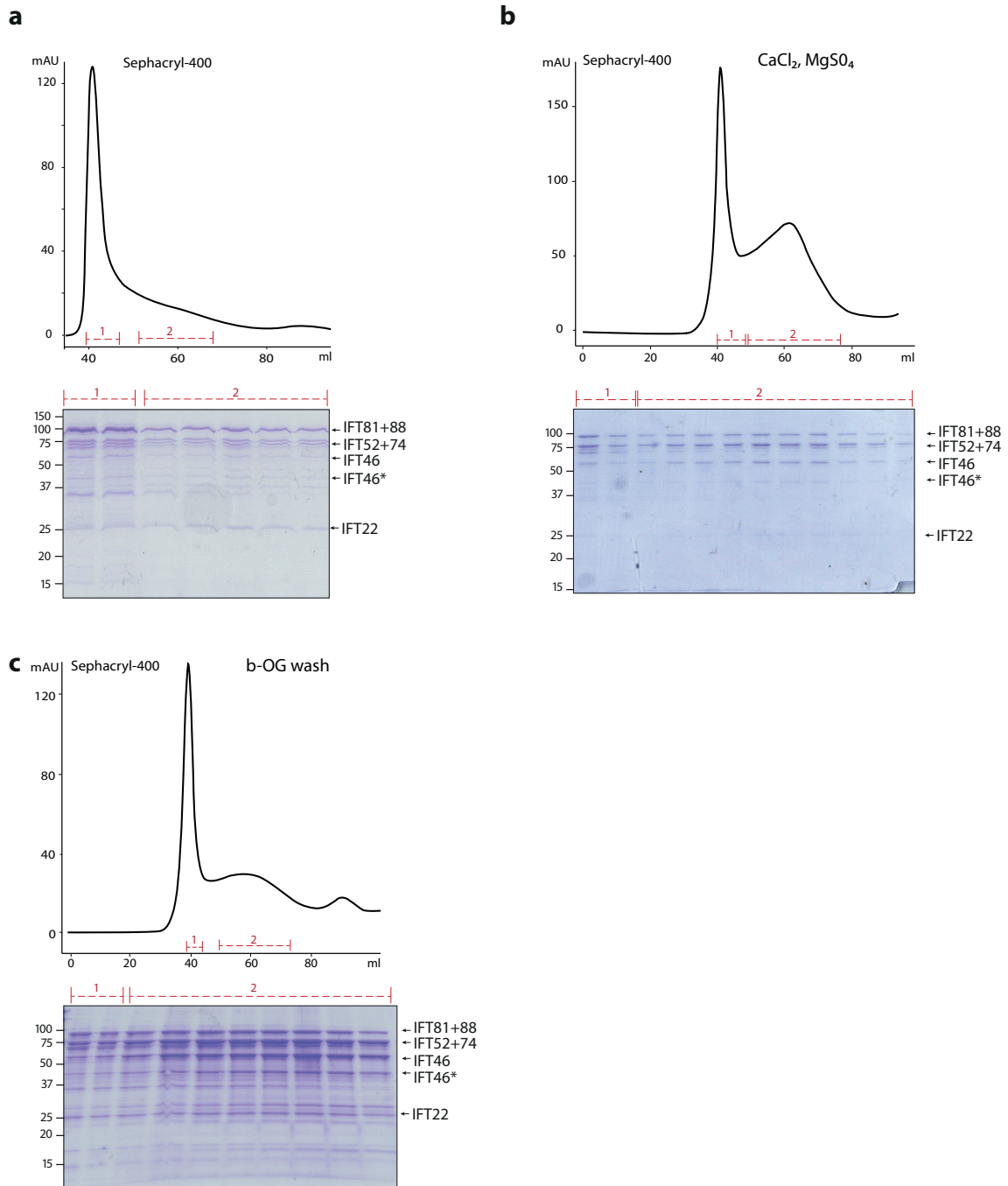
Figure 8 Size-exclusion chromatograms of IFT complex B core proteins after affinity purification. (a) The core proteins, except for IFT27, were loaded on the gel filtration column Sephacryl 400 (16/60). IFT25 was low abundant. (b) All eight proteins were co-purified in a buffer containing $MgSO_4$ and $CaCl_2$. IFT27 and IFT25 could not be detected. (a,b) Equal amounts were loaded on the SDS-PAGE. (c) SEC elution profile after removing potential lipid contamination using b-OG. Lanes 1 and 2 were respectively loaded with 25% and 50% of the amount loaded in the remaining lanes.

During multiple size-exclusion purifications of the core subunits it was observed that the UV absorbance at 280 nm did not correspond to the protein amount on an SDS-

PAGE (Figure 8a & b, SDS-PAGE gels). Since lipids have a UV absorbance at 280 nm but could not be stained on an SDS-PAGE, it could be possible that they were present in the observed aggregation peak. To remove the potential lipid contamination, I washed the complex bound to the affinity matrix using buffers containing either 1% Triton X-100 or 30 mM n-octyl-b-D-glucoside (b-OG) before eluting the polypeptides. The SEC-elution profile of the complex washed with b-OG during the affinity purification (Figure 8c) showed a more defined nonaggregated peak after the void-volume peak, similar to the purification results with $CaCl_2$ and $MgSO_4$ (Figure 8b).

6.4.1 Linear Sucrose Gradient

Large protein complexes are often purified using density centrifugation as an alternative to size-exclusion chromatography. To test whether this approach could be more suitable for separating the recombinant IFT complex B core, linear sucrose gradient ultracentrifugation was used (Figure 9). The affinity-purified proteins were loaded on the gradient. All fractions were analysed on a SDS-PAGE gel. The top fractions, containing low molecular weight proteins or molecules unable to enter the gradient, showed a strong band of around 24 kDa, which is likely an *E. coli* protein. The majority of the core proteins co-migrated in the gradient, with the major peak appearing in fractions 4-6 from the top of the gradient. Most of the proteins could be observed in all fractions of the gradient. This is consistent with the SEC data that showed different oligomeric states of the core complex (Figure 8).

To test whether the *T. brucei* homolog of DnaK, Hsp70, is capable of binding to the complex, MBP-tagged Hsp70 was co-expressed with the complex. Interestingly, the gradient fractions 4-6, where the core complex was peaking, were the fractions with the least amount of Hsp70 (Figure 9b). The majority of Hsp70 was found at the bottom of the gradient. These results show that Hsp70 associates with the larger, potentially aggregated fractions of the IFT-B core complex, but not with the 'single complex'.
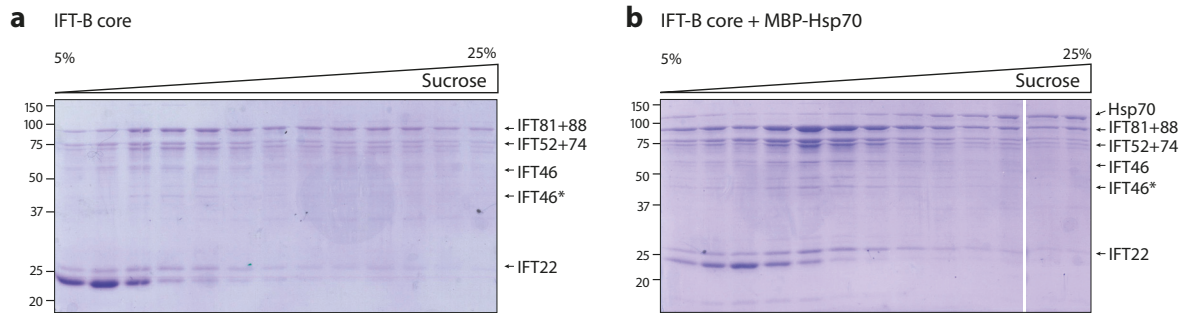
Figure 9 Linear sucrose gradient ultracentrifugation. (a) All eight affinity purified proteins were loaded on the sucrose gradient. (b) The eight core proteins co-purified with MBP-Hsp70 were affinity purified and loaded on the sucrose gradient. Fractions were collected using a peristaltic pump.

6.5 Expression of the recombinant complex in a DnaK deletion strain

To investigate potential differences in the expression of the core-complex in the absence of DnaK, the DnaK deletion strain EN2 was tested (Ratelade et al., 2009). Due to the kanamycin selection marker of this cell line, our pCOLA vector containing IFT27 and IFT22 could not be co-transformed. Thus, purification of only IFT88, IFT81, IFT74, IFT52, IFT46 and IFT25 was tested. The six-protein complex was purified using Cu-NTA affinity chromatography. The suppression of DnaK in this cell line was verified with anti-DnaK Western blot analysis (Figure 10b). The affinity purified 6-protein complex from EN2 cells was used for Western blot. A strong signal for DnaK was detected for the control BL21-cells but none for the core complex expressed in EN2 cells. Thus, DnaK is successfully suppressed in the EN2 cell line.

Size-exclusion chromatography showed a similar elution profile of the complex compared to previous purifications in BL21(DE3) (Figure 8, Figure 10a), indicating no influence of DnaK on the oligomeric state of the complex. A chemical cross-linking experiment with glutaraldehyde showed the cross-linking of the six core-subunits. The cross-linked band had a very large molecular weight and could only be seen at the top of the gel (Figure 10c).
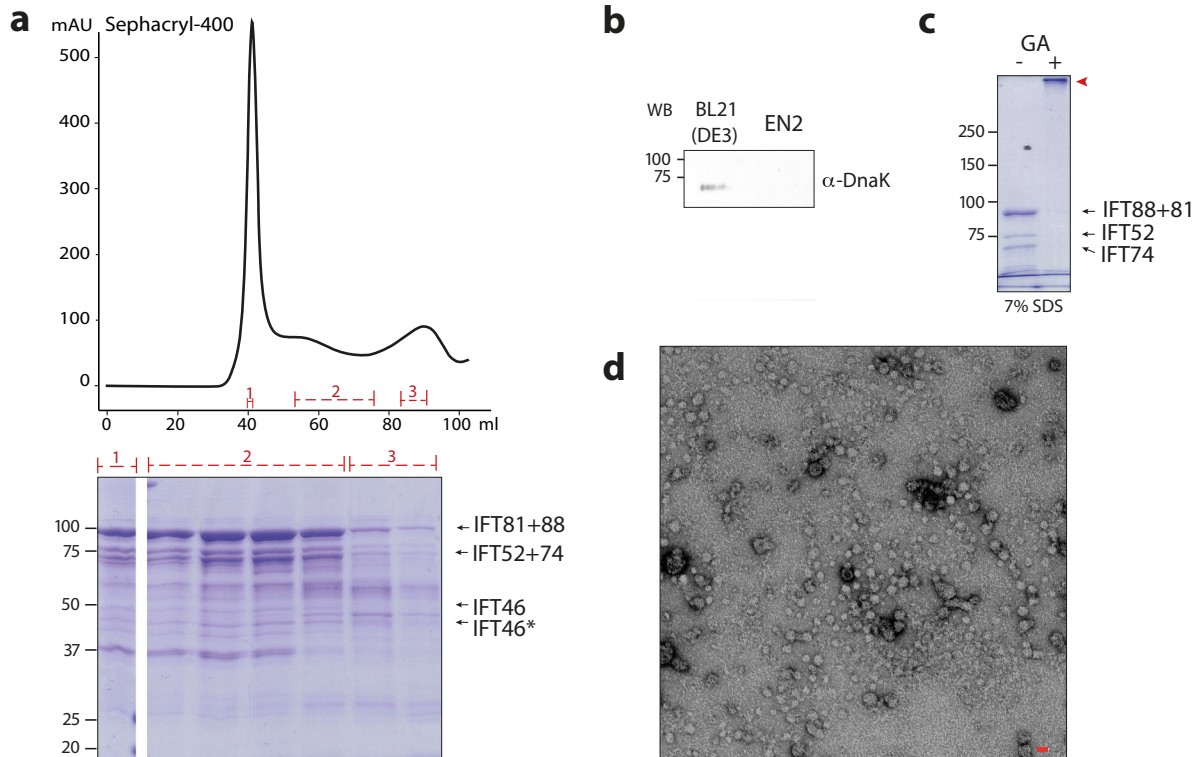
Figure 10 Test of protein expression in the DnaK-deletion EN2 cell line (a) Affinity-purified complex was loaded on a Sephacryl-400 (16/60) column. For the SDS-PAGE, equal amounts of sample were loaded for peak 2 and 3. For lane 1, a third of the sample volume was loaded compared to other fractions. (b) Anti-DnaK Western blot. Bl21(DE3) cell lysate was used as the positive control. (c) Chemical cross-linking using 0.05% glutaraldehyde (GA) for 1 minute at room temperature. The red arrow marks the high-molecular weight species that was unable to enter the gel. (d) Peak 2 of panel (a) was combined and used for negative staining electron microscopy studies. Scale bar (red): 20nm

Fractions from size-exclusion chromatography (Figure 10a, peak 2) were used for negative staining EM studies (Figure 10d) to check whether the sample contains prominent structures that represent the complex composed of IFT88, IFT81, IFT74, IFT52, IFT46 and IFT25. Roundish particles, between larger, dark assemblies, could be observed with sizes between 10 and 16m. If an overall globular shape of the complex were assumed, structures with a diameter of approximately 10.7 nm would be expected. Further studies are needed to verify if the particles are IFT complex B core proteins or may be liposomal contamination.

6.6 IFT74 and IFT81 form a stable sub core-complex and interact with Hsp70

Yeast-two hybrid studies have shown the interaction between *Chlamydomonas* IFT74 and IFT81 (Lucker et al., 2005). To investigate whether the homologous proteins in *T. brucei* also interact in a recombinant system, IFT74 and IFT81 in pCDF were co-expressed and co-purified. Furthermore, the interaction of the two proteins with MBP-Hsp70 was tested. Zn^{2+}-affinity chromatography was used to capture His-IFT81 and its binding partner IFT74. MBP-Hsp70 is also pulled-down (Figure 11a). To exclude that Hsp70 is only binding to IFT81-IFT74 via its chaperone function, 4 mM ATP and 20% glycerol were added to the buffers. No difference in the binding of the three proteins was observed (Figure 11d).

Alternatively, amylose beads were used to pull-down MBP-Hsp70 and associated molecules (Figure 11b). Interestingly, only MBP-Hsp70 was strongly enriched on the amylose beads. This is probably due to the much higher expression level of MBP-Hsp70 compared to IFT81 and IFT74 and only a fraction of the expressed MBP-Hsp70 is binding to IFT74-IFT81 in solution.

To check the homogeneity and stochiometry of the hetero-trimeric complex, the Zn^{2+}-purified macromolecules were loaded on a size-exclusion column. Two different peaks were observed, aside from an aggregation peak in the void volume of the column (Figure 11c). Peak number 2 showed the trimeric assembly at a molar ratio of 1:2:2 (Hsp70:IFT81:IFT74). Seemingly, the heterotetramer of 2xIFT81 and 2xIFT74 binds to one molecule of Hsp70. The third peak contained excess Hsp70, although trace amounts of IFT81 and IFT74 were also detected. The 1:2:2 stochiometry of the trimeric complex and the higher expression levels of MBP-Hsp70 explain the minor amounts of IFT74 and IFT81 that were captured by Hsp70 on the amylose beads given the much higher level of Hsp70 than the two IFT proteins (Figure 11b). The trimeric complex was examined by rotary shadowing electron microscopy to study the arrangement of the three proteins, but no consistent structures were observed on the grids (data not shown).
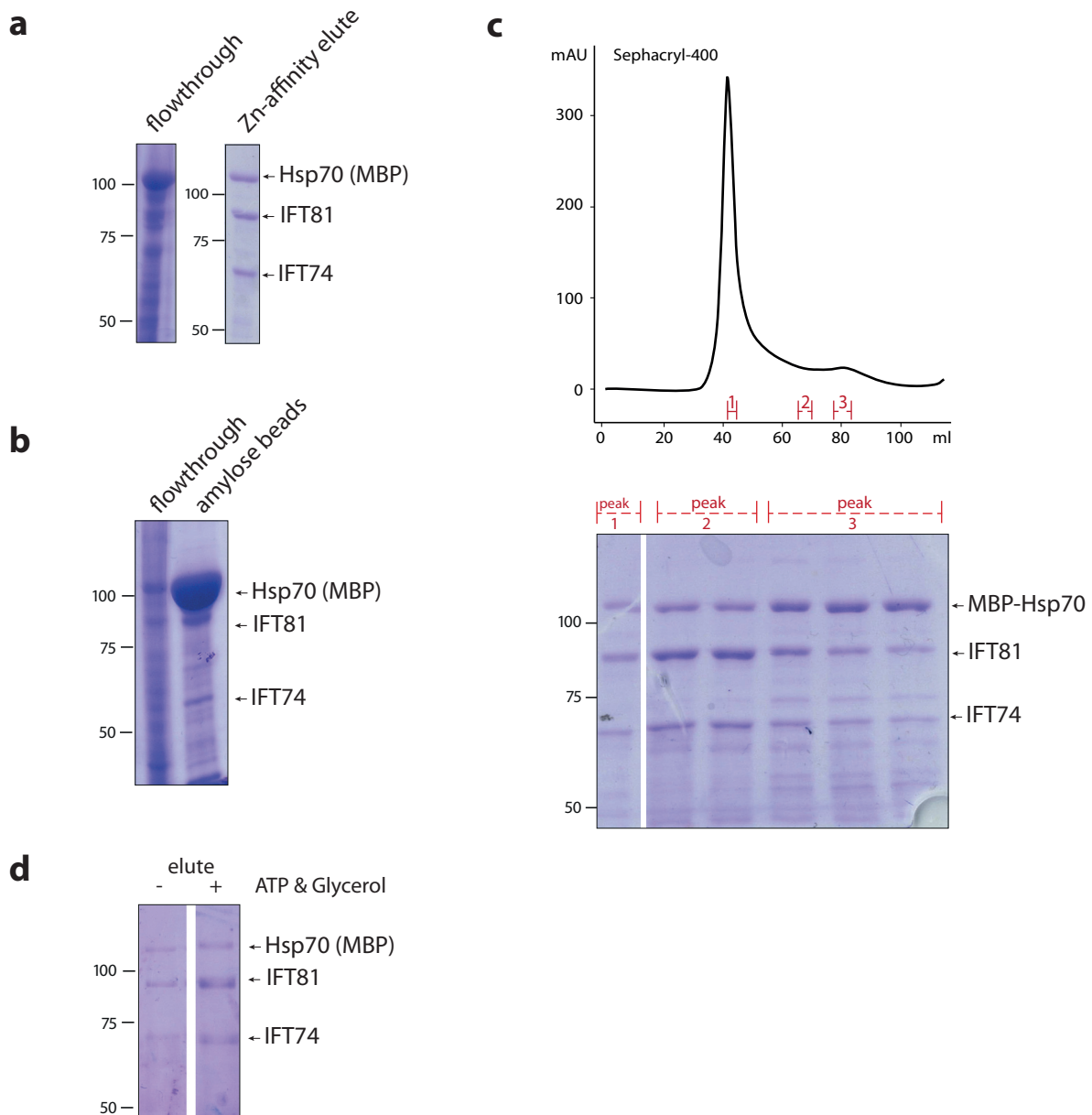
Figure 11 Purification of the IFT74/IFT81/Hsp70 complex. (a,b) Cell lysate was split half/half and separately loaded on a Zn-HiTrap column and an amylose resin. SDS-PAGE gels show the flow-through and (a) eluted proteins or (b) the amylose-bound proteins. (c) The eluent of the Zn^{2+} affinity purification was loaded on a Sephacryl-400 (16/60) column and fractions were analysed on an SDS-PAGE gel. (d) Zn-NTA HiTrap elute fractions, where prior to elution a wash with ATP and glycerol had been included or not.

6.7   The IFT complex core proteins bind lipids

To elucidate whether the complex is capable of binding lipids, liposome-binding assays were conducted (Figure 12). A size-exclusion chromatography peak fraction of

the core complex (where a detergent wash had been included during the prior affinity chromatography step) was analysed. Western blotting using anti-His antibody showed that IFT46 was pulled down by liposomes (Figure 12b). IFT81 was not detected in any fraction, which could be due to an unsuccessful transfer onto the nitrocellulose membrane or insufficient expression.
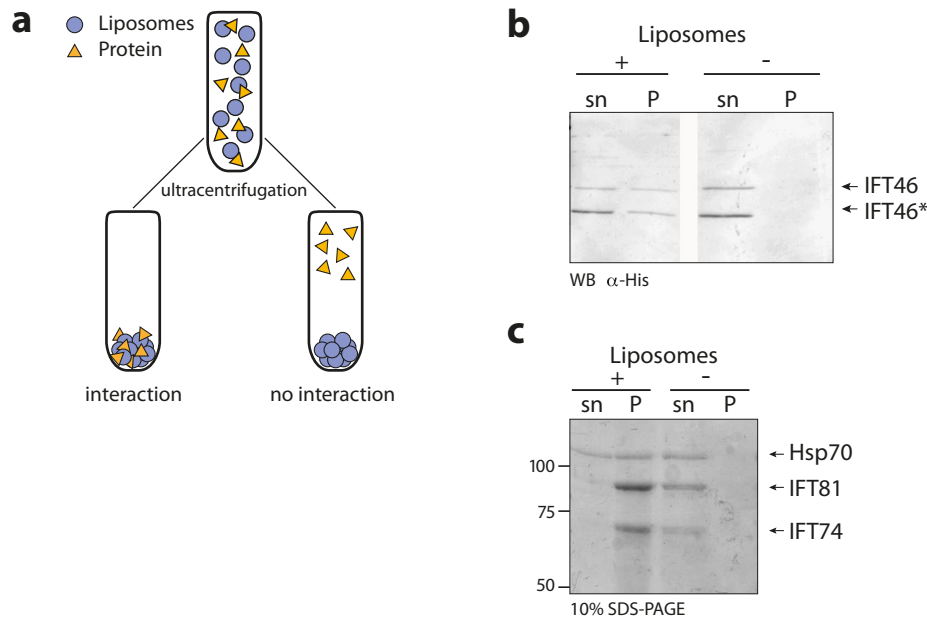
Figure 12 Liposome binding assay. (a) Schematic representation of the liposome binding assay. (b) Purified IFT complex B core proteins were incubated with liposomes. Supernatants (sn) and pellets (P) were run on a 12% SDS-PAGE and IFT46 was detected by anti-His Western blotting. (c) The purified protein sub-complex composed of IFT74, IFT81 and Hsp70 was used for the liposome binding assay. The majority of the complex proteins were pulled down by liposomes.

The sub-core complex consisting of IFT74 and IFT81 together with the potential binding partner Hsp70 was also tested. MBP-Hsp70, IFT81 and IFT74 were only pelleting in the presence of liposomes. While all IFT81 and IFT74 proteins bound to liposomes, only ~60% of MBP-Hsp70 was pelleted. The un-pelleted Hsp70 is likely to represent the fraction of the polypeptide that is not bound to IFT74-81. The results of sub-core complex of IFT74 and IFT81 indicate a liposome-binding capability. In conclusion, the complex core proteins are able to bind to liposomes.

6.8   Analysis of the peripheral IFT-B subunit IFT20

Among all components of the IFT complex B, the peripheral subunit IFT20 is the only one localising to the trans-Golgi network. It was suggested to be involved in the selective transport of cilium-destined vesicles to the ciliary base. The unique distribution pattern and the relatively small size of IFT20 make it an intriguing target for structural studies.

IFT20 from *T. brucei* was cloned to a homemade vector (HM15b), which provides a cleavable N-terminal 6xHis-tag. Secondary structure analysis predicted the protein to be composed mainly of α-helices. Moreover, 50% of the protein was computed to assemble into a coiled coil (Figure 13).

Figure 13 Bioinformatic analysis of IFT20. (a) Using the secondary structure prediction server PSIPRED (Buchan et al., 2010; see section 9), the amino acid sequence of IFT20 was analysed. Pred = prediction (b) The online software COILS (Lupas et al., 1991; see section 9) was used to compute the probability of IFT20 to assemble into coiled coils.

Initial purification was carried out using Ni-NTA affinity chromatography. To remove minor impurities, the protein was subjected to an ion-exchange chromatography prior to SEC. The protein eluted in two peaks on a gel filtration column – dimer and tetramer, with the predominant amount of the protein being in a tetrameric state (Figure 14a).
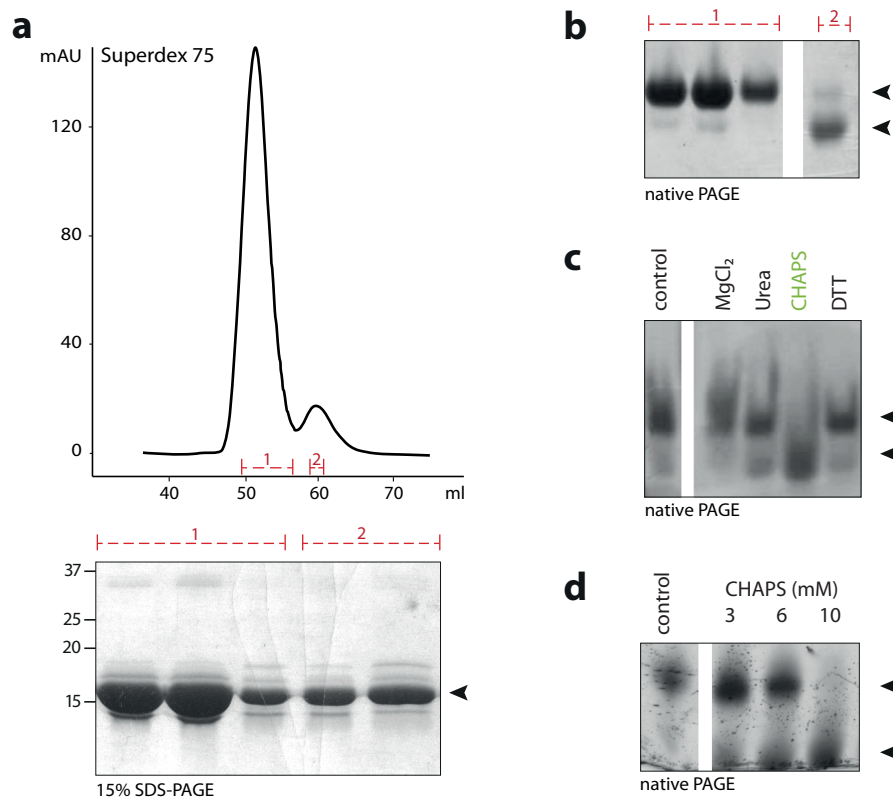
Figure 14 Purification and characterisation of *T. brucei* IFT20. (a) The Ni-NTA affinity purified IFT20 was loaded on the size-exclusion column Superdex-75 (16/60). Two distinguishable peaks with different amounts of protein were observed. (b) Fractions of the SEC-run of panel (a) were analysed on a 5% native gel. (c) Different additives were added to the purified protein and samples were loaded on a native-PAGE to check for the influence of the additives onto the protein oliogomeric states. (d) Different concentrations of CHAPS were tested.

To assess the homogeneity within both peaks, a native gel was run. A clear shift between the two species can be observed (Figure 14b). The dimeric fractions contain trace amounts of the tetrameric protein and vice versa. To further investigate whether it is possible to shift the oligomerisation states of IFT20, different additives were tested. Fraction of tetrameric IFT20 were incubated with the additives and analysed on a native polyacrylamide gel. Among the diverse set of chemicals, CHAPS resulted in a strong shift from the tetrameric to the dimeric state (Figure 14c, a subset of

additives is shown here). Different concentrations of CHAPS and the influence on the tetramer to dimer shift were studied. While 3 mM CHAPS did not result in a significant change, 10 mM CHAPS shifted IFT20 nearly completely into the dimeric state (Figure 14d). It is worth noting that 10mM corresponds to the critical micelle concentration of CHAPS. However, re-purifying IFT20 in a buffer containing 10mM CHAPS, resulted in a different elution profile, with a 50:50 ratio of tetramer and dimer (Figure 15a).
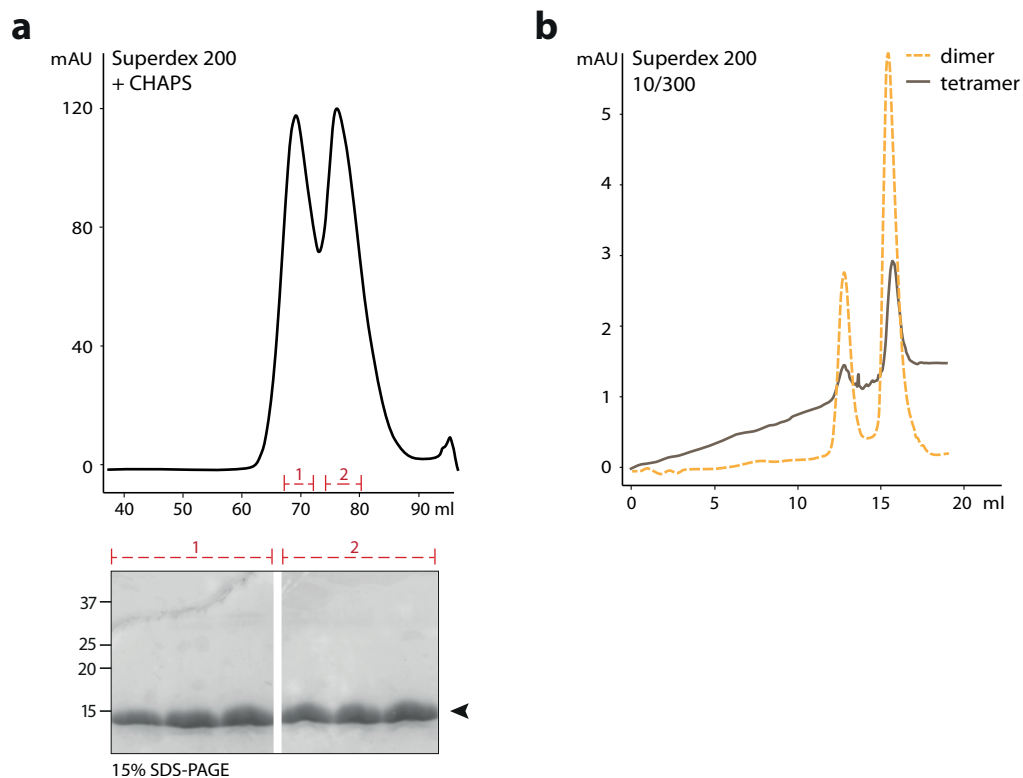
Figure 15 Re-purification of *T. brucei* IFT20 in the presence of CHAPS. (a) An SEC elution profile of the re-purified IFT20 in the presence of 10mM CHAPS. Equal amounts were loaded on the SDS-PAGE. The arrow marks IFT20. (b) Re-loading either peak 1 ("tetramer") or peak 2 ("dimer") in (a) on an analytical gel filtration column Superdex 200 (10/300).

Subsequently, re-purifying IFT20 in a buffer containing 10mM CHAPS, resulted in a different elution profile, with a 50:50 ratio of tetramer and dimer (Figure 15a). Interestingly, re-loading either the dimeric or the tetrameric IFT20 on an analytical size-exclusion column showed the protein to elute again in two peaks (Figure 15b), indicating that the protein is in equilibrium between the two states. Crystallisation trials of IFT20 with and without the addition of CHAPS were conducted, but no crystals have been obtained.

7 Discussion

Since the discovery of intraflagellar transport in 1993 (Kozminski et al., 1993), tremendous advances in understanding the principles of the process have been made (Blacque et al., 2008; Finetti et al., 2009; Sedmak and Wolfrum, 2010). However, the structural mechanism of IFT still remains largely unclear. It is possible to isolate the IFT complexes from *Chlamydomonas* but the yield and the purity are inadequate for structural studies (Behal et al., 2009). To circumvent both the impurity and the low yields, a co-expression strategy has been taken to produce individual proteins of the IFT complex B core in a bacterial expression system. The pETDuet system allowed us to co-express the entire eight core proteins. Despite the shortcoming of not being able to co-transform the four plasmids at the same time, but rather in a stepwise process, I managed to express the recombinant core complex in bacteria.

7.1 Reconstitution of the *T. brucei* IFT complex B core

It was possible to purify the complex with affinity tags on only two of the 8 core subunits – IFT46 and IFT81. This shows that the subunits of the IFT complex B core purified from *E. coli* interact and assemble into a complex. Interestingly, Ni^{2+} was not sufficient in capturing the 6×His-tagged subunits. Other metal ions were tested and Zn^{2+} and Cu^{2+} were found to be better suited in binding the 6×His-tagged proteins. It has been published that Zn^{2+} is superior to Ni^{2+} metal affinity due to its reduced binding affinity for *E. coli* proteins (Gaberc-Porekar and Menart, 2001). Cu^{2+} on the other hand is known to bind to even a single exposed histidine.

Six of the eight IFT complex B core subunits have been verified either via mass spectrometry or by anti-His Western blots. IFT27 and IFT25, which were both low abundant and hard to be recognised on an SDS-PAGE gel, were not verified with either method. IFT27 was significantly lower expressed than its expression partner IFT22 on the vector pCOLA (Figure 1d). In the recent publication by Bhogaraju and colleagues (Bhogaraju et al., 2011), they showed that recombinant *Cr*IFT27 was strongly stabilised by its binding partner IFT25. It might be possible that in addition

to the low abundance, recombinant IFT27 is degraded easily. Future studies should include an affinity tag at the N- or C-terminus of IFT27 to test this hypothesis.

As described previously, IFT27 and IFT25 are part of IFT complex B isolated from *Chlamydomonas* flagella (Cole et al., 1998; Wang et al., 2009; Lechtreck et al., 2009). However, within the cytoplasm they can be found at a separate location from the other complex B proteins (Wang et al., 2009). It cannot be excluded that the recombinant complex might be less stable than its *in vivo* counterpart. Notably, both proteins are not conserved in *C. elegans* and *D. melanogaster* (Qin et al., 2007; Lechtreck et al., 2009). In conclusion, although detectable in small-scale experiments, IFT27 and IFT25 are less stably integrated into the core complex in the recombinant system used here than *in vivo*. The absence of IFT27 did not influence the purification of the other core proteins in a detectable manner.

During the first affinity purification step, the *E. coli* chaperone protein DnaK was co-purifying with complex B proteins as was verified by mass spectrometry. Interestingly, chaperone proteins of the Hsp70 family can be found at the flagellar tip region (Shapiro et al., 2005). Since their transport is likely to be mediated by IFT particles, it could be possible that DnaK binds to the complex in a similar manner as Hsp70-IFT interaction. The majority of DnaK can be removed from the complex during the affinity chromatography step, indicating that the binding is not strong. However, it cannot be ruled out that members of the recombinant complex are not completely folded, thus activating DnaK binding.

7.2 Does the IFT complex B core assemble into structures similar to the IFT particle?

During multiple size-exclusion purifications, it was observed that the complex consistently eluted in different oligomeric states. Aside from the potential "single complex", the recombinant proteins seem to form higher order structures and/or large aggregates. Similarly, using linear sucrose gradient ultra-centrifugation as an alternative approach to gel filtration, the complex was found in all fractions, from the top of the gradient to the bottom, although the complex was more enriched in

fraction 4-6 from the top. It has to be noted, that the composition of the larger structures is unknown, in part due to the extended coiled-coil structures of IFT74 and IFT81 that prevent the measurement of the exact molecular weight of the recombinant complex by means of gel filtration. Using the DnaK deletion strain EN2 to co-express IFT88, 81, 74, 52, 46 and IFT25 and to test the influence of the chaperone protein did not show a change in the purification. The complex still eluted in a large shoulder peak on the size-exclusion column, indicating again different oligomeric states.

Studies have shown that trains of IFT particles with several single IFT-A and -B complexes arranged in a chain-like manner, move along the axoneme within the cilium (Pigino et al., 2009). Whether the reconstituted IFT complex B core assembles into similar larger structures even in the absence of IFT-A proteins is unknown but tempting to speculate. The different oligomeric states of the complex observed on size-exclusion chromatography proved to be one of the main obstacles for successful crystallisation. A homogeneous protein sample is indispensable for crystal growth. Therefore, many of my efforts have focused on obtaining a more homogeneous sample. Arginine and glutamic acid have been shown to improve solubility and long-term stability of other proteins (Golovanov et al., 2004). However, no significant difference in the elution profiles of the core complex upon the addition of these additives was noted. Recently, the crystal structure of IFT27-25 was published (Bhogaraju et al., 2011). In their purification protocol, $CaCl_2$ and $MgSO_4$ were added to all buffers. When I used both additives during a purification of the complex, a more defined peak of the 'single' complex was observed (Figure 8b).

7.2.1 Hsp70 associates with the higher oligomeric assemblies

Interestingly, purifying IFT88, -81, -74, -52, -46 and -25 together with Hsp70 in EN2 cells on a sucrose gradient showed that Hsp70 is not part of the fraction of the complex that migrates to the middle of the gradient. Hsp70 was exclusively found in the bottom fractions (Figure 9b). This implies that this part of the core complex may be aggregated and Hsp70 is associated with the proteins via its chaperone function.

7.3 Obstacles during the reconstitution of the IFT complex B core

The two biggest obstacles during the purification of the complex were the large yield fluctuations and reproducibility problems. Whether glycerol stocks or a fresh transformed cell were used, protein yield was inconsistent and independent of the amounts of grown cells. Inducing the cells at an O.D. of 0.9-1 stabilised the yield to some extent. Although I have managed to partially purify the recombinant complex B core from *E. coli*, the observed inconsistent yield and sample heterogeneity indicate that a eukaryotic expression system might be better suited for producing the core complex. Post-translational modifications might be able to stabilise the assembly and enable the purification of a less heterogeneous sample. For insect cell expression, the multiBac system (Berger et al., 2004) would be a reasonable approach to co-express the eight-proteins of the core complex. Once the expression can be verified, it is possible to scale up the protein yield for biochemical and structural studies. In addition to the core-complex, other sub-core complexes, such as IFT46-IFT52 with or without IFT88, are also worth to be studied by protein crystallography (Lucker et al., 2010).

As an alternative to crystallisation, electron microscopy studies could give some insights into the overall 3-dimensional architecture of the IFT complex B core. In recent years, methods to prepare samples with better homogeneity and higher stability for EM studies have been developed. Kastner and colleagues introduced the "GraFix" method that uses a sucrose gradient with simultaneous cross-linking to generate homogeneous particles for subsequent EM analyses (Kastner et al., 2008). Another method published recently presented a protocol for successful blotting of protein complexes from native PAGE onto the carbon grid (Knispel et al., 2012). Both approaches would be feasible for EM studies of the recombinant IFT complex B core by generating a more homogeneous sample for subsequent analyses.

7.4 Sub-core complex of IFT74 and IFT81 binds the chaperone protein Hsp70

Yeast-two hybrid assays have shown that IFT74 and IFT81 from *Chlamydomonas* directly interact with each other (Lucker et al., 2005). Both subunits from *T. brucei* together with the chaperone protein Hsp70 were analysed in this study. 6×His-tagged IFT81 was able to pull down both IFT74 and Hsp70. Due to the MBP-tag on Hsp70, the fusion protein was more expressed than IFT74 and IFT81 since MBP is known to improve both the solubility and the yield of a recombinant protein (Kapust and Waugh, 1999). On the size-exclusion chromatography, the majority of the three proteins were co-eluted with a 1:2:2 (Hsp70:IFT81:IFT74) stochiometry, i.e, one copy of Hsp70 binds to a tetramer of two copies each of IFT81 and IFT74 (Figure 11c). Given the stronger overexpression of MBP-Hsp70, it was not surprising that using amylose beads to capture MBP-Hsp70 resulted in an excess of MBP-Hsp70 over IFT81 and IFT74 (Figure 11b). No binding site of Hsp70 to either of IFT81 or IFT74 has yet been identified. Nevertheless, the binding seems to be not based on the chaperone function of the Hsp70, since including ATP- and high glycerol washes on the Ni-NTA affinity column did not result in an altered binding of Hsp70 to IFT74 and IFT81. Although the assembly seems to be stable to some extent, rotary shadowing experiments (data not shown) did not show a distinct structure of the complex proteins, which could be due to the mechanical stress during the grid preparation that disrupts the association between the three polypeptides.

7.5 Lipid binding of the IFT complex B

Part of the cargo destined for the cilium is transported in vesicles from the trans-Golgi network to the ciliary base. IFT20, a peripheral subunit of the IFT complex B, is thought to be one of the key players in this process. However, how the cargo is loaded on the IFT particle for the subsequent transport into the cilium is yet unknown (Figure 16).
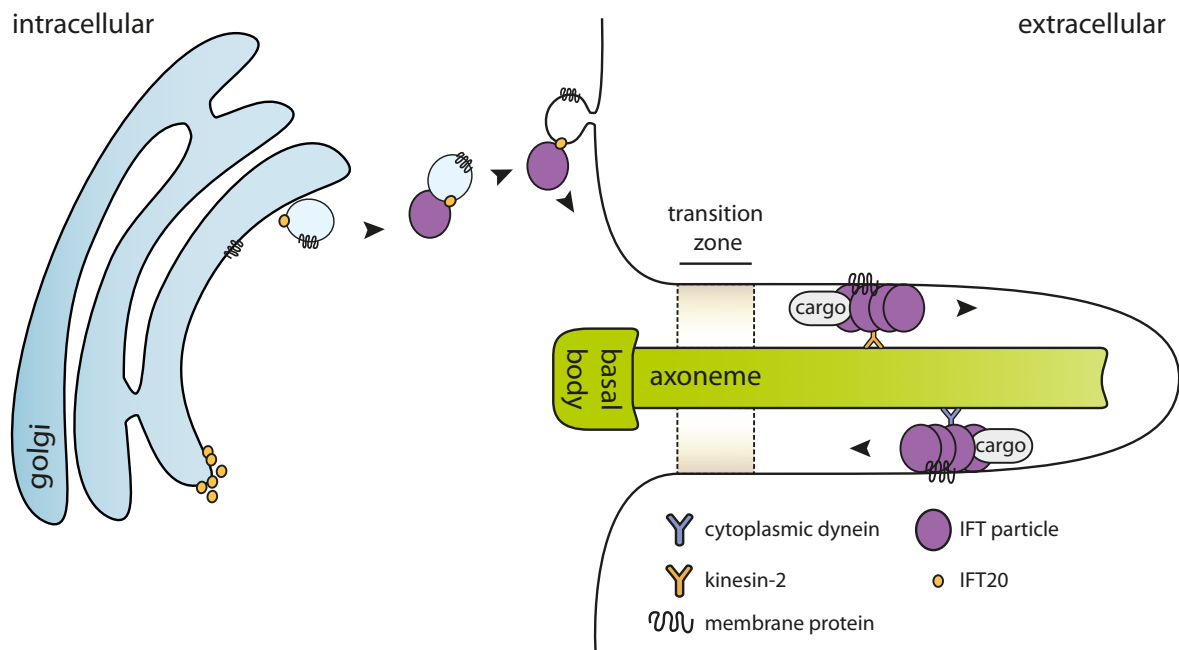
Figure 16 Vesicle trafficking from the Golgi to the cilium. IFT20 localises to the tans-Golgi network, where it interacts with GMAP210 (Follit et al., 2008). IFT20 is proposed to sort vesicles associated with molecules destined for the cilium; IFT20 is further involved with their correct transport to the ciliary base where they are fused to the plasma membrane to unload ciliary components (Follit et al., 2009).

In a preliminary experimental test, I have shown that the recombinant complex B core was able to bind to liposomes (Figure 12b, c). It is possible, that one or more of its subunits are the tethering points for vesicles. Given that the IFT74/81/Hsp70 complex could be pulled down by liposomes, at least IFT74 and/or IFT81 provide part of the lipid contact site. Whether other core-proteins might also attach to liposomes awaits further studies. Additionally, it should be investigated whether the types of lipids used to generate the liposomes have an influence on the binding of the IFT-B core.

7.6   IFT20 is in equilibrium between dimers and tetramers

IFT20 is a unique subunit of the IFT complex B since it is the only member also found to localise to the trans-Golgi network (Follit et al., 2006) (Figure 16). Previous studies have focused largely on the potential role of IFT20 in the transport of vesicles from the Golgi apparatus to their ciliary destination (Follit et al., 2006; Follit et al., 2008) and its involvement with ciliary disorders (Jonassen et al., 2008).

Despite the small size of the protein, no structural information has been published yet. Here I have shown that the recombinant protein could be easily purified in a bacterial expression system. The coiled-coil protein assembles into both a dimer and a tetramer. Whether this has any biological significance or is just a result of the used purification strategy is yet unknown. Interestingly, addition of CHAPS during the purification of the polypeptide resulted in less tetrameric IFT20 (Figure 15a). CHAPS is a zwitterionic detergent, normally used during the purification of membrane proteins (Raja and Vales, 2011). Adding the chemical in a concentration close to its critical micelle concentration (CMC) induced a partial shift of IFT20 to a dimer (Figure 14c, d). Moreover, IFT20 is in equilibrium between both states, as was observed upon re-loading the tetrameric or the dimeric protein, respectively, on a size-exclusion column (Figure 15b). These two states of IFT20 were probably the reason for the unsuccessful crystallisation attempts of the protein. As was observed with the IFT complex B core, a homogeneous sample is indispensable for successful crystallisation. In order to crystallise IFT20 it might be feasible to investigate co-crystallisation with binding partners, like IFT54 (Omori et al., 2008) or IFT57 (Baker et al., 2003). The interaction could stabilise the polypeptide in one of its oligomerisation states and may thus facilitate protein crystallisation.

Part II:

Structural characterisation of the coiled-coil domain of the cytolinker protein plectin

1   Abstract

Plectin is a versatile cytolinker protein, whose unique domain organization allows it to cross-link the three main cytoskeleton components, intermediate filaments, actin and microtubules. Plectin is of special importance in hemidesmosomes and the z-discs, where it acts as a stabilizer of the structure. A large set of mutations in plectin have been linked to the onset of the human disorder epidermolysis bullosa (EB). This disease manifests itself as a loss of skin integrity and occurrence of skin blisters. Most of the mutations have been identified as autosomal recessive with the exception of Ogna, a substitution of arginine to tryptophan in the coiled-coil domain of the protein. To investigate the influence of this single amino acid change on the functionality of plectin, I have carried out extensive biochemical, biophysical and structural studies on the recombinant coiled-coil domain plectin. The results indicated that the mutation mainly influences the oligomerization ability of plectin. Using electron paramagnetic resonance (EPR) study, the orientation of the coiled-coil protein was identified to be parallel and does not change upon introduction of the arginine to tryptophan mutation. Future studies will be needed to fully understand the influence of the single amino acid change on the integrity of plectin and the development of EB.

2   Zusammenfassung

Plectin ist ein vielseitiges Zytolinker Protein und besitzt eine ideale Struktur um alle drei wichtigen Zytoskelett-Komponenten – Actin, Mikrotubuli und Intermediäre Filamente - miteinander zu verbinden. Es ist von besonderer Bedeutung in den Hemidesmosomen der Epidermis und den Z-Linien in den Muskelzellen, wo es als Stabilisator fungiert. Verschiedene Mutation in Plectin konnten mittlerweile der Krankheit Epidermolysis bullosa (EB) zugeordnet werden. Diese Krankheit zeichnet sich durch eine besondere Sensitivität der Haut auf jeglichen mechanischen Stress aus, gekennzeichnet durch Blasen- und Wundbildung der Epidermis. Die meisten der Plectin Mutationen werden autosomal rezessiv vererbt, mit Ausnahme einer Mutation von Arginin zu Tryptophan (R>W). Diese Substitution liegt in der Coiled-coil Domäne des Proteins und ist bisher die einzige Mutation von Plectin mit einem dominanten Phänotyp. Um den Einfluß dieser einzelnen Aminosäurenänderung auf die Integrität und Stabilität von Plectin zu untersuchen, wurden verschiedene Abschnitte der Coiled-coil Domäne untersucht. Mittels Elektronenspinresonanz konnte festgestellt werden, dass das Protein ein paralleles Dimer ist, das sich unabhängig von der Mutation in dieser Orientierung bildet.   Interessanterweise scheint die Mutation R>W die Fähigkeit von Plectin zu beeinflussen größere Aggregate zu bilden. Inwiefern sich diese Beobachtung funktional mit der Entwicklung von EB korreliert, wird der Fokus zukünftiger Experimente sein.

3 Introduction

3.1 Plectin

As mentioned in the first part, one of the key architectural elements of the cilium is the microtubular axoneme (part I, chapter 3.2). Microtubules, together with the actin and the intermediate filaments, are the building blocks of the cytoskeleton, a complex network of protein fibers responsible for the cell's shape and required for processes like cell division, intracellular traffic or movement of cells along surfaces - just to name a few. The different properties of each of these three proteinaceous groups give rise to the various functions the cytoskeleton comprises. Actin filaments, with a diameter of around 6 nm, microtubules with 23 nm and intermediate filaments about 10 nm in width (Fuchs and Weber, 1994) are structurally stabilised and inter-linked by cytolinkers/accessory proteins. One versatile cytolinker family is the plakin family, with the main members being plectin (Figure 17, in green) and desmoplakin.
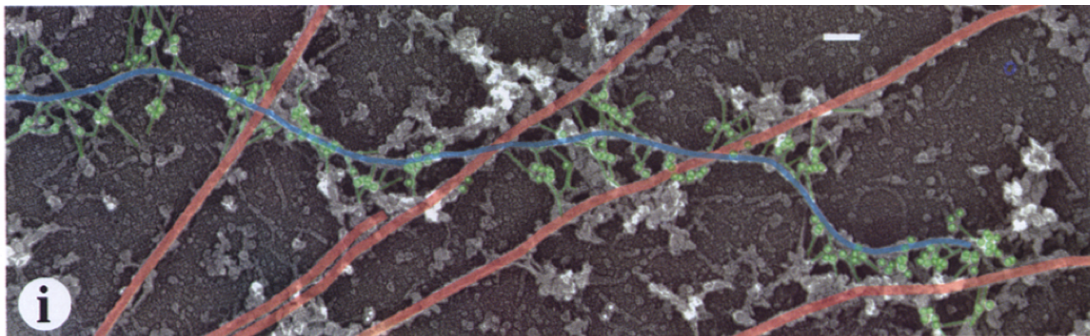
Figure 17 Linking the cytoskeleton by plectin. Plectin (green) cross-links intermediate filaments (blue) to microtubules (red). Scale bar: 0.1 μm. Figure from (Svitkina et al., 1996).

3.2 Domain organisation & structural information

Plectin is a large cytolinker protein (approx. 500kDa), which was identified as intermediate filament binding partner and reported to share structural homologies to microtubule-associated proteins (MAPs) decades ago (Pytela and Wiche, 1980). Structurally, plectin can be dissected into three regions. (1) an amino-terminal globular domain consisting of an actin-binding domain and several spectrin repeats

(plakin domain), (2) a central coiled-coil rod with a length of around 200 nm (Wiche, 1998), and (3) a carboxyl-terminal globular domain composed of 6 plectin repeats (Figure 18). EM analysis indicated that plectin has a dumbbell-like structure, as can be seen in Figure 17 in green, with the long coiled-coil rod enabling the linkage of distant binding partners (Steinböck and Wiche, 1999). Electron microscopy studies have clearly visualised plectin interacting with various cytoskeleton components (Svitkina et al., 1996), showing its versatility as a cytolinker.

Full length *Mm* Plectin domain organization
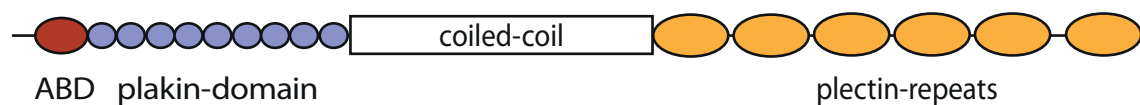
Figure 18 Domain organisation of full-length *Mus musculus* Plectin. The N-terminal globular domain contains binding sites for actin (red) and the spectrin repeats (blue). The C-terminal plectin repeats (yellow) include attachment sites for intermediate filaments.

Plectin is able to bind to actin via its N-terminal domain (Seifert et al., 1992), which regulates the actin network (Andrä et al., 1998) and serves to associate with integrin β4 (Rezniczek et al., 1998). The C-terminal region contains - aside from another integrin β4 site (Rezniczek et al., 1998) - the attachment site of intermediate filaments (Wiche et al., 1993). More precisely, a basic amino acid region between the 5th and the 6th plectin repeat is indispensable for the binding of plectin to intermediate filaments (Nikolic et al., 1996; Karashima et al., 2012). The interaction between these proteins has been the subject of diverse studies (Foisner et al., 1988; Hijikata et al., 1999; Favre et al., 2011), indicating a significant role of plectin in the architecture of intermediate filament structures (Wiche and Winter, 2011). Other binding partners of plectin include vimentin, desmin, fodrin and lamin B (reviewed in (Steinböck and Wiche, 1999)), just to name a few. The central coiled-coil domain is suggested to be involved in the oligomerisation of plectin. By itself, the coiled-coil domain is capable of forming dimers as well as higher oligomeric structures via lateral interaction along the coiled coil (Walko et al., 2011).

Interestingly, plectin exists as multiple isoforms generated by alternative splicing (Elliott et al., 1997). Analysing the exon-intron arrangement of human plectin revealed that 30 of the 32 exons are located in the N-terminal part of plectin (Liu et

al., 1996). Consequently, the different isoforms vary in short sequences in the amino-terminal domain with the remaining polypeptide being unchanged (Rezniczek et al., 2003; Wiche and Winter, 2011). This is one of the reasons for the wide range of various binding partners of plectin. Subsequently, tissue-dependent variations in the expression of plectin isoforms enable different cytoskeleton architectures in reliance on the cell's specific requirements. Interestingly, a rod-less splice variant of plectin has been detected in rat (Elliott et al., 1997) and human (Brown et al., 2001).

Plectin can be found in a variety of different tissues throughout mammalian species (Wiche, 1989). In the basal keratinocytes of the skin plectin is an essential component of hemidesmosomes (HD), a structure that attaches keratinocytes to the basement membrane zone (Tsuruta et al., 2011). Plectin is required for the connection of intermediate filaments with integrin (Borradori and Sonnenberg, 1999). Interestingly, in mouse keratinocytes isoform plectin 1a is selectively associated with HDs, while other isoforms are located at the cell periphery (Andrä et al., 2003). In the striated muscle cells plectin is situated at the z-discs (Wiche et al., 1983), the sarcomer boundaries and anchoring points for different filaments (Clark et al., 2002). Recent studies further indicate an association of plectin with proteins involved in signalling pathways (Lunter and Wiche, 2002; Osmanagic-Myers and Wiche, 2004; Gregor et al., 2006), implying a scaffolding role of plectin in these processes.

The large molecular weight of plectin has made it a challenging protein for structural studies. Hence, investigations have mainly focused on the analysis of fragments rather than the full-length protein. To date, crystal structures of plectin include parts of the plakin domain (Sonnenberg et al., 2007; Ortega et al., 2011) and the actin-binding domain (ABD) of mouse (Urbanikova et al., 2002; Sevcik et al., 2004) and human plectin (Garcia-Alvarez et al., 2003). Also, the ABD of human plectin binding to a fragment of integrin $\beta 4$ has been crystallised (de Pereda et al., 2009). However, no structural data is yet available for either the coiled-coil rod domain or the C-terminal globular domain.

3.3 Epidermolysis bullosa

Epidermolysis bullosa (EB) is a skin disorder characterised by blistering of the skin and mucus membranes (Shinkuma et al., 2011). Mutations in genes associated with the integrity of the dermal-epidermal basement membrane zone (BMZ) are connected to the onset of EB (Pfendner et al., 2005). In general, EB can be subdivided into three categories: EB simplex (EBS), junctional EB (JEB) and dystrophic EB (DEB) (Uitto and Richard, 2004).

Mutations in the plectin gene are linked to different forms of EBS, such as EBS with muscular dystrophy (EBS-MD) (Chavanas et al., 1996; Gache et al., 1996) and EBS with pyloric atresia (EBS-PA) (Pfendner and Uitto, 2005). Both EBS-MD and EBS-PA are autosomal recessive, like most of the plectin mutations related to EBS. Interestingly, most of the genetic modifications of plectin in EBS-MD result in truncated versions of the polypeptide (Pfendner et al., 2005).

A rare mutation of plectin results in an autosomal dominant form termed EBS-Ogna (Koss-Harnes et al., 2002; Walko et al., 2011). It is characterised by a change of cytosine (C) to thymine (T) in the central rod region at cDNA position 5998, leading to a substitution of arginine (R) for tryptophan (W) in the translated polypeptide (Koss-Harnes et al., 2002). Patients suffering from EBS-Ogna show the typical skin fragility but no muscular pathologies (Koss-Harnes et al., 2002), indicating that the mutation only influences plectin's function in the skin but not in muscle tissues. This is supported by data showing a reduced number of HDs in EBS-Ogna mouse and the degradation of plectin 1a (Walko et al., 2011). A current model proposed by Walko and colleagues (Walko et al., 2011) suggests that the R2000W mutation in human plectin introduces a local instability of the dimeric coiled-coil region, thus facilitating the proteolytic degradation of the protein.

4 Aim

The association of mutations in plectin with the disorder epidermolysis bullosa underlines the immense importance of the functionality of this cytolinker protein. The sub-group EBS-Ogna is characterised by a single amino acid change in the coiled-coil region of the protein. This change from arginine to tryptophan (R→W) has a drastic effect on the protein's function and its role in the hemidesmosomes of the skin. To unravel the influence of this amino acid change and how this could lead to the detrimental effects observed in patients suffering from EBS-Ogna, I will study the three-dimensional architecture of the coiled-coil domain of *M. musculus* plectin. More precisely, since the full-length construct is too large to be likely to crystallise, I will investigate the structure of smaller parts of the coiled-coil rod containing the mutation. The wild-type variant as well as the R→W mutated protein will both be studied by protein crystallography. Biochemical studies on the behaviour of the recombinant polypeptide will further give a more complete picture of the influence of the mutation on the functionality of plectin.

5 Materials and Methods

5.1 Cloning

General cloning procedures were performed as previously described (part I, chapter 5.1), unless otherwise stated.

All wild-type and R1999W (Ogna) plectin 1c rod-constructs in pET15b were obtained from Karin Gross (Wiche lab, MFPL, Vienna). Exceptions are the mini-rod constructs (wt & Ogna), all mutations listed in Table 4, and the pET29a and MalpET constructs. All constructs are summarised in Table 4. The constructs for insect cell expression are listed in Table 5 and were cloned and expressed by Karin Gross and Irmgard Fischer (Wiche lab, MFPL, Vienna).

The construct Glob-FL-rod (Table 5) contains the last helix of the 5th spectrin repeat and the four spectrin repeats (spectrin repeat 6-9) preceding the coiled-coil domain.

Single amino acid mutations were introduced using the Pfu-Ultra polymerase (Quick change mutagenesis, Stratagene) or Phusion polymerase (New England Biolabs). Primers were designed according to the Quick-change mutagenesis protocol (Stratagene). To ensure successful amplification of the desired mutation, 18 cycles were run. Afterwards, supercoiled template was digested by DpnI for 2 hours at 37°C prior to transformation into *E. coli* DH5α. The correct mutation was verified via sequencing.

Table 4 Constructs for bacterial expression.

	Name	AA range	Mutation	Vector	Affinity tag
Plectin	Full-length rod	1376-2501	K2043C$^\$$	pET15b/Amp^R	6xHis
	N-rod	1375-1806		pET15b/Amp^R	6xHis
				pET29a/Kan^R	no tag
	C-rod	2193-2501	E2367C$^\$$	pET15b/Amp^R	6xHis
	M-rod	1808-2189	K1883C$^\$$ K2043C$^\$$ E2149C$^\$$	pET15b/Amp^R	6xHis
	mini-rod	1975-2081	V2032M$^\#$ L2040M$^\#$ K2043C$^\$$ L2050M$^\#$ S2058M$^\#$	pET15b/Amp^R	6xHis
			-	MalpET/Kan^R	MBP
Ogna	Full-length rod	1376-2501	K2043C$^\$$	pET15b/Amp^R	6xHis
	N-rod	1375-1806		pET15b/Amp^R	6xHis;
				pET29a/Kan^R	no tag
	C-rod	2193-2501	E2367C$^\$$	pET15b/Amp^R	6xHis
	M-rod	1808-2189	K1883C$^\$$ K2043C$^\$$ E2149C$^\$$	pET15b/Amp^R	6xHis
	mini-rod	1975-2081	V2032M$^\#$ L2040M$^\#$ K2043C$^\$$ L2050M$^\#$ S2058M$^\#$	pET15b/Amp^R	6xHis
			-	MalpET/Kan^R	MBP

$^\$$ Mutations for EPR measurement

$^\#$ Mutations for phasing in crystal structure determination

Table 5 Constructs for baculovirus/insect cell expression

	Name	AA range	Mutation	Affinity tag
Plectin	Full-length rod	1376-2501	K2043C$^\$$	6xHis
	Glob-FL-rod$^\%$	898-2501		6xHis;
Ogna	Full-length rod	1376-2501	K2043C$^\$$	6xHis
	Glob-FL-rod$^\%$	898-2501		6xHis;

$^\$$ Mutations for EPR measurement

$^\%$ These constructs contain the four preceding globular spectrin repeats

5.2 Expression & Purification

E. coli strain BL21 (DE3) was used for the expression of recombinant proteins. All expressions were carried out at low temperature (16° to 18° Celsius) to increase the amount of soluble proteins. For a detailed description see part I, chapter 5.2.

Pelleted cells were resuspended in lysis buffer (20 mM Tris-HCl, pH 8.0, 300 mM NaCl, 5% glycerol, 20 mM imidazole, 1 mM PMSF, 2 µg/ml DNAse I) and broken using the Emulsiflex-C3 Homogenizer (Avestin). Cell lysate was cleared as described in part I, chapter 5.2. Nickel-affinity chromatography was taken as the first purification step, using a gravity column or a HiTrap chelating HP column (GE healthcare) on a Äkta purifier (GE healthcare). Bound proteins were eluted via an increasing imidazole gradient. If the protein was used for crystallographic studies, the N-terminal 6×His tag was removed via thrombin digestion (20% of total protein amount) overnight at 4°C. The affinity-purified protein was concentrated using Amicon ultra centrifugal filters (MWCO: 3 - 50kDa) and subsequently loaded on a size exclusion chromatography column Superdex-200, 16/60 or the analytical Superose 6 10/300 (HiLoad; GE healthcare), which was pre-equilibrated with SEC-buffer 1 (20 mM Tris-HCl, pH 8.0, 100 mM NaCl, 5% glycerol) or SEC-buffer 2 (20 mM HEPES, pH 7.5, 100 mM NaCl, 5% glycerol). In general SEC-buffer 1 was used. SEC-buffer 2 was used only if subsequent biochemical analysis was incompatible with a Tris-HCl-based buffer.

5.2.1 Purification of protein produced in insect cells

Insect cell pellets containing the constructs listed in Table 5 were obtained from Wiche's lab (MFPL, Vienna). The pellets were lysed in buffer A (20 mM HEPES, pH 7.4, 1% glycerol, 1% Triton X-100) prior to centrifugation at 16.000 rcf for 30 minutes at 4°C. The supernatant was diluted 6 times with HiTrap buffer (50 mM sodium phosphate pH 7.4, 300 mM NaCl) and loaded on a 1-ml HiTrap chelating HP column (GE Healthcare) charged with Co^{2+}. The bound protein was eluted via a linear imidazole gradient. The protein was either directly used for rotary metal shadowing experiments or dialysed against HiTrap buffer to remove the imidazole.

5.3   Selenomethionine labelling

To express selenomethionine-labelled protein, the methionine auxotrophe strain *E. coli* B834 was used (gift from the Clausen lab, IMP, Vienna). Cells from 10 ml of overnight cultures were pelleted and resuspended in 1L of minimal media (60 mM K_2HPO_4, 33 mM KH_2PO_4, 7.5 mM $(NH_4)_2SO_4$ and 1.7 mM Tri-Sodium Citrate), supplemented with 1 mM $MgSO_4$, 0.00048% Thiamine, 40 µg/ml amino acid mix 1 (Table 6), 40 µg/ml amino acid mix 2 (Table 6), 40 µg/ml selenomethionine and 0.2% glucose. When OD_{600} reached 0.5-0.6 at 37°C, cells were immediately chilled on ice for 10 minutes and transferred to 18°C. 30-45 minutes after this transfer, the protein expression was induced by 0.5 mM IPTG. Cells were harvested 18-20 hours post induction. Selenomethionine-labelled protein was purified in the presence of either 10 mM β-mercaptoethanol (for affinity purification) or 5 mM DTT (for size-exclusion chromatography) in all buffers.

Table 6 Composition of the amino acid mixes.

Amino acid mix	Ingredients
1	all L-amino acids except methionine, tyrosine, tryptophan and phenylalanine dissolved in sterile water stock concentration: 40 mg/ml
2	tyrosine, tryptophan and phenylalanine, dissolved in sterile water, small amount of hydrochloric acid was added to improve solubility stock concentration: 40 mg/ml

5.4   Lysine methylation

Lysine methylation as described by Walter and colleagues (Walter et al., 2006) was used to improve the crystallisation. In short, following procedure was used, all steps carried out at 4°C.

Affinity purified protein was desalted into methylation buffer (50 mM HEPES pH 7.5, 250 mM NaCl) via a HiPrep 26/10 desalting column (GE Healthcare) and diluted to a concentration of less than 1 mg/ml. For each millilitre of protein solution, 20 µl of 1M dimethyl-borane complex (DMBC, Sigma; dissolved in ddH20) and 40 µl of 1M formaldehyde (Merck) were added and stirred at 4°C for two hours, followed by another addition of 20 µl 1M DMBC and 40 µl 1M formaldehyde. After incubation for two more hours, a final amount of 10 µl 1M DMBC was added. The protein solution was continuously stirred at 4° over night. On the next day precipitated protein was removed by centrifugation, followed by size-exclusion chromatography using SEC buffer 1. Methylated protein was concentrated to a final concentration of 5-20 mg/ml and utilised for crystallisation trials.

5.5   Static light scattering

All static light scattering (SLS) experiments were carried out on an instrument from Wyatt Technology Corp. The system consists of a HPLC system (Agilent Technologies) that is connected in sequence to a triple-angle laser light scattering detector (miniDAWN TREOS), a UV detector (280nm, Agilent Technologies) and a refractive index detector (RI-101, Shodex). 100 µg of the respective protein was loaded on a Superose 6 10/300 column (GE healthcare) or Superdex 200 10/300 (GE healthcare) pre-equilibrated with SLS buffer (20 mM Tris-HCl pH 8.0, 100 mM NaCl) and eluted at a constant flow rate of 0.5 ml/min. The collected data was analysed with the Astra software (Wyatt technology).

5.6 Chemical cross-linking

Glutaraldehyde cross-linking was performed as described in part I, chapter 5.3. Alternatively, dimethyl-pipelimidate (DMP, Sigma) was used for chemical cross-linking. DMP has an arm-length of 9.2 Å. Prior to cross-linking, the protein was transferred into cross-linking buffer 1 (20 mM HEPES, pH 7.5, 100 mM NaCl, 5% glycerol) or cross-linking buffer 2 (50 mM Bicine, pH 8.5, 27.5 mM NaCl, 26 mM KCl) either by size-exclusion chromatography or micro-Biospin columns P-6 (Biorad) and diluted to 0.5-1 mg/ml.

DMP was mixed with the protein of interest at a final concentration of 20 mM DMP and allowed to react for 30-40 minutes at room temperature. The reaction was stopped by the addition of 100 mM Tris-HCl (pH 8.0). The cross-linking results were analysed by SDS-page.

5.7 Electron microscopy

All electron microscopy experiments were carried out with the help of Ekaterina Shimanovskaya (negative staining and image acquisition) or Marlene Brandstetter (rotary metal shadowing and image acquisition).

For all negative staining experiments, protein at a concentration of approximately 60 µg/ml was adsorbed to glow-discharged grids and stained for 1 minute using 2% uranyl acetate with unadjusted pH.

For rotary metal shadowing, protein at a concentration of approximately 25 µg/ml in buffer containing 20% glycerol (v/v) was prepared. The samples were rotary shadowed with 0.7 nm platinum/carbon at an angle of 5 degree.

Image acquisition was done on a Morgagni 268D electron microscope (FEI) at 80 kV. Image analysis was done using ImageJ (http://rsbweb.nih.gov/ij/).

5.8 Electron Paramagnetic Resonance Studies

To determine the coiled-coil orientation, electron paramagnetic resonance (EPR) spectroscopy of site-directed spin labelled constructs was carried out. This method enables to study the conformation of a target protein by introducing a paramagnetic spin label into the macromolecule. The spin label is attached to accessible cystein residues in the protein and subsequent spectroscopic measurements can yield information about the distance of other paramagnetic labels in the protein within a distance of 1-8 nm (Steinhoff, 2002). The orientation of coiled-coil systems can be determined by either pulsed EPR measurements for distances in the range of 2-8 nm or low-temperature continuous wave (cw)-EPR measurements for short distances (below 2 nm). All EPR measurements as well as subsequent data analyses were carried out under supervision of Dr. Katharina Pirker (AIT Tulln).

To attach the paramagnetic spin label the following procedure was used:

Purified protein in SEC buffer 1 (20 mM Tris-HCl pH 8.0, 100 mM NaCl, 5% glycerol) or affinity chromatography buffer (20 mM Tris-HCl pH 8.0, 300 mM NaCl, 5% glycerol, 250-400mM imidazole) was incubated with the spin label (1-Oxyl-2,2,5,5-tetramethyl-Δ3-pyrroline-3-methyl) Methanethiosulfonate (MTSSL, *Toronto Research*) at a ratio of 1:8 or 1:20 (protein : MTSSL) and kept rotating at 4°C in the dark over night. Excess of unbound spin label was removed using a PD-10 desalting column (GE healthcare) followed by size-exclusion chromatography (Superdex 200 16/60, GE healthcare). The labelled protein was concentrated to at least 50 μM for subsequent measurements.

Initial cw-EPR spectra were collected at UFT Tulln on a Bruker EMX spectrometer operating at 9.4 GHz equipped with a high sensitivity resonator. Low temperature measurements were carried out using a variable temperature unit cooled with liquid nitrogen. All room temperature measurements were carried out with 1 mW microwave power, 100 kHz modulation frequency, 0.1 mT modulation amplitude and 41 ms conversion time and time constant. Parameters for 160 K measurements were chosen with 0.2 mW microwave power, 100 kHz modulation frequency, 0.25 mT modulation amplitude and 41 ms conversion time and time constant.

Samples with spin label efficiency of higher than 60% were taken for double electron-electron resonance (DEER) measurements at Bruker BioSpin Headquarters (Rheinstetten, Germany). DEER experiments were performed at 60 K on a Bruker ELEXSYS spectrometer operating at 9 GHz. The four-pulse DEER sequence was chosen with $\pi/2(\nu_{obs})$-τ_1-$\pi(\nu_{obs})$-t'- $\pi(\nu_{pump})$-$(\tau_1+\tau_2$-t')-$\pi(\nu_{obs})$-τ_2-echo, where the observer pulse length was 12 ns for $\pi/2$ and 24 ns for π pulses. The pump pulse length was 12 ns, the long interpulse delay was $\tau2$ = 1200, 2000 or 3000 ns. All other parameters were used according to (Pannier et al., 2000). The DEER spectra were analysed using the programme DeerAnalysis2010 (Jeschke, 2006). The background was corrected by a homology 3-dimensional fit. Simulations were checked for stability according to the DEERAnalysis2010 manual.

To determine distances shorter than 2 nm, low-temperature cw-EPR was used. A spin dilution experiment as described in Gross et al (Gross et al., 1999) was carried out in order to prepare control samples for the parallel as well as anti-parallel coiled-coil constructs. In the control, only one fifth of every spin label site is occupied by the paramagnetic label, whereas the other ones sites carry a diamagnetic analogue. A 1:4 mixture of MTSSL and a diamagnetic analogue (1-Acetyl-2,2,5,5-tetramethyl-Δ3-pyrroline-3-methyl Methane-thiosulfonate (MTS), *Toronto Research*) was prepared and added with an 8 times molar excess to the affinity purified protein. Following overnight incubation at 4°C, excess spin label was removed as described above for the regular labelled samples. Spectra were collected at 160 K. Analysis of the spectra broadening and computation of the short distance were done with the programme WinDipfit (Steinhoff et al., 1997).

5.9 Crystallisation & data collection

Initial protein crystallisation trials were pipetted using a Phoenix/RE robot (Art Robot Industries) for sitting drop vapour diffusion. Either Intelli-3-well plates (Art Robot Industries) or MSC-2-well plates (Swissci) were used in combination with different commercially available screens (Table 7) to identify suitable crystallisation conditions. Plates were stored at either 22°C or 4°C in a crystallisation hotel CrystalMation (Rigaku).

Table 7 Commercial crystallisation screens tested.

| Company	Screen
Hampton Research	Crystal screen I & II
	Cryo 1-2
	PEG/ion
	Additive screen
	Detergent screen
Emerald Bioscience	Wizard I & II
Molecular Dimension	Morpheus
	Midas
	PACT premier
Jena Bioscience	JBS 1-4

Initial crystallisation hits were manually optimised by using hanging drop vapour diffusion in 48-well plates (VDX48, Hampton Research). Optimised crystals were tested in-house on an X8 PROTEUM (BrukerAXS). To avoid damage during freezing, crystals were equilibrated in cryo-protectant solution prior to freezing in liquid nitrogen. Cryo-protection was achieved by adding either 20% glycerol or 40% PEG400 to the given crystallisation condition.

For improvement of diffraction data, crystal dehydration technique (Heras et al., 2003) was applied. Following two approaches were tested. Crystals were transferred to 3 µl of cryo-protectant solution (crystallisation solution + cryoprotectant) and equilibrated overnight against 400 µl of dehydration solution (crystallisation solution + 40% PEG 400). Alternatively, crystals were moved to 15 µl dehydration solution and equilibrated against air for approximately 2 hours, prior to freezing in liquid nitrogen.

Crystal diffraction data was collected at the European Synchotron Radiation Facility (ESRF) in Grenoble, France. The native crystal dataset was collected at ID23-1 and the selenomethionine crystals at the tuneable beamline ID14-4. The collected diffraction data were integrated using iMosflm (Battye et al., 2011) and scaled using the SCALA software (Evans, 2006). Autosol, part of the software suite Phenix (Terwilliger et al., 2009), was used to locate the selenium sites and to calculate the experimental maps. The model was built in COOT (Emsley and Cowtan, 2004) and refinement was done using CNS (Brunger et al., 1998).

6   Results

EBS-Ogna is caused by a single amino acid replacement at position 2000 (R2000W) in human and position 1999 (R1999W) in mouse plectin. It represents a unique plectin mutant that results in this rare autosomal dominant disorder. To investigate the structural basis of this mutant, a number of constructs of the coiled-coil domain of mouse plectin 1c (Refseq NM_011117.2) have been generated for crystallographic and biochemical studies (Figure 19). The three constructs spanning residues 1376-2501 (full-length), 1808-2189 (M-rod) and 1975-2081 (mini-rod), which all contain the mutation position, have been cloned both as wild-type (wt) and as mutant (R1999W; Ogna) form.
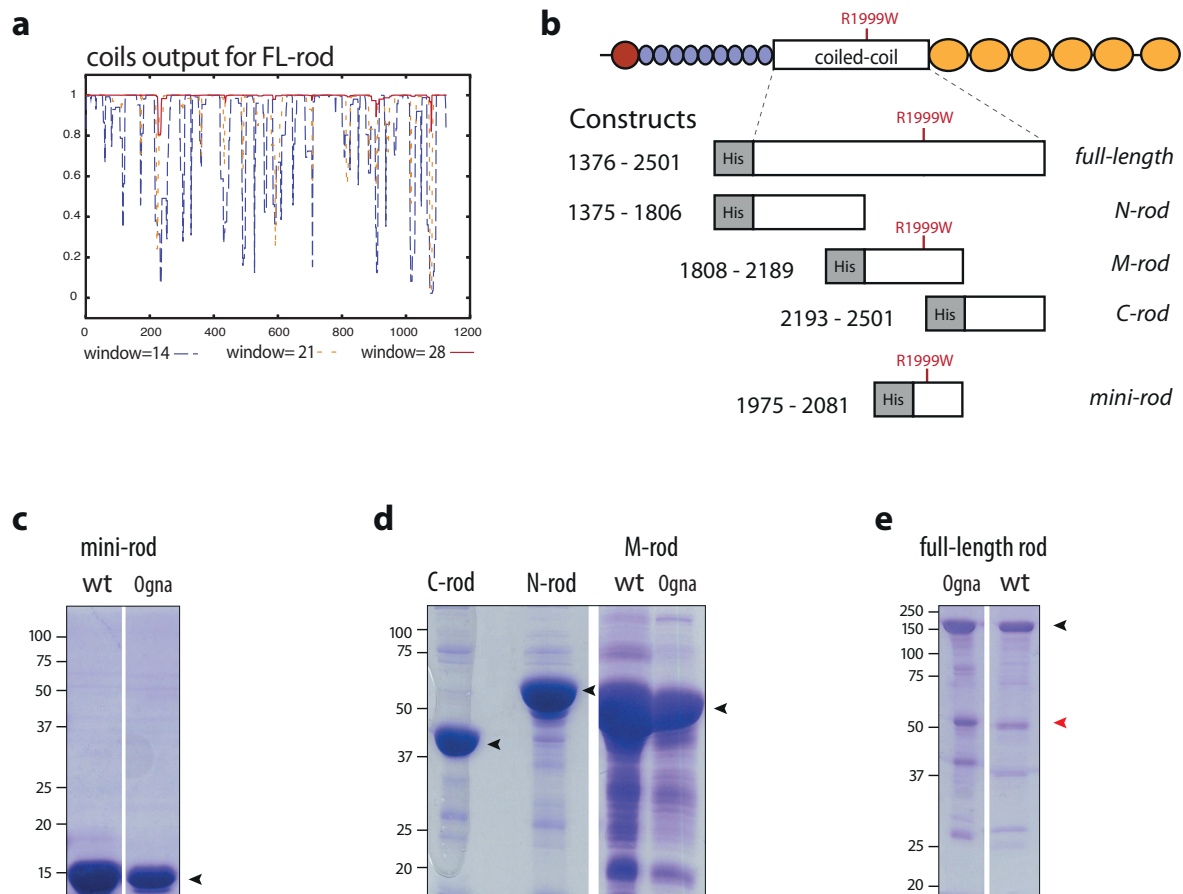

Figure 19 Constructs and expression of the plectin coiled-coil rod. (a) Full-length (FL) coiled coil of plectin was analysed by the COILS server. (b) A schematic representation of several generated constructs. The mutation R1999W is indicated relative to its position in the given construct. Simplified names of the constructs are given in italic. (c-e) Purification of different truncations of recombinant plectin after overexpression in *E. coli*. The black arrows mark the proteins of interest; the red arrow marks degraded proteins.

The full-length coiled-coil construct (residues 1376-2501), which has a theoretical molecular weight of 130 kDa, showed on an SDS-PAGE a band of ~150 kDa (Figure 19e, black arrow). Aside from the aberrant migration behaviour during electrophoresis, part of the protein degraded readily into a stable 50 kDa fragment (Figure 19e, red arrow). The N-terminal 6×His tag was removed via thrombin digestion. SDS-Page analysis revealed that the 50-kDa degradation product was also digested by thrombin (data not shown), indicating that it is a degraded product from the C-terminus of the full-length rod. Other generated coiled-coil constructs could be purified with only minor impurities and were used for structural studies (Figure 19c, d; black arrows indicate the protein of interest).

6.1 Oligomerisation state of the plectin coiled-coil rod

Because of the aberrant elution behaviour due to the elongated shape, size-exclusion chromatography is not suitable for the determination of the molecular weight/oligomerisation of a coiled-coil protein. Static light scattering (SLS) is an alternative approach that is able to measure the molecular weight of a molecule independent of its shape. Thus, SLS was used to examine the oligomerisation state of the recombinant plectin coiled-coil rod in addition to chemical cross-linking experiments. All of the generated constructs (Figure 19b) were used for this study. The recombinant proteins were purified by Ni-NTA affinity chromatography and subsequently used for SLS measurements. It has been shown previously that the full-length rod expressed in insect cells forms both dimers and higher oligomers in solution (Walko et al., 2011).

SLS results indicated that the full-length rod produced in bacteria has a molecular weight of 150 kDa for both wt and Ogna (Figure 20a). This is only slightly larger than the theoretical weight of 130 kDa of the monomer protein, indicating that this construct is a monomer. Aside from the monomeric peak, two lower molecular weight peaks were detected (Figure 20a). They most likely contain degradation products of the full-length rod, since the protein is not stable in solution (Figure 19e, red arrow).
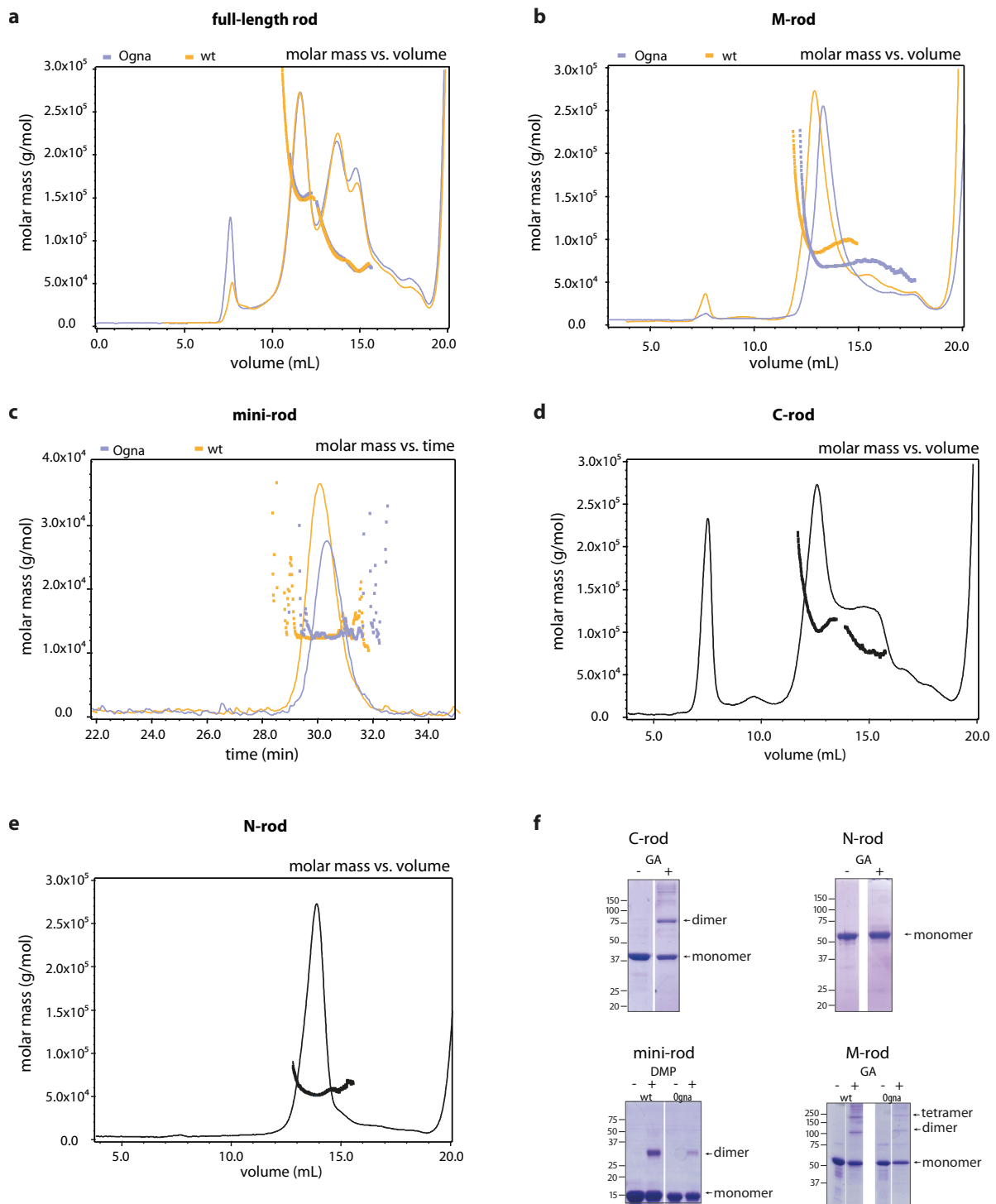
**Figure 20 Static light scattering (SLS) analyses of different truncations of the plectin rod domain.**
(a) Full-length rod was calculated to be ~150 kDa in solution, corresponding to a monomer. (b) The molecular weight of the M-rod slightly differed between wild-type and Ogna. (c) The mini-rod of plectin showed a molecular weight of 13kDa, corresponding to a monomer. (d) SLS showed that the C-terminal rod forms a trimer and a dimer. An aggregation peak is eluting at 8ml. (e) Plectin N-rod was calculated to be a monomer. (f) Cross-linking results of different truncations. 0.01% glutaraldehyde was used to cross-link plectin N-rod and C-rod for 5 minutes and plectin M-rod (wt/Ogna) for 10 minutes at room temperature. DMP was used to cross-link both wild-type and Ogna mini-rod.

SLS results also indicated that the M-rod has a molecular weight of approximately 90 kDa for wild-type plectin, suggesting a dimeric form. Interestingly, however, the Ogna mutant of the same segment was measured to be about 70 kDa (Figure 20b). This does not match either the monomeric form (45 kDa) or the dimeric form (90 kDa). A possible explanation is that there is an intermediate state between monomer and dimer and the averaging algorithm of the program is not able to reflect such a state. Using glutaraldehyde to cross-link the species present in wild-type and Ogna plectin M-rod, bands corresponding to both a dimer and a tetramer were observed (Figure 20f).

The two mini-rod constructs (residues 1975-2081) were also analysed by SLS. Surprisingly, the molecular weight for both wild-type and the Ogna mutation was measured to be 12-13 kDa, a clear monomer (Figure 20c), while chemical cross-linking using dimethyl pipelimidate (DMP) showed dimerised protein bands (Figure 20f).

Analysing the C-rod by chemical cross-linking showed that the protein is predominantly a dimer in solution (Figure 20f). By SLS, the construct was found to be a dimer; additionally a peak corresponding to a trimer could also be observed (Figure 20d). Interestingly, the N-terminal region of the rod was found to be a monomer both by SLS and glutaraldehyde cross-linking (Figure 20e, f).

To test whether the N-rod and C-rod are able to interact – as they would in an anti-parallel coiled-coil conformation – both purified proteins were mixed and loaded on a Superdex 200 10/300 (Figure 21a). For comparison, the individual constructs were also loaded on the same size-exclusion column (Figure 21b, c). Plectin N- rod alone eluted around ~12.8 ml (Figure 21b); the C-terminal rod eluted both at the void volume and at 11.6-13 ml (Figure 21a, c). The size-exclusion chromatogram of the mixed N- and C-rod showed plectin N-rod to still elute at approximately 12.7 ml, and plectin C-rod to elute in the same range as in the individual run (Figure 21a). No higher molecular weight peak corresponding to a complex between N- and C- rod was observed.
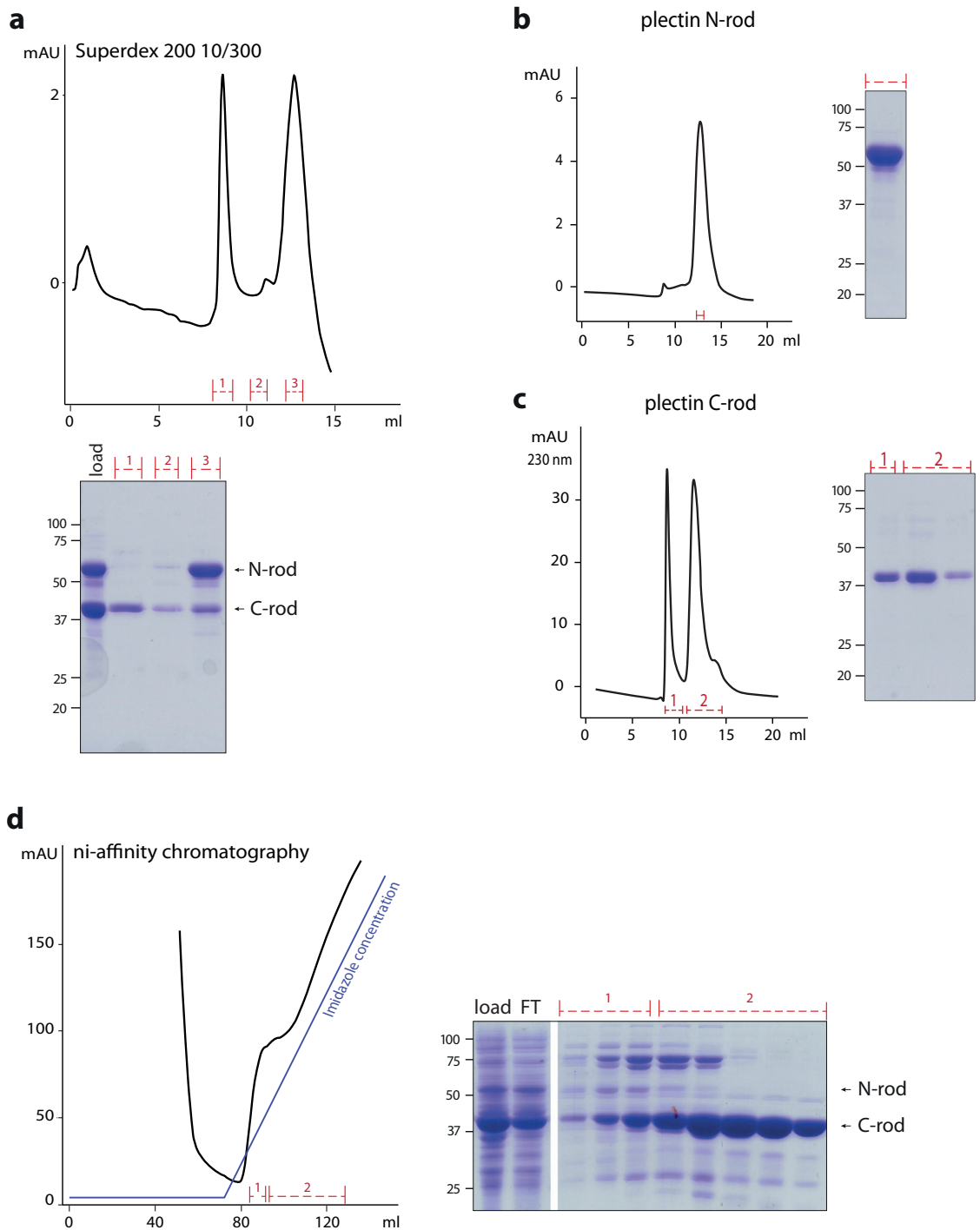
Figure 21 Interaction test of the N- and C-termini of the plectin coiled coil. (a) The purified N- and C-terminal part of the coiled-coil rod were mixed in an equimolar ratio and loaded on an analytical Superdex 200 10/300 column. (b, c) The individual constructs were loaded on the same column for comparison. (b) Plectin N-rod eluted at ~12.8 ml. (c) The C-rod construct eluted at the void volume and between 11.6-13 ml. This fragment does not contain any tryptophan, thus the UV at 230 nm was measured. (d) Affinity purification of the co-expressed plectin untagged N-rod and 6×His-tagged C-rod. FT, flowthrough.

Furthermore, 6×His-tagged plectin C-rod was unable to capture untagged plectin N-rod in significant amounts upon co-expression (Figure 21d).

These results suggest that the N- and C-terminal part of the coiled coil do not interact, thus it is likely the plectin coiled coil has a parallel arrangement in a dimeric form.

6.2 Influence of the R1999W mutation on the oligomerisation of the full-length rod

During affinity purification and SLS measurements, no significant differences between wild-type and Ogna plectin were observed. To investigate how this mutation may influence the integrity of the protein, I used analytical size-exclusion chromatography to study differences in the oligomerisation ability of the full-length plectin rod in both wild-type and Ogna forms. Since the UV signal did not correspond to the amount of protein loaded on the SDS-PAGE, the band intensities on the SDS-PAGE were analysed using ImageJ (*http://rsbweb.nih.gov/ij/*) to plot against the fraction number (Figure 22).

Comparison of both plectin and Ogna full-length rod showed that they peaked at different elution volumes (Figure 22c). While wt plectin tended to form oligomers to a large extent, the mutant counterpart existed almost equally as oligomers and dimers. Therefore, the mutation seems to impair the protein's ability to form larger oligomers. One possibility is that the residue R1999 contributes to the oligomeric association of the rod domain; substituting it by the bulky and hydrophobic aromatic tryptophan (W) might weaken this association. The same analysis of the wild-type and the Ogna mutant of the M-rod indicated a similar pattern (data not shown).
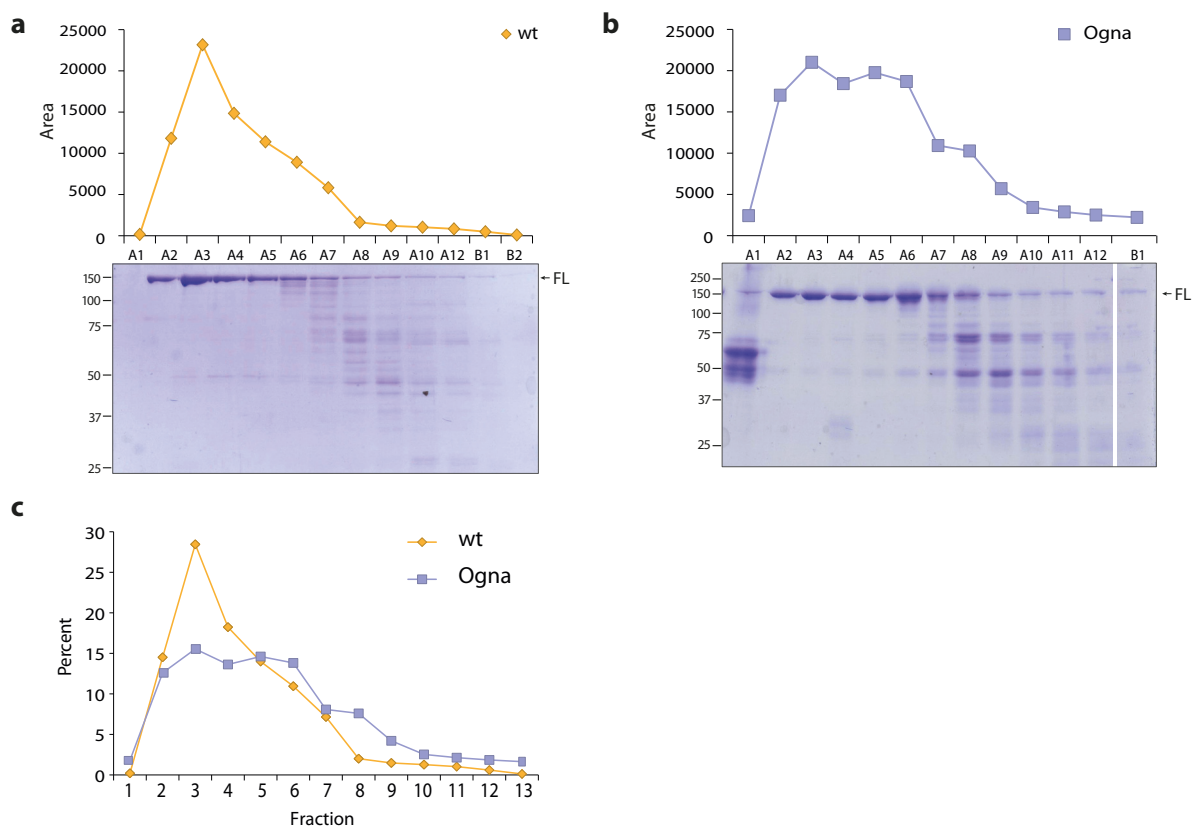
Figure 22 Analytical gel-filtration analyses of wt and the Ogna mutant of the plectin rod domain. Full-length rod samples pre-purified by Ni-NTA were loaded on the Superose 6 (10/300) column. 1 ml each for fractions from the void volume (fraction 'A1') onwards were collected and analysed on an SDS-PAGE. Band intensities were computed using ImageJ. (a) Elution profile of the wild-type plectin rod domain. (b) Elution profile of the Ogna mutant of the plectin rod domain. (c) The curves of both wild-type and mutated plectin were overlaid for comparison.

6.3   Crystallisation of Ogna mini-rod

The shortest construct Ogna mini-rod was successfully crystallised in 0.1 M sodium/potassium phosphate pH 6.2, and 2-2.5 M sodium chloride.

A native dataset was initially collected to 2.5 Å resolution, but spots with rotational disorder were observed (Figure 23a). To solve the phase problem, single wavelength anomalous dispersion (SAD) was utilised, using selenomethionine labelled protein. Initial attempts to solve the phase were not successful because the selenomethionine sites could not be found. This was later explained by the observation that the first 12 residues containing the selenomethionine labelled residues are disordered in the final

structure (Figure 23c). Therefore, we have generated the following mutations in the central region of the protein: V2032M, L2040M, L2050M and S2058M (Figure 23c). Each single mutant was expressed and used for crystallisation.
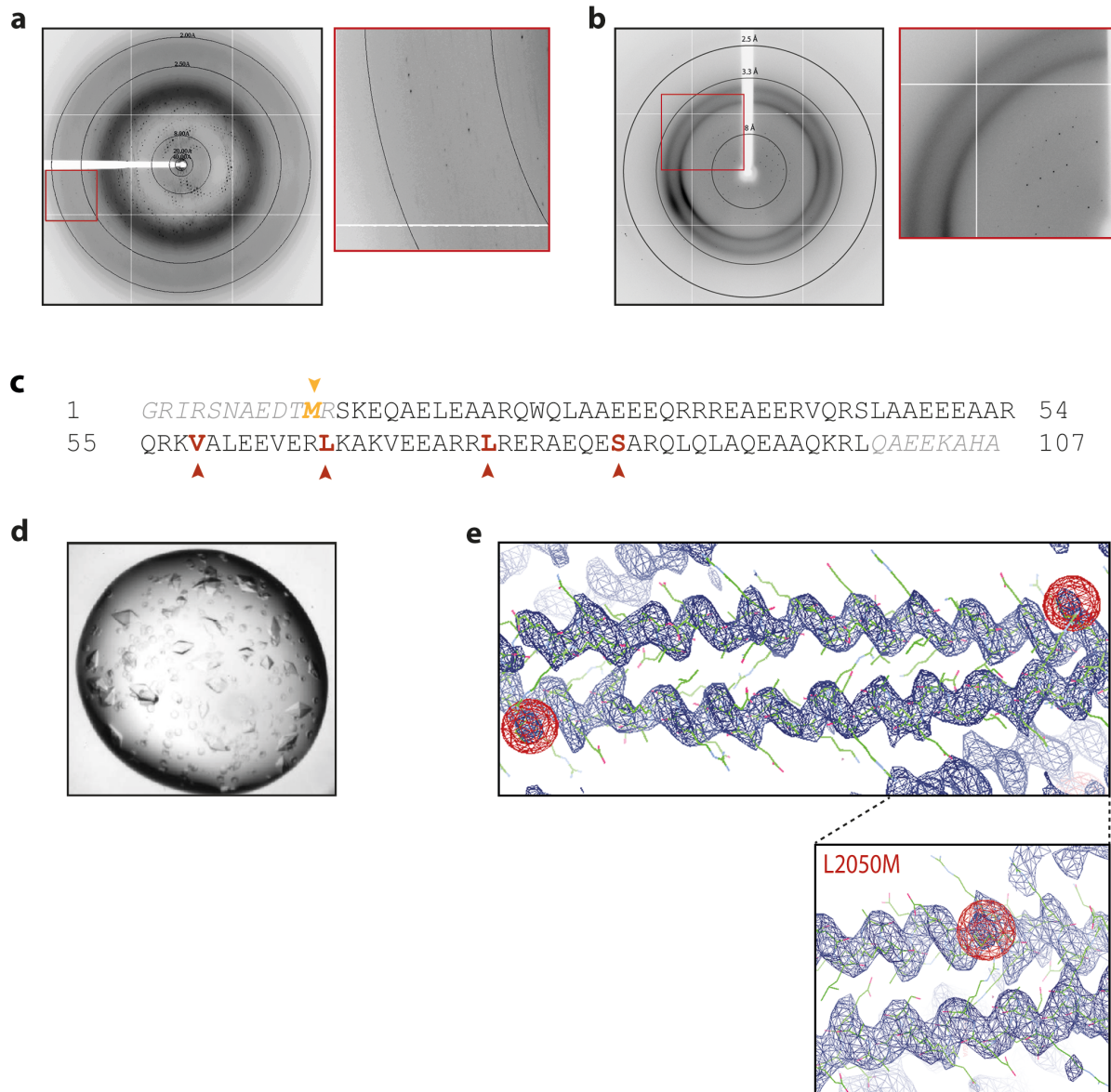

Figure 23 Crystallisation and structure determination of the Ogna mini-rod. (a) Diffraction pattern of the native crystal. The red square shows an amplification of an area for a better view of the smearing spots. (b) Diffraction pattern of the crystals after lysine methylation. The red square shows the discrete spots without rotational disorder. (c) Amino acid sequence of the Ogna mini-rod. In italic grey are the residues that are missing in the final structure. The yellow methionine is the only native methionine in the mini-rod construct. It could not be detected in the initial SAD phasing due to the disordered N-terminal 12 residues in the final structure. The red arrows mark the residues that were mutated to methionine for phase determination. (d) Crystals of the L2050M mutant. (e) The experimental electron density map of the anti-parallel Ogna mini-rod. In red are the two selenomethionine groups in the dimer.

94

No crystals were obtained for S2058M, whereas V2032M only produced small crystals. L2040M and L2050M both crystallised in sodium/potassium phosphate pH 6.0, 5 mM DTT and 2.5 M sodium chloride (Figure 23d). Both selenomethionine constructs diffracted well and data collected from Ogna L2050M was used for SAD-phasing. However, although it was possible to solve the phase problem this time and an anti-parallel coiled coil could be built (Figure 23e), the model could not be refined to a satisfactory statistics (R_{work} ~40%). This was later found to be due to the observed rotational disorder of the native dataset (Figure 23a), which left significant residual electron densities around the two continuous helices unassigned.

Table 8 Data collection and refinement statistics.

Data collection	
Space group	I422
Cell dimensions	
a, b, c (Å)	105.59, 105.59, 90.40
Resolution (Å)	35-3.5 (3.83-3.50) *
No. unique reflections	31475 (3397)
R_{sym}	0.212(0.883)
I / sI	8.7 (3.5)
Completeness (%)	99.9 (100.0)
Redundancy	9.3 (9.7)
Refinement	
Resolution (Å)	35-3.5
R_{work} / R_{free} (%)	27.2/30.2
No. atoms	
Protein	720
R.m.s. deviations	
Bond lengths (Å)	0.0106
Bond angles (°)	1.33

*Values in parentheses are for highest-resolution shell.
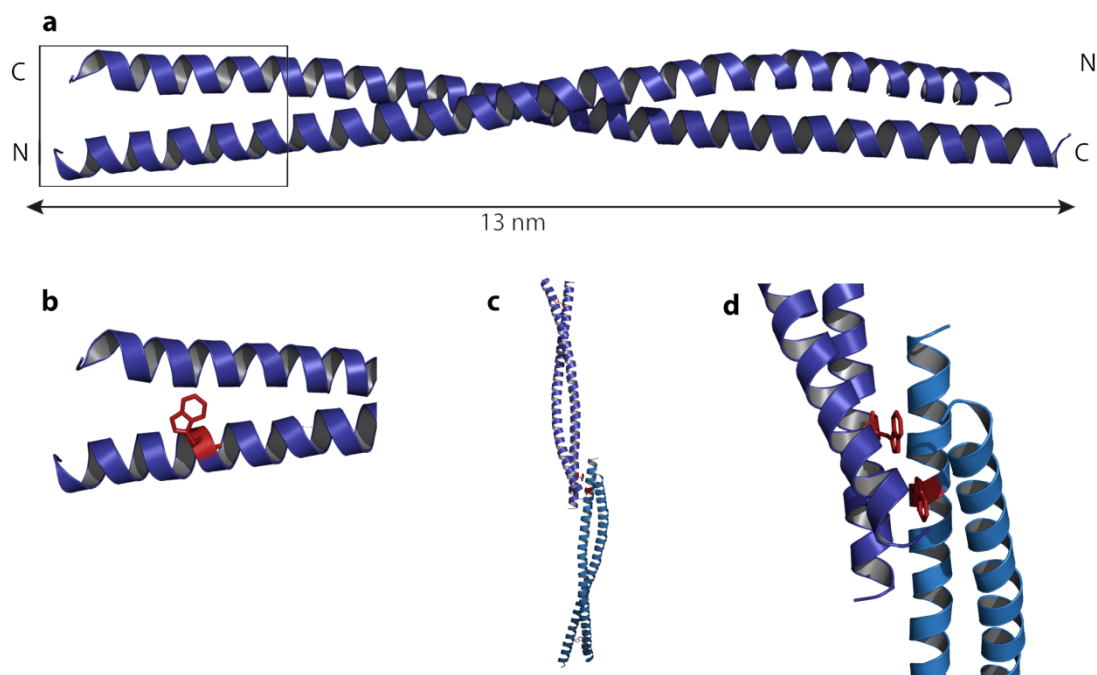
Figure 24 Crystal structure of the Ogna mini-rod. (a) Ribbon diagram of the refined model. The anti-parallel coiled-coil rod has a length of 13 nm. (b) Enlargement of the rectangular area in (a). The mutation of R→W is at the terminal part of the coiled coil, with the tryptophan side-chain pointing outwards. (c) Symmetry-related molecules in the crystal lattice. (d) The tryptophan residue W1999 is involved in crystal contacts with neighbouring molecules in the crystal lattice.

To resolve the packing disorder of the crystal, the Ogna mini-rod was re-purified and subjected to lysine methylation, which alters surface charges of a target protein and may change the crystal packing. Ogna mini-rod contains 6 lysines that were modified by the method as described in Materials & Methods (chapter 5.4). The methylated protein crystallised in 0.1 M sodium acetate pH 4, 20% PEG 400 and 0.1 M $CaCl_2$ (or 0.1 M $MgCl_2$). Diffraction data was collected to 3.3 Å resolution (Figure 23b). To further improve the diffraction data, crystal dehydration was tested, which has been shown to be effective in obtaining a better resolution (Heras et al., 2003). The dehydrated protein crystals did not show an improved diffraction data. The final structure was obtained with a resolution of 3.3 Å (Figure 24a). The protein crystallised in space group I422. The summary of the data collection and the refinement statistics are shown in Table 8.

The short coiled-coil rod is a dimer oriented in an anti-parallel manner. The first twelve amino acids at the N-terminus and the last eight residues at the C-terminus are missing in the final structure. The mutation R1999W is located close to the N-

terminus of each strand (Figure 24b). Closer examination revealed that W1999 is involved in crystal contacts within the crystal lattice (Figure 24c), which explains why the wt form of the same construct could not be crystallised under the same condition. Figure 25 shows the crystal packing of the dimeric protein from the three different axes.
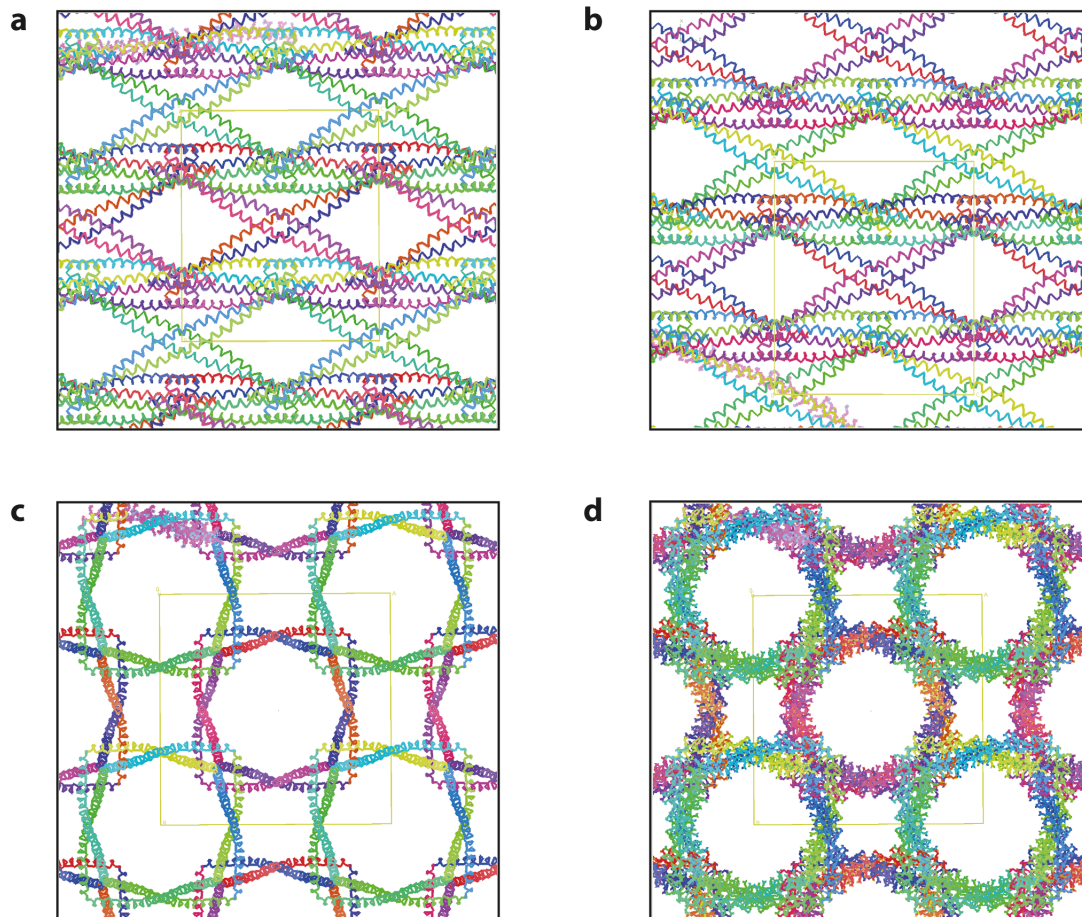
Figure 25 Crystal packing of the Ogna mini-rod. The arrangement of the Ogna mini-rod dimers in the crystal lattice is shown by looking down the (a) a-axis, (b) b-axis, and (c) c-axis. (d) The same view as (c) with all side chains shown. The crystal has a solvent content of 75%. The central yellow squares in the figures mark the unit cell.

Although the SLS results of plectin mini-rod suggest the protein to be a monomer in solution (Figure 20c), in the crystal it is clearly a dimer. It is likely that the protein is not completely in a dimerised state in solution, but crystallisation favoured the dimerised protein.

To compare the Ogna structure with wild-type plectin, I also attempted to crystallise wt-plectin mini-rod but did not succeed in obtaining good crystals. The protein

crystallised in only small needle-like clusters, which were unsuitable for data collection. Further optimisations including streak- or micro-seeding were not successful in obtaining single, diffracting crystals. It is likely that the replacement of arginine by tryptophan, which contributes to crystal contacts in the Ogna mini-rod (Figure 24c, d), is critical in obtaining well ordered packing of the molecules in a crystal. Attempts to crystallise larger parts of the coiled-coil rod were also unsuccessful.

6.4 Negative staining electron microscopy studies

Since it was not possible to obtain a crystal structure for the other coiled-coil constructs aside from Ogna mini-rod, electron microscopy (EM) was used to study potential structural differences between the wild-type and mutant plectin. MBP-10×His-tagged plectin M-rod, both wild-type and Ogna, were purified using Ni-NTA affinity chromatography and subsequently labelled with 5-nm nano-gold (chapter 5.7).
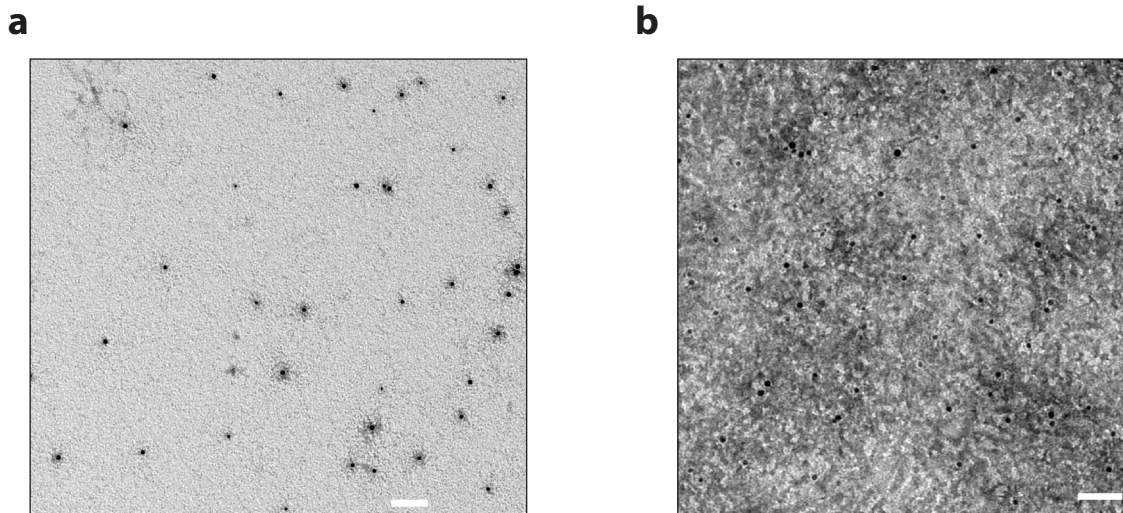
**Figure 26 Electron microscopic studies of nano-gold labelled plectin.** (a) Wild-type MBP-plectin M-rod and (b) MBP-Ogna M-rod were labelled using 5-nm nano-gold and stained by uranyl-acetate. The nano-gold label is visible as black dot. Scale bars: 50 nm.

In the case of a parallel arrangement of the coiled coil, both labels should be close to each other, whereas in an anti-parallel arrangement the labels should have a distance

of 60 nm. Although the nano-gold particles were clearly visible, no consistent distribution pattern was observed (Figure 26).

6.5 Electron paramagnetic resonance studies

To investigate whether there is a difference in the coiled-coil arrangement of the wild-type and the Ogna plectin rod domain, electron paramagnetic resonance spectroscopy (EPR) was used as an alternative to protein crystallisation and EM studies. In short, this technique allows measuring the distance between paramagnetic spin labels up to 8 nm in a biological macromolecule. The paramagnetic spin label, usually MTSSL (chapter 5.8), is attached via a cysteine-disulfide bridge to the protein (Figure 27a).
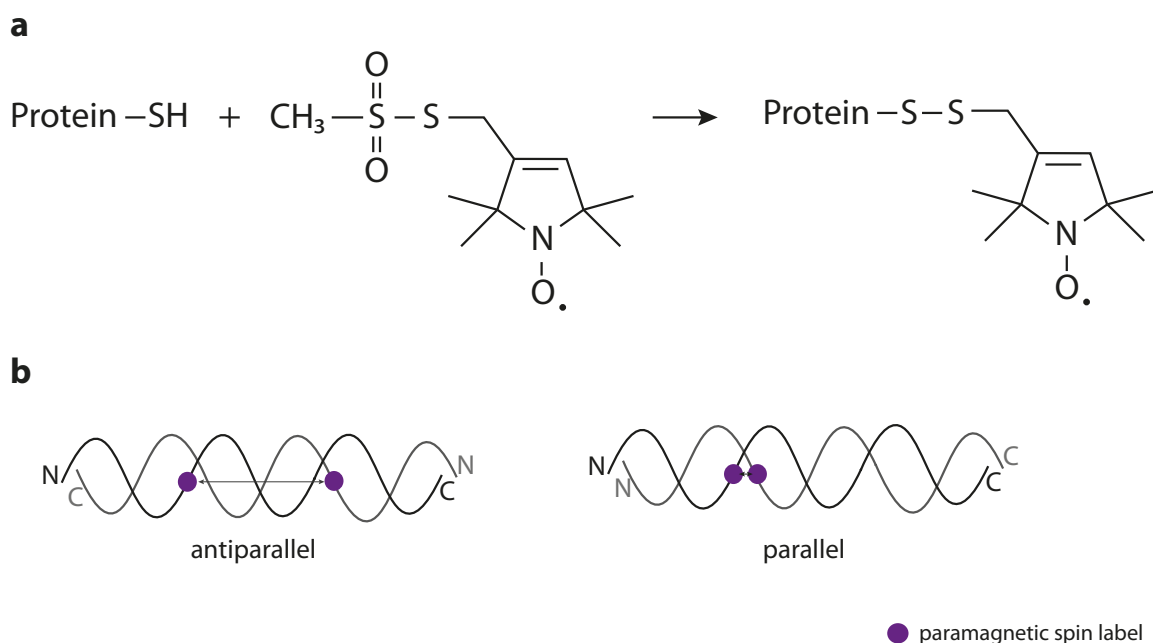
Figure 27 Principle of EPR spin label attachment. (a) The paramagnetic spin label (MTSSL, in our case) is attached to an accessible cysteine residue in the protein of interest. (b) Depending on the orientation of a coiled coil, the spin labels can be in distant or close position. EPR allows to measure the distance between the spin labels and to allow the identification of the orientation of the coiled coil.

Due to the lack of cysteine residues in the plectin coiled-coil rod, cysteine had to be introduced in order to be able to label the protein.

Since full-length recombinant plectin rod domain purified from bacteria easily degraded, two shorter coiled-coil constructs were used for this study. Plectin mini- and M-rod, both wild-type and Ogna were tested. Based on the crystal structure of Ogna mini-rod, a lysine at position 2043 was mutated to cysteine (Figure 28, highlighted in brown). Aside from its accessibility, the computed distance between the introduced cysteines in the dimer was optimal for the EPR measurements. At this position, the distance of the anti-parallel dimer was calculated to be 3.5 nm. In a parallel orientation the distance of the spin labels was estimated to be lower than 2 nm, making both conformations measureable for either pulsed (double electron electron resonance - DEER) or low-temperature continuous wave (cw) EPR (Figure 27b).
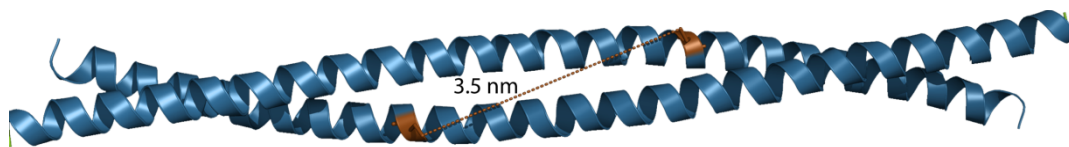
Figure 28 Illustration of the two K2043 residues on the anti-parallel Ogna mini-rod dimer.

DEER measurements showed the expected anti-parallel arrangement of Ogna-K2043C mini-rod with a distance distribution of 3.3 nm (Figure 29a, c). Interestingly, plectin-K2043C mini-rod also showed a similar distance of 3.2 nm (Figure 29b, c), indicating an anti-parallel arrangement of the coiled coil for both constructs. Measuring of the larger construct M-rod revealed that both wild-type plectin and Ogna showed no distance larger than 2 nm (Figure 29d, e, f).

Since 2 nm are at the lower limit of DEER measurements, a different experimental setup had to be used to determine the exact distance between labelled sites of M-rod constructs. Cw-EPR spectra collected at 160 K are known to broaden due to spin-spin dipolar interactions if the spins are in a distance below 2 nm (Steinhoff et al., 1997).
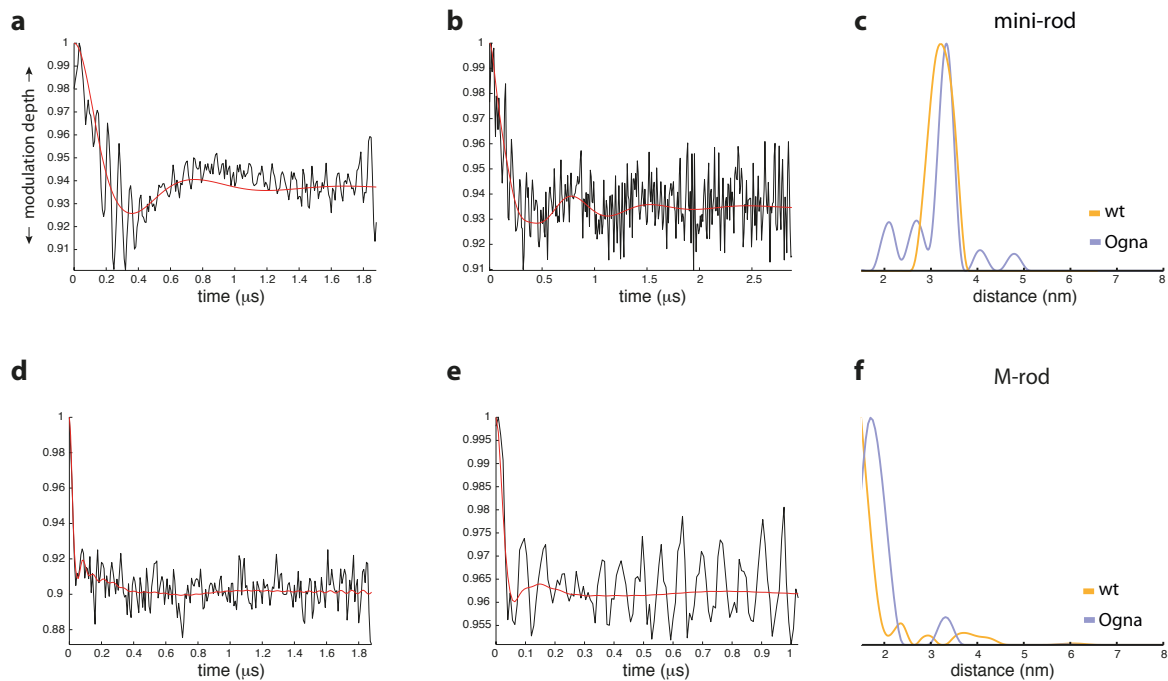
Figure 29 DEER measurements of the M- and mini-rod of Ogna and wild-type plectin. Purified protein was labelled using the paramagnetic spin label MTSSL and distances were measured by pulsed EPR. (a & b) The form factors of (a) wild-type and (b) Ogna mini-rod are shown. (c) The computed distance distribution for the mini-rod constructs. (d - f) The results for plectin M-rod are given. Spectra of (d) wild-type and (e) Ogna are shown. (a, b, d, e) The red line indicates the fitted curve used to compute the distance. (c & f) The resulting distance distribution was calculated for wt (yellow) and Ogna (blue) plectin.

Using a control sample with only 1 spin-label per dimer (for sample preparation, see chapter 5.8), the broadening of the double-labelled sample spectra compared to the single-labelled spectra was evaluated and used to determine the distance of the interacting spins. Plectin-K2043C mini-rod served as the control sample for the measurements. Spectra of the spin labelled proteins and the control sample were recorded at 160 K by cw-EPR (Figure 30).

As expected, no broadening of plectin or Ogna-K2043C mini-rod spectra was observed (Figure 30a, b). Both wild-type and Ogna plectin-K2043C M-rod spectra showed a clear broadening compared to the control sample (Figure 30c, d). A distance of 1.8 nm between the spin labels was calculated. These results showed that the crystallised mini-rod is anti-parallel regardless of the R1999W mutation. Interestingly, a longer part of the middle coiled-coil segment (M-rod) showed a parallel arrangement. Therefore, although different constructs of the rod domain showed different orientations of the two strands, the mutation R1999W did not

change the conformation within the same region examined in comparison to wild-type plectin. It can be concluded that the full-length rod domain likely adopts a parallel coiled-coil dimer while the crystal structure Ogna mini-rod may represent a local anti-parallel interaction.
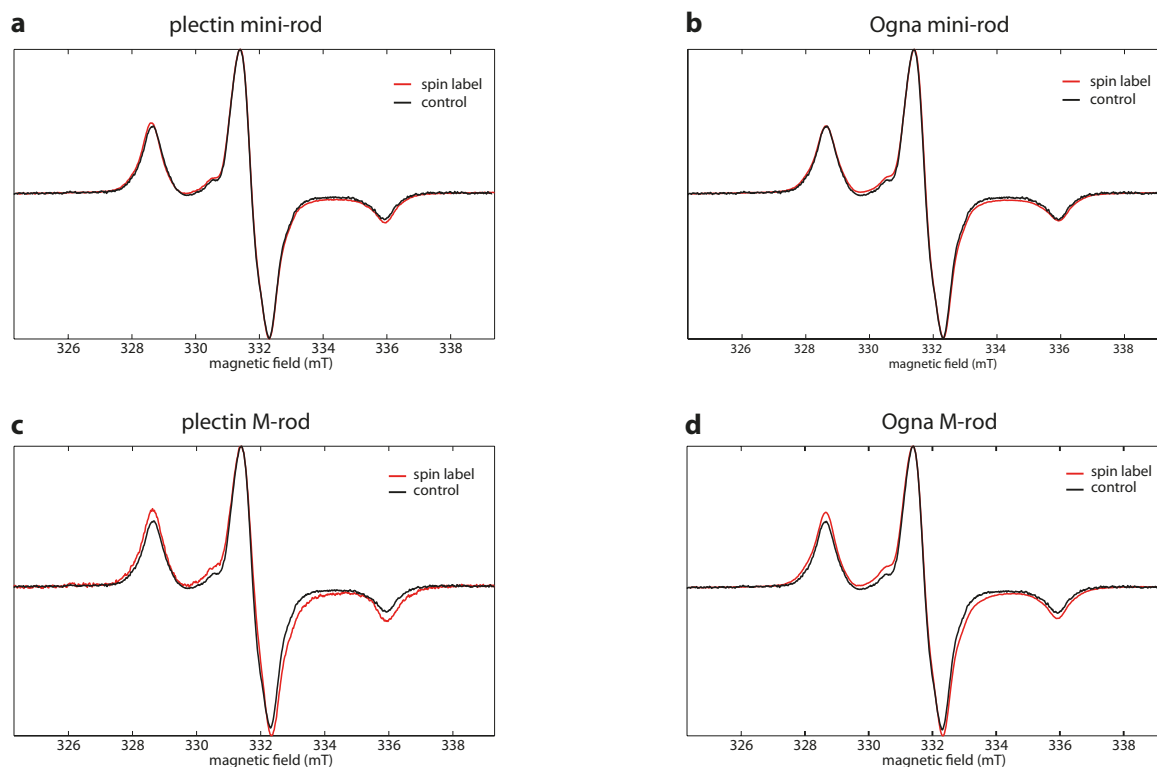
Figure 30 Low-temperature cw-EPR measurements of the M- and mini-rod of Ogna and wild-type plectin. (a - d) Purified protein was labelled with paramagnetic spin label and was measured at 160 K by cw-EPR (red spectra). As a control, spectra of spin diluted (single-labelled) protein were collected (black). The broadening of the spectra was used to compute the distance between the spin labels. Spectra of wild-type (a, c) and Ogna (b, d) for mini- (a, b) and M-rod (c, d) are shown.

The form factors of all the constructs from the DEER measurements indicated a rather low modulation depth. The modulation depth indicates the number of coupled spins in the analysed system. In a coiled-coil system the expected number of coupled spins would correspond to 2, which was not achieved by any of the samples analysed by DEER. Instead, the average number of coupled spins was ~1.2. This suggests that the protein, regardless of construct and/or mutation, is not in a complete dimerised state and this would also support the SLS results observed for plectin wt/R1999W mini-rod (Figure 20c).

To further investigate the integrity of the coiled-coil, other amino acid residues were mutated and measured by EPR. K1883 and E2149 were separately changed to cysteine in plectin M-rod of wild-type and Ogna. Both positions were predicted to be at the position b and f of the heptad repeat, thus likely to be accessible for the spin label. Low-temperature cw-EPR revealed that for both mutations, K1883C and E2149C, no short distance was detected, regardless of plectin or Ogna (data not shown). It is possible that the coiled-coil structure at the terminal regions of plectin M-rod is opening up to some extent, leading to the absence of any short distance.

Table 9 Spin label efficiency

Sample	Protein : MTSSL	Label efficiency (%)
Plectin mini-rod	1:8	93.01
Ogna mini-rod	1:8	41.44
	1:20	90.56
Plectin M-rod	1:8	88.79
Ogna M-rod	1:8	65.86

It is noteworthy that, although the EPR data did not show any difference between wild-type and mutant plectin within the respective constructs, higher spin label efficiency was observed for plectin in comparison to Ogna throughout all labelling experiments (Table 9).

6.6   Rotary metal shadowing EM studies

Due to the different EPR results observed for plectin/Ogna mini- and M-rod, rotary metal shadowing experiments were conducted to assess the orientation of the full-length coiled-coil rod of wild-type plectin. A construct spanning residues 898-2501 of plectin was used for this purpose. This construct contains the C-terminal 478 amino acids of the plakin domain (i.e. the last four spectrin repeats) preceding the plectin coiled-coil domain (Figure 31a) and was expressed in the baculovirus/insect cell system (see part II, section 5.2.1, Table 5).
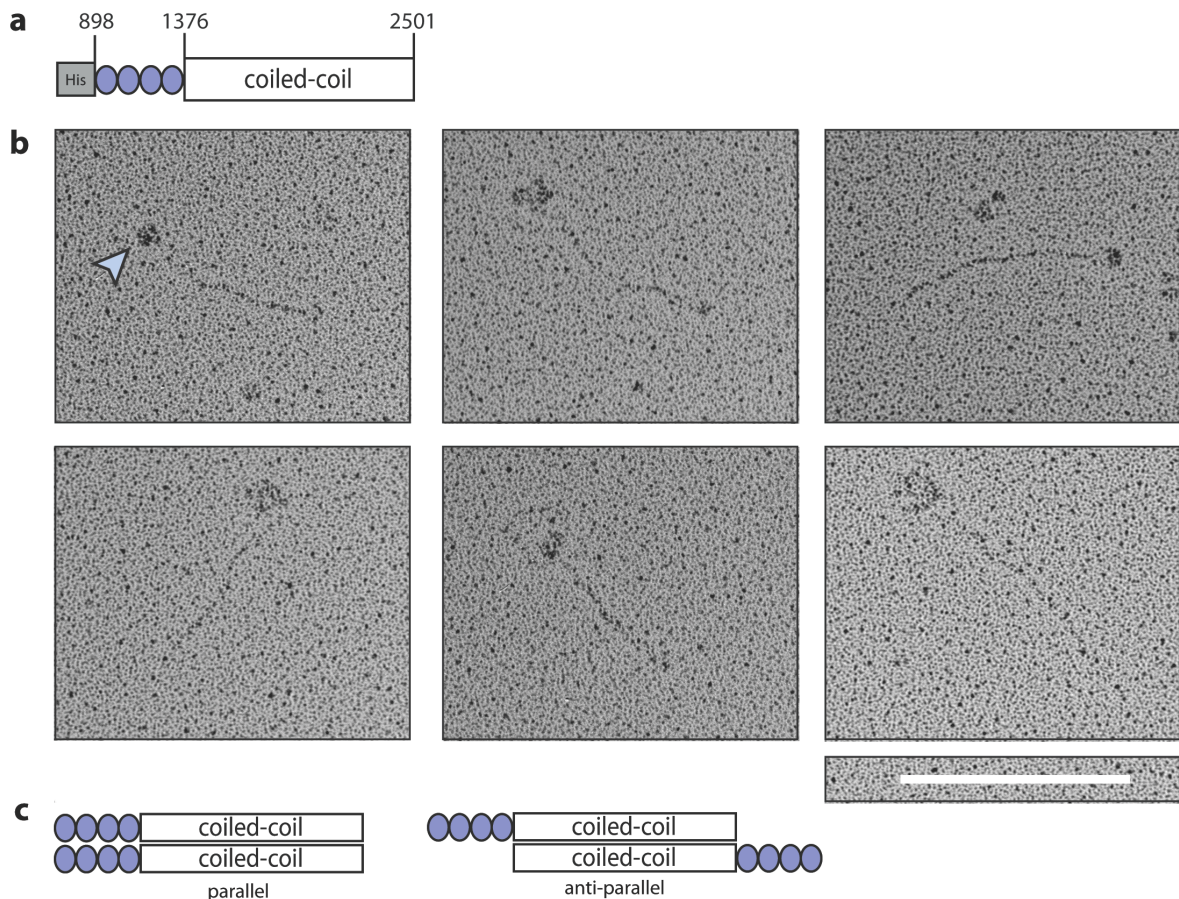
Figure 31 Rotary metal shadowing EM micrographs of the full-length plectin coiled coil with the preceding spectrin repeats. (a) A schematic representation of the plectin construct used for rotary metal shadowing. A fragment of the plakin domain and the coiled-coil domain were expressed in insect cells. (b) Rotary metal shadowing EM micrographs. The images repeatedly show the same structure containing a "head" (blue arrowhead) and a 135 – 190 nm long "tail". Scale bar: 200 nm. (c) A schematic representation of the potential arrangements of the used construct.

The linear coiled-coil domain can be clearly seen on various positions on the grid (Figure 31b). Length measurements showed that the coiled coils are between 140 and 190 nm long, with the majority being approximately 180 nm long. This is going in line with the theoretical length of 170 nm for the fully extended coiled-coil domain. Interestingly, the four spectrin repeats in front of the coiled-coil were consistently observed on only one end of the rod domain (Figure 31b, blue arrowhead). This suggests a parallel arrangement of the full-length plectin coiled coil (Figure 31b).

7   Discussion

Plectin - as a versatile cytolinker - is of crucial importance in the maintenance of the cytoskeleton integrity (Andrä et al., 1998), (Hijikata et al., 1999). Along with other proteins, plectin is a constitutive component of hemidesmosomes and dysfunctions of these proteins have been linked to the disease epidermolysis bullosa (EB) (Uitto and Richard, 2004). Among the more than 30 mutations identified in plectin related to the onset of EB, the Ogna mutant is of particular interest because it represents the only autosomal dominant mutation in plectin (Pfendner et al., 2005). As mentioned above, this mutation is a single amino acid change from arginine to tryptophan at position 2000 of the coiled-coil region of human plectin (Koss-Harnes et al., 2002) and position 1999 of mouse plectin.

Using the coiled-coil prediction program COILS (Lupas et al., 1991), it is predicted that the arginine 1999 is at the position *f* of the heptad repeat (Figure 32) – on the surface of a coiled-coil dimer. While the overall heptad repeat positions for the individual amino acids do not change between wild-type and mutant, the position W1999 and its preceding amino acid Q1998 are predicted to shift from *f* to *d* and *e* to *c*, respectively. The replacement of a charged residue by the hydrophobic tryptophan may influence the coiled-coil stability in that region because of difficulties in packing the bulky aromatic tryptophan side chain into the coiled-coil interface.
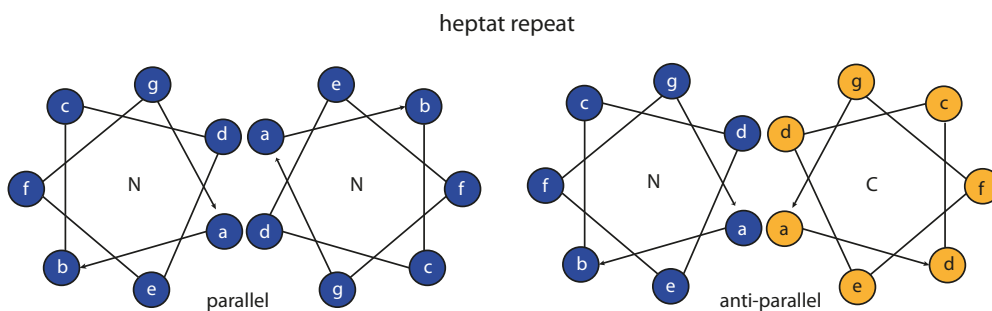
Figure 32 Schematic representation of the heptad repeat (*a-g*) of parallel and anti-parallel coiled-coil dimers. Positions *a* and *d* of the coiled coil dimer are mostly hydrophobic residues - important for stabilising the coiled coil interaction, whereas positions *e* and *g* are often occupied by charged residues (Wagschal et al., 1999). Both parallel and anti-parallel dimer orientations are shown.

7.1 Recombinant wild-type plectin forms large assemblies

Full-length plectin assembles into dimers via its coiled-coil domain (Wiche and Winter, 2011). Assemblies of different higher oligomeric structures have been observed, which was proposed to occur via the globular domains flanking the central rod of the protein (Wiche, 1989). Recombinant plectin-rod domain expressed in insect cells formed higher order structures in addition to dimers (Walko et al., 2011), suggesting that the coiled-coil domain is also able to form oligomers. A recent model proposed a lateral arrangement of plectin to be important for stabilising the hemidesmosomes (Walko et al., 2011).

Despite the large size of the full-length recombinant coiled-coil domain, I was able to express it in *E. coli* (Figure 19e). Interestingly, I found the recombinant plectin rod expressed in bacteria to be largely in a monomeric state, aside from higher oligomers/aggregates. Additionally, the rod domain readily degraded to a size of 50kDa. Nevertheless, it was observed that bacterial expressed wild-type plectin rod domain forms higher oligomers to a larger extent than Ogna does (Figure 22). The mutation is altering the oligomerisation behaviour of plectin. Thus, it might be possible that the mutation R1999W influences the protein's ability to associate into larger structures. This was also discussed in a recent publication of Walko et al (Walko et al., 2011), where they observed different oligomerisation behaviour of the plectin/Ogna rod domain via electron microscopy studies. The diminished ability of Ogna to form this aggregates could be linked to the observed defects in EBS-Ogna (Walko et al., 2011). It has been reported for a dimeric coiled-coil protein (Bcr) that mutation of specific residues in the anti-parallel dimer are resulting in different oligomeric states of the protein (Taylor and Keating, 2005).

7.2 The plectin rod domain is likely to be a parallel dimer

To gain more insights into the influence of the R1999W mutation on the structural integrity of plectin, extensive crystallographic studies of fragments of the coiled-coil domain were conducted. The shortest construct – mini-rod - of the Ogna mutant was successfully crystallised and the structure showed an anti-parallel arrangement of the

coiled coil (Figure 24). Crystallisation of the wild-type counterpart plectin mini-rod was not successful. Although small needle clusters were observed, it was not possible to improve these crystals. The missing tryptophan 1999 that is involved in crystal contacts in the mutant plectin could be the reason. The loss of the stabilising interaction between neighbouring molecules might have influenced the crystallisation negatively. By means of EPR, I was able to show that both plectin and Ogna mini-rod have the same orientation, indicating that the mutation does not influence the orientation of the coiled-coil rod.

Surprisingly, the coiled-coil orientation changed when the larger M-rod construct was studied by EPR (Figure 29, Figure 30). Although the chosen length of the small construct was expected to represent the whole coiled-coil region, this seemed to not be the case. It could be possible, that the anti-parallel orientation is more favourable for the short region from 1975-2081 (mini-rod), but not for the longer region from 1808-2189 (M-rod). Rotary metal shadowing data of a construct containing four spectrin repeats in front of the coiled-coil domain showed the globular fragment only at one end of the coiled-coil dimer (Figure 31b). This, in combination with the observed inability of the N- and C- rod to interact, further supports a parallel arrangement of plectins coiled-coil domain.

7.3 Recombinant plectin only partly dimerises

An interesting finding during the diverse studies was the incomplete dimerisation stage of the recombinant protein. Both EPR and SLS studies revealed that plectin, regardless of wild-type or the mutant R1999W, is to some extent found in a monomeric state. The low modulation-depth observed by EPR measurements was the first indication of the incomplete dimerisation of plectin. The SLS-results of plectin mini-rod (wt/Ogna), M-rod (Ogna) and full-length (wt/Ogna), supported this finding (Figure 20). It is uncertain whether the bacterial expression system or the subsequent purification strategy contributes to the incomplete dimerisation.

The absence of short distances in the mutants K1883C and E2149C of M-rod construct (wt/Ogna) also demonstrates that the termini of the mid-part of the coiled-

coil rod are not in close vicinity, implying that this construct may only dimerise partly via its middle segment (Figure 33).
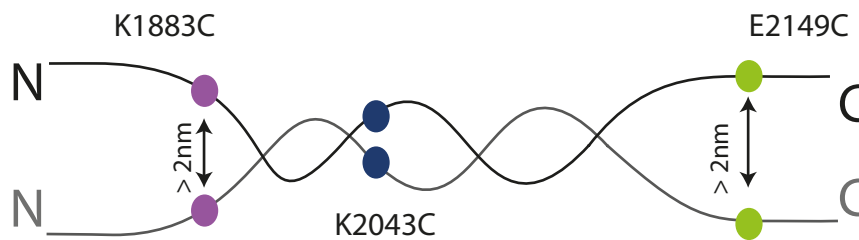
Figure 33 Schematic representation of the EPR results for the M-rod. From the three different mutations tested by EPR, a model can be deduced. While the middle segment of plectin M-rod is a dimer, as indicated by mutation K2043C, both termini are not in the range of 2 nm, i.e. they are open at the ends.

7.4   Difference between wild-type and R1999W plectin

As mentioned in the introduction (part II, chapter 3), a current model of how the mutation of R1999→W influences the integrity of plectin states that a local destabilisation of the coiled-coil region due to the R1999W mutation makes the mutant plectin more susceptible to proteolytic degradation (Walko et al., 2011). During my experiments no differences in general degradation pattern were observed. If degradation occurred as for the full-length construct purified from bacteria, both plectin and Ogna seemed to be degraded to the same extent. Whether the putative degradation is connected with the different oligomerisation behaviour of the wild-type and mutant plectin still awaits to be investigated.

Wild-type and mutant plectin behaved similarly during the purification with the exception of their different oligomerisation capability. During the cross-linking studies I observed that wild-type plectin M- and mini-rod were cross-linked to a larger extent than the Ogna counterparts (Figure 20f). Whether this also reflects their dissimilar oligomerisation behaviour still needs to be investigated.

Interestingly, during spin-labelling experiments it was noticed that Ogna is more difficult to label than its wild-type counterpart. All EPR-constructs of Ogna displayed lower label efficiency. In the case of Ogna mini-rod-K2043C, the spin label had to be

increased from eight- to 20-fold in excess. If the mutation does in fact create a local disarrangement of the coiled coil, the neighbouring residues might be less accessible for the spin label. It is worth testing in the future the distances of the coiled coil in close proximity of the R1999W mutation in order to investigate potential disruptions of the coiled-coil stability.

The data presented here relied on the assumption that the shorter coiled-coil segments behave similarly to the full-length rod. Due to the different results obtained for the diverse constructs, future studies should focus on the full-length rod. EPR studies of the full-length rod domain, purified from *E. coli* were not successful. This was due to both low yields and the degradation of the large construct. Studying the insect-cell expressed full-length construct by EPR was also not successful because the labelled protein readily aggregated during concentration and EPR measurements were not possible. Optimisation of buffers and purification strategies should be carried out to achieve higher concentration necessary for EPR and other biophysical studies.

In conclusion, this study showed an influence on the oligomerisation state of plectin dependent on the mutation R1999W, but no differences on the ultrastructural level have been discovered so far. Characterisation of the potential influences on plectin's function by the mutation R1999W will greatly promote the development of putative therapies for patients affected with EBS.

8 References Part I & Part II

Adhiambo, C., T. Blisnick, G. Toutirais, E. Delannoy, and P. Bastin. 2009. A novel function for the atypical small G protein Rab-like 5 in the assembly of the trypanosome flagellum. *J Cell Sci*. 122:834-41.

Afzelius, B.A. 1976. A human syndrome caused by immotile cilia. *Science*. 193:317-9.

Ahmed, N.T., C. Gao, B.F. Lucker, D.G. Cole, and D.R. Mitchell. 2008. ODA16 aids axonemal outer row dynein assembly through an interaction with the intraflagellar transport machinery. *J Cell Biol*. 183:313-22.

Alberts, B., A. Johnson, J. Lewis, M. Raff, K. Roberts, and P. Walter. 2002. Molecular Biology of the Cell. Garland Science.

Andrä, K., I. Kornacker, A. Jörgl, M. Zörer, D. Spazierer, P. Fuchs, I. Fischer, and G. Wiche. 2003. Plectin-isoform-specific rescue of hemidesmosomal defects in plectin (-/-) keratinocytes. *J Invest Dermatol*. 120:189-97.

Andrä, K., B. Nikolic, M. Stocher, D. Drenckhahn, and G. Wiche. 1998. Not just scaffolding: plectin regulates actin dynamics in cultured cells. *Genes Dev*. 12:3442-51.

Badano, J.L., N. Mitsuma, P.L. Beales, and N. Katsanis. 2006. The ciliopathies: an emerging class of human genetic disorders. *Annu Rev Genomics Hum Genet*. 7:125-48.

Baker, S.A., K. Freeman, K. Luby-Phelps, G.J. Pazour, and J.C. Besharse. 2003. IFT20 links kinesin II with a mammalian intraflagellar transport complex that is conserved in motile flagella and sensory cilia. *J Biol Chem*. 278:34211-8.

Baldari, C.T., and J. Rosenbaum. 2009. Intraflagellar transport: it's not just for cilia anymore. *Current Opinion in Cell Biology*.

Battye, T.G., L. Kontogiannis, O. Johnson, H.R. Powell, and A.G. Leslie. 2011. iMOSFLM: a new graphical interface for diffraction-image processing with MOSFLM. *Acta Crystallogr D Biol Crystallogr*. 67:271-81.

Beales, P.L., E. Bland, J.L. Tobin, C. Bacchelli, B. Tuysuz, J. Hill, S. Rix, C.G. Pearson, M. Kai, J. Hartley, C. Johnson, M. Irving, N. Elcioglu, M. Winey, M. Tada, and P.J. Scambler. 2007. IFT80, which encodes a conserved intraflagellar transport protein, is mutated in Jeune asphyxiating thoracic dystrophy. *Nat Genet*. 39:727-9.

Behal, R.H., E. Betleja, and D.G. Cole. 2009. Purification of IFT particle proteins and preparation of recombinant proteins for structural and functional analysis. *Methods in Cell Biology: VOLUME 93.* 93:179-96.

Behal, R.H., M.S. Miller, H. Qin, B.F. Lucker, A. Jones, and D.G. Cole. 2012. Subunit Interactions and Organization of the Chlamydomonas reinhardtii Intraflagellar Transport Complex A Proteins. *J Biol Chem.* 287:11689-703.

Berbari, N.F., A.K. O'Connor, C.J. Haycraft, and B.K. Yoder. 2009. The primary cilium as a complex signaling center. *Curr Biol.* 19:R526-35.

Berger, I., D.J. Fitzgerald, and T.J. Richmond. 2004. Baculovirus expression system for heterologous multiprotein complexes. *Nat Biotechnol.* 22:1583-7.

Bhogaraju, S., M. Taschner, M. Morawetz, C. Basquin, and E. Lorentzen. 2011. Crystal structure of the intraflagellar transport complex 25/27. *The EMBO Journal.*

Bhowmick, R., M. Li, J. Sun, S.A. Baker, C. Insinna, and J.C. Besharse. 2009. Photoreceptor IFT complexes containing chaperones, guanylyl cyclase 1 and rhodopsin. *Traffic.* 10:648-63.

Blacque, O.E., S. Cevik, and O.I. Kaplan. 2008. Intraflagellar transport: from molecular characterisation to mechanism. *Front Biosci.* 13:2633-52.

Blacque, O.E., C. Li, P.N. Inglis, M.A. Esmail, G. Ou, A.K. Mah, D.L. Baillie, J.M. Scholey, and M.R. Leroux. 2006. The WD repeat-containing protein IFTA-1 is required for retrograde intraflagellar transport. *Molecular Biology of the Cell.* 17:5053-62.

Borradori, L., and A. Sonnenberg. 1999. Structure and function of hemidesmosomes: more than simple adhesion complexes. *J Invest Dermatol.* 112:411-8.

Brazelton, W.J., C.D. Amundsen, C.D. Silflow, and P.A. Lefebvre. 2001. The bld1 mutation identifies the Chlamydomonas osm-6 homolog as a gene required for flagellar assembly. *Curr Biol.* 11:1591-4.

Brito, D.A., S.M. Gouveia, and M. Bettencourt-Dias. 2012. Deconstructing the centriole: structure and number control. *Current Opinion in Cell Biology.*

Brown, M.J., J.A. Hallam, Y. Liu, K.M. Yamada, and S. Shaw. 2001. Cutting edge: integration of human T lymphocyte cytoskeleton by the cytolinker plectin. *J Immunol.* 167:641-5.

Brunger, A.T., P.D. Adams, G.M. Clore, W.L. DeLano, P. Gros, R.W. Grosse-Kunstleve, J.S. Jiang, J. Kuszewski, M. Nilges, N.S. Pannu, R.J. Read, L.M. Rice, T. Simonson, and G.L. Warren. 1998. Crystallography & NMR system: A new software suite for macromolecular structure determination. *Acta Crystallogr D Biol Crystallogr.* 54:905-21.

Buchan, D.W., S.M. Ward, A.E. Lobley, T.C. Nugent, K. Bryson, and D.T. Jones. 2010. Protein annotation and modelling servers at University College London. *Nucl Acids Res*. 38:W563-W568.

Chavanas, S., L. Pulkkinen, Y. Gache, F.J. Smith, W.H. McLean, J. Uitto, J.P. Ortonne, and G. Meneguzzi. 1996. A homozygous nonsense mutation in the PLEC1 gene in patients with epidermolysis bullosa simplex with muscular dystrophy. *J Clin Invest*. 98:2196-200.

Chih, B., P. Liu, Y. Chinn, C. Chalouni, L.G. Komuves, P.E. Hass, W. Sandoval, and A.S. Peterson. 2012. A ciliopathy complex at the transition zone protects the cilia as a privileged membrane domain. *Nat Cell Biol*. 14:61-72.

Clark, K.A., A.S. McElhinny, M.C. Beckerle, and C.C. Gregorio. 2002. Striated muscle cytoarchitecture: an intricate web of form and function. *Annu Rev Cell Dev Biol*. 18:637-706.

Cole, D.G. 2003. The intraflagellar transport machinery of Chlamydomonas reinhardtii. *Traffic*. 4:435-42.

Cole, D.G., D.R. Diener, A.L. Himelblau, P.L. Beech, J.C. Fuster, and J. Rosenbaum. 1998. Chlamydomonas kinesin-II-dependent intraflagellar transport (IFT): IFT particles contain proteins required for ciliary assembly in Caenorhabditis elegans sensory neurons. *J Cell Biol*. 141:993-1008.

Cole, D.G., and W.J. Snell. 2009. SnapShot: Intraflagellar transport. *Cell*. 137:784-784.e1.

Craige, B., C.-C. Tsao, D.R. Diener, Y. Hou, K.-F. Lechtreck, J. Rosenbaum, and G.B. Witman. 2010. CEP290 tethers flagellar transition zone microtubules to the membrane and regulates flagellar protein content. *The Journal of Cell Biology*. 190:927-40.

Czarnecki, P.G., and J.V. Shah. 2012. The ciliary transition zone: from morphology and molecules to medicine. *Trends in Cell Biology*.

Dave, D., D. Wloga, N. Sharma, and J. Gaertig. 2009. DYF-1 Is required for assembly of the axoneme in Tetrahymena thermophila. *Eukaryotic Cell*. 8:1397-406.

Dawe, H.R., U.M. Smith, A.R. Cullinane, D. Gerrelli, P. Cox, J.L. Badano, S. Blair-Reid, N. Sriram, N. Katsanis, T. Attie-Bitach, S.C. Afford, A.J. Copp, D.A. Kelly, K. Gull, and C.A. Johnson. 2007. The Meckel-Gruber Syndrome proteins MKS1 and meckelin interact and are required for primary cilium formation. *Hum Mol Genet*. 16:173-86.

de Pereda, J.M., M.P. Lillo, and A. Sonnenberg. 2009. Structural basis of the interaction between integrin alpha6beta4 and plectin at the hemidesmosomes. *EMBO J*. 28:1180-90.

Deane, J.A., D.G. Cole, E.S. Seeley, D.R. Diener, and J. Rosenbaum. 2001. Localization of intraflagellar transport protein IFT52 identifies basal body transitional fibers as the docking site for IFT particles. *Curr Biol*. 11:1586-90.

Delaval, B., A. Bright, N.D. Lawson, and S. Doxsey. 2011. The cilia protein IFT88 is required for spindle orientation in mitosis. *Nat Cell Biol*. 13:461-8.

Elliott, C.E., B. Becker, S. Oehler, M.J. Castanon, R. Hauptmann, and G. Wiche. 1997. Plectin transcript diversity: identification and tissue distribution of variants with distinct first coding exons and rodless isoforms. *Genomics*. 42:115-25.

Emmer, B.T., D. Maric, and D.M. Engman. 2010. Molecular mechanisms of protein and lipid targeting to ciliary membranes. *J Cell Sci*. 123:529-36.

Emsley, P., and K. Cowtan. 2004. Coot: model-building tools for molecular graphics. *Acta Crystallogr D Biol Crystallogr*. 60:2126-32.

Evans, P. 2006. Scaling and assessment of data quality. *Acta Crystallogr D Biol Crystallogr*. 62:72-82.

Fan, Z.-C., R.H. Behal, S. Geimer, Z. Wang, S.M. Williamson, H. Zhang, D.G. Cole, and H. Qin. 2010. Chlamydomonas IFT70/CrDYF-1 Is a Core Component of IFT Particle Complex B and Is Required for Flagellar Assembly. *Molecular Biology of the Cell*.

Favre, B., Y. Schneider, P. Lingasamy, J.-E. Bouameur, N. Begré, Y. Gontier, M.-F. Steiner-Champliaud, M.A. Frias, L. Borradori, and L. Fontao. 2011. Plectin interacts with the rod domain of type III intermediate filament proteins desmin and vimentin. *Eur J Cell Biol*. 90:390-400.

Finetti, F., S.R. Paccani, M.G. Riparbelli, E. Giacomello, G. Perinetti, G.J. Pazour, J. Rosenbaum, and C.T. Baldari. 2009. Intraflagellar transport is required for polarized recycling of the TCR/CD3 complex to the immune synapse. *Nat Cell Biol*. 11:1332-9.

Fisch, C., and P. Dupuis-Williams. 2011. Ultrastructure of cilia and flagella - back to the future! *Biol Cell*. 103:249-70.

Flock, A., and A.J. Duvall. 1965. The ultrastructure of the kinocilium of the sensory cells in the inner ear and lateral line organs. *Journal of Cell Biology*. 25:1-8.

Foisner, R., F.E. Leichtfried, H. Herrmann, J.V. Small, D. Lawson, and G. Wiche. 1988. Cytoskeleton-associated plectin: in situ localization, in vitro reconstitution, and binding to immobilized intermediate filament proteins. *J Cell Biol*. 106:723-33.

Follit, J.A., J.T. San Agustin, F. Xu, J.A. Jonassen, R. Samtani, C.W. Lo, and G.J. Pazour. 2008. The Golgin GMAP210/TRIP11 anchors IFT20 to the Golgi complex. *PLoS Genet*. 4:e1000315.

Follit, J.A., R.A. Tuft, K.E. Fogarty, and G.J. Pazour. 2006. The intraflagellar transport protein IFT20 is associated with the Golgi complex and is required for cilia assembly. *Molecular Biology of the Cell*. 17:3781-92.

Follit, J.A., F. Xu, B.T. Keady, and G.J. Pazour. 2009. Characterization of mouse IFT complex B. *Cell Motil Cytoskeleton*. 66:457-68.

Fuchs, E., and K. Weber. 1994. Intermediate filaments: structure, dynamics, function, and disease. *Annu Rev Biochem*. 63:345-82.

Gaberc-Porekar, V., and V. Menart. 2001. Perspectives of immobilized-metal affinity chromatography. *J Biochem Biophys Methods*. 49:335-60.

Gache, Y., S. Chavanas, J.P. Lacour, G. Wiche, K. Owaribe, G. Meneguzzi, and J.P. Ortonne. 1996. Defective expression of plectin/HD1 in epidermolysis bullosa simplex with muscular dystrophy. *J Clin Invest*. 97:2289-98.

Garcia-Alvarez, B., A. Bobkov, A. Sonnenberg, and J.M. de Pereda. 2003. Structural and functional analysis of the actin binding domain of plectin suggests alternative mechanisms for binding to F-actin and integrin beta4. *Structure*. 11:615-25.

Garcia-Gonzalo, F.R., K.C. Corbit, M.S. Sirerol-Piquer, G. Ramaswami, E.A. Otto, T.R. Noriega, A.D. Seol, J.F. Robinson, C.L. Bennett, D.J. Josifova, J.M. García-Verdugo, N. Katsanis, F. Hildebrandt, and J.F. Reiter. 2011. A transition zone complex regulates mammalian ciliogenesis and ciliary membrane composition. *Nat Genet*. 43:776-84.

Gerdes, J.M., E.E. Davis, and N. Katsanis. 2009. The vertebrate primary cilium in development, homeostasis, and disease. *Cell*. 137:32-45.

Golovanov, A.P., G.M. Hautbergue, S.A. Wilson, and L.-Y. Lian. 2004. A simple method for improving protein solubility and long-term stability. *J Am Chem Soc*. 126:8933-9.

Gregor, M., A. Zeold, S. Oehler, K.A. Marobela, P. Fuchs, G. Weigel, D.G. Hardie, and G. Wiche. 2006. Plectin scaffolds recruit energy-controlling AMP-activated protein kinase (AMPK) in differentiated myofibres. *J Cell Sci*. 119:1864-75.

Gross, A., L. Columbus, K. Hideg, C. Altenbach, and W.L. Hubbell. 1999. Structure of the KcsA potassium channel from Streptomyces lividans: a site-directed spin labeling study of the second transmembrane segment. *Biochemistry*. 38:10324-35.

Haimo, L.T., and J.L. Rosenbaum. 1981. Cilia, flagella, and microtubules. *J Cell Biol*. 91:125s-130s.

Hartl, F.U., A. Bracher, and M. Hayer-Hartl. 2011. Molecular chaperones in protein folding and proteostasis. *Nature*. 475:324-32.

Hartl, F.U., and M. Hayer-Hartl. 2002. Molecular chaperones in the cytosol: from nascent chain to folded protein. *Science*. 295:1852-8.

Haycraft, C.J., P. Swoboda, P.D. Taulman, J.H. Thomas, and B.K. Yoder. 2001. The C. elegans homolog of the murine cystic kidney disease gene Tg737 functions in a ciliogenic pathway and is disrupted in osm-5 mutant worms. *Development*. 128:1493-505.

Heras, B., M.A. Edeling, K.A. Byriel, A. Jones, S. Raina, and J.L. Martin. 2003. Dehydration converts DsbG crystal diffraction from low to high resolution. *Structure*. 11:139-45.

Hijikata, T., T. Murakami, M. Imamura, N. Fujimaki, and H. Ishikawa. 1999. Plectin is a linker of intermediate filaments to Z-discs in skeletal muscle fibers. *J Cell Sci*. 112 (Pt 6):867-76.

Hou, Y., H. Qin, J.A. Follit, G.J. Pazour, J. Rosenbaum, and G.B. Witman. 2007. Functional analysis of an individual IFT protein: IFT46 is required for transport of outer dynein arms into flagella. *J Cell Biol*. 176:653-65.

Hoyer-Fender, S. 2010. Centriole maturation and transformation to basal body. *Semin Cell Dev Biol*. 21:142-7.

Hudak, L.M., S. Lunt, C.H. Chang, E. Winkler, H. Flammer, M. Lindsey, and B.D. Perkins. 2010. The intraflagellar transport protein ift80 is essential for photoreceptor survival in a zebrafish model of jeune asphyxiating thoracic dystrophy. *Invest Ophthalmol Vis Sci*. 51:3792-9.

Iomini, C., L. Li, J.M. Esparza, and S.K. Dutcher. 2009. Retrograde intraflagellar transport mutants identify complex A proteins with multiple genetic interactions in Chlamydomonas reinhardtii. *Genetics*. 183:885-96.

Ishikawa, H., and W.F. Marshall. 2011. Ciliogenesis: building the cell's antenna. *Nat Rev Mol Cell Biol*. 12:222-34.

Jeschke, G. 2006. DeerAnalysis2006—a comprehensive software package for analyzing pulsed ELDOR data. *Appl Magn Reson*. 30:473-498.

Jonassen, J.A., J. San Agustin, J.A. Follit, and G.J. Pazour. 2008. Deletion of IFT20 in the mouse kidney causes misorientation of the mitotic spindle and cystic kidney disease. *J Cell Biol*. 183:377-84.

Kapust, R.B., and D.S. Waugh. 1999. Escherichia coli maltose-binding protein is uncommonly effective at promoting the solubility of polypeptides to which it is fused. *Protein Sci*. 8:1668-74.

Karashima, T., D. Tsuruta, T. Hamada, N. Ishii, F. Ono, K. Hashikawa, B. Ohyama, Y. Natsuaki, S. Fukuda, H. Koga, R. Sogame, T. Nakama, T. Dainichi, and T. Hashimoto. 2012. Interaction of plectin and intermediate filaments. *J Dermatol Sci*. 66:44-50.

Kastner, B., N. Fischer, M.M. Golas, B. Sander, P. Dube, D. Boehringer, K. Hartmuth, J. Deckert, F. Hauer, E. Wolf, H. Uchtenhagen, H. Urlaub, F. Herzog, J.M. Peters, D. Poerschke, R. Lührmann, and H. Stark. 2008. GraFix: sample preparation for single-particle electron cryomicroscopy. *Nat Methods*. 5:53-5.

Keady, B.T., R. Samtani, K. Tobita, M. Tsuchya, J.T. San Agustin, J.A. Follit, J.A. Jonassen, R. Subramanian, C.W. Lo, and G.J. Pazour. 2012. IFT25 Links the Signal-Dependent Movement of Hedgehog Components to Intraflagellar Transport. *Dev Cell*. 22:940-51.

Kee, H.L., J.F. Dishinger, T. Lynne Blasius, C.J. Liu, B. Margolis, and K.J. Verhey. 2012. A size-exclusion permeability barrier and nucleoporins characterize a ciliary pore complex that regulates transport into cilia. *Nat Cell Biol*. 14:431-7.

Knispel, R.W., C. Kofler, M. Boicu, W. Baumeister, and S. Nickell. 2012. Blotting protein complexes from native gels to electron microscopy grids. *Nat Meth*. 9:182-4.

Kobayashi, T., K. Gengyo-Ando, T. Ishihara, I. Katsura, and S. Mitani. 2007. IFT-81 and IFT-74 are required for intraflagellar transport in C. elegans. *Genes Cells*. 12:593-602.

Koss-Harnes, D., B. Hoyheim, I. Anton-Lamprecht, A. Gjesti, R.S. Jorgensen, F.L. Jahnsen, B. Olaisen, G. Wiche, and T. Gedde-Dahl, Jr. 2002. A site-specific plectin mutation causes dominant epidermolysis bullosa simplex Ogna: two identical de novo mutations. *J Invest Dermatol*. 118:87-93.

Kozminski, K.G., P.L. Beech, and J.L. Rosenbaum. 1995. The Chlamydomonas kinesin-like protein FLA10 is involved in motility associated with the flagellar membrane. *J Cell Biol*. 131:1517-27.

Kozminski, K.G., K.A. Johnson, P. Forscher, and J. Rosenbaum. 1993. A motility in the eukaryotic flagellum unrelated to flagellar beating. *Proc Natl Acad Sci USA*. 90:5519-23.

Kramer-Zucker, A.G., F. Olale, C.J. Haycraft, B.K. Yoder, A.F. Schier, and I.A. Drummond. 2005. Cilia-driven fluid flow in the zebrafish pronephros, brain and Kupffer's vesicle is required for normal organogenesis. *Development*. 132:1907-1921.

Krock, B.L., and B.D. Perkins. 2008. The intraflagellar transport protein IFT57 is required for cilia maintenance and regulates IFT-particle-kinesin-II dissociation in vertebrate photoreceptors. *J Cell Sci*. 121:1907-15.

Kulaga, H.M., C.C. Leitch, E.R. Eichers, J.L. Badano, A. Lesemann, B.E. Hoskins, J.R. Lupski, P.L. Beales, R.R. Reed, and N. Katsanis. 2004. Loss of BBS proteins causes anosmia in humans and defects in olfactory cilia structure and function in the mouse. *Nat Genet*. 36:994-8.

Kunitomo, H., and Y. Iino. 2008. Caenorhabditis elegans DYF-11, an orthologue of mammalian Traf3ip1/MIP-T3, is required for sensory cilia formation. *Genes Cells*. 13:13-25.

Lechtreck, K.-F., S. Luro, J. Awata, and G.B. Witman. 2009. HA-tagging of putative flagellar proteins in Chlamydomonas reinhardtii identifies a novel protein of intraflagellar transport complex B. *Cell Motil Cytoskeleton*. 66:469-82.

Li, C., P.N. Inglis, C.C. Leitch, E. Efimenko, N.A. Zaghloul, C.A. Mok, E.E. Davis, N.J. Bialas, M.P. Healey, E. Héon, M. Zhen, P. Swoboda, N. Katsanis, and M.R. Leroux. 2008. An essential role for DYF-11/MIP-T3 in assembling functional intraflagellar transport complexes. *PLoS Genet*. 4:e1000044.

Liang, P., and T.H. MacRae. 1997. Molecular chaperones and the cytoskeleton. *J Cell Sci*. 110 (Pt 13):1431-40.

Liu, C.G., C. Maercker, M.J. Castanon, R. Hauptmann, and G. Wiche. 1996. Human plectin: organization of the gene, sequence analysis, and chromosome localization (8q24). *Proc Natl Acad Sci U S A*. 93:4278-83.

Lucker, B.F., R.H. Behal, H. Qin, L.C. Siron, W.D. Taggart, J. Rosenbaum, and D.G. Cole. 2005. Characterization of the intraflagellar transport complex B core: direct interaction of the IFT81 and IFT74/72 subunits. *J Biol Chem*. 280:27688-96.

Lucker, B.F., M.S. Miller, S.A. Dziedzic, P.T. Blackmarr, and D.G. Cole. 2010. Direct interactions of intraflagellar transport complex B proteins IFT88, IFT52 and IFT46. *J Biol Chem*.

Lunter, P.C., and G. Wiche. 2002. Direct binding of plectin to Fer kinase and negative regulation of its catalytic activity. *Biochem Biophys Res Commun*. 296:904-10.

Lupas, A., M. Van Dyke, and J. Stock. 1991. Predicting coiled coils from protein sequences. *Science*. 252:1162-1164.

Macnab, R.M. 2003. How bacteria assemble flagella. *Annu. Rev. Microbiol.* 57:77-100.

May-Simera, H.L., and M.W. Kelley. 2012. Cilia, Wnt signaling, and the cytoskeleton. *Cilia*. 1:7.

Mukhopadhyay, S., X. Wen, B. Chih, C.D. Nelson, W.S. Lane, S.J. Scales, and P.K. Jackson. 2010. TULP3 bridges the IFT-A complex and membrane phosphoinositides to promote trafficking of G protein-coupled receptors into primary cilia. *Genes Dev*. 24:2180-93.

Mykytyn, K., R.F. Mullins, M. Andrews, A.P. Chiang, R.E. Swiderski, B. Yang, T. Braun, T. Casavant, E.M. Stone, and V.C. Sheffield. 2004. Bardet-Biedl syndrome type 4 (BBS4)-null mice implicate Bbs4 in flagella formation but not global cilia assembly. *Proc Natl Acad Sci U S A*. 101:8664-9.

Nikolic, B., E. Mac Nulty, B. Mir, and G. Wiche. 1996. Basic amino acid residue cluster within nuclear targeting sequence motif is essential for cytoplasmic plectin-vimentin network junctions. *J Cell Biol*. 134:1455-67.

Nonaka, S., Y. Tanaka, Y. Okada, S. Takeda, A. Harada, Y. Kanai, M. Kido, and N. Hirokawa. 1998. Randomization of left-right asymmetry due to loss of nodal cilia generating leftward flow of extraembryonic fluid in mice lacking KIF3B motor protein. *Cell*. 95:829-37.

Oh, E.C., and N. Katsanis. 2012. Cilia in vertebrate development and disease. *Development*. 139:443-8.

Omori, Y., C. Zhao, A. Saras, S. Mukhopadhyay, W. Kim, T. Furukawa, P. Sengupta, A. Veraksa, and J. Malicki. 2008. Elipsa is an early determinant of ciliogenesis that links the IFT particle to membrane-associated small GTPase Rab8. *Nat Cell Biol*. 10:437-44.

Ortega, E., R.M. Buey, A. Sonnenberg, and J.M. de Pereda. 2011. The structure of the plakin domain of plectin reveals a non-canonical SH3 domain interacting with its fourth spectrin repeat. *J Biol Chem*. 286:12429-38.

Osmanagic-Myers, S., and G. Wiche. 2004. Plectin-RACK1 (receptor for activated C kinase 1) scaffolding: a novel mechanism to regulate protein kinase C activity. *J Biol Chem*. 279:18701-10.

Otto, E.A., B. Schermer, T. Obara, J.F. O'Toole, K.S. Hiller, A.M. Mueller, R.G. Ruf, J. Hoefele, F. Beekmann, D. Landau, J.W. Foreman, J.A. Goodship, T. Strachan, A. Kispert, M.T. Wolf, M.F. Gagnadoux, H. Nivet, C. Antignac, G. Walz, I.A. Drummond, T. Benzing, and F. Hildebrandt. 2003. Mutations in INVS encoding inversin cause nephronophthisis type 2, linking renal cystic disease to the function of primary cilia and left-right axis determination. *Nat Genet*. 34:413-20.

Ou, G., O.E. Blacque, J.J. Snow, M.R. Leroux, and J.M. Scholey. 2005. Functional coordination of intraflagellar transport motors. *Nature*. 436:583-7.

Pannier, M., S. Veit, A. Godt, G. Jeschke, and H.W. Spiess. 2000. Dead-time free measurement of dipole-dipole interactions between electron spins. *J Magn Reson*. 142:331-340.

Parisi, M.A., D. Doherty, P.F. Chance, and I.A. Glass. 2007. Joubert syndrome (and related disorders) (OMIM 213300). *Eur J Hum Genet*. 15:511-21.

Parker, J.D.K., L.K. Hilton, D.R. Diener, M.Q. Rasi, M.R. Mahjoub, J. Rosenbaum, and L.M. Quarmby. 2010. Centrioles are freed from cilia by severing prior to mitosis. *Cytoskeleton (Hoboken, NJ)*. 67:425-30.

Pazour, G.J., S.A. Baker, J.A. Deane, D.G. Cole, B.L. Dickert, J. Rosenbaum, G.B. Witman, and J.C. Besharse. 2002a. The intraflagellar transport protein,

IFT88, is essential for vertebrate photoreceptor assembly and maintenance. *J Cell Biol.* 157:103-13.

Pazour, G.J., and R.A. Bloodgood. 2008. Targeting proteins to the ciliary membrane. *Curr Top Dev Biol.* 85:115-49.

Pazour, G.J., B.L. Dickert, Y. Vucica, E.S. Seeley, J. Rosenbaum, G.B. Witman, and D.G. Cole. 2000. Chlamydomonas IFT88 and its mouse homologue, polycystic kidney disease gene tg737, are required for assembly of cilia and flagella. *J Cell Biol.* 151:709-18.

Pazour, G.J., B.L. Dickert, and G.B. Witman. 1999. The DHC1b (DHC2) isoform of cytoplasmic dynein is required for flagellar assembly. *J Cell Biol.* 144:473-81.

Pazour, G.J., J.T. San Agustin, J.A. Follit, J.L. Rosenbaum, and G.B. Witman. 2002b. Polycystin-2 localizes to kidney cilia and the ciliary level is elevated in orpk mice with polycystic kidney disease. *Current Biology.* 12:R378-80.

Pazour, G.J., and G.B. Witman. 2003. The vertebrate primary cilium is a sensory organelle. *Curr Opin Cell Biol.* 15:105-10.

Pedersen, L.B., M.S. Miller, S. Geimer, J.M. Leitch, J. Rosenbaum, and D.G. Cole. 2005. Chlamydomonas IFT172 is encoded by FLA11, interacts with CrEB1, and regulates IFT at the flagellar tip. *Current Biology.* 15:262-6.

Pfendner, E., F. Rouan, and J. Uitto. 2005. Progress in epidermolysis bullosa: the phenotypic spectrum of plectin mutations. *Exp Dermatol.* 14:241-9.

Pfendner, E., and J. Uitto. 2005. Plectin gene mutations can cause epidermolysis bullosa with pyloric atresia. *J Invest Dermatol.* 124:111-5.

Pigino, G., K.H. Bui, A. Maheshwari, P. Lupetti, D. Diener, and T. Ishikawa. 2011. Cryoelectron tomography of radial spokes in cilia and flagella. *J Cell Biol.* 195:673-87.

Pigino, G., S. Geimer, S. Lanzavecchia, E. Paccagnini, F. Cantele, D.R. Diener, J. Rosenbaum, and P. Lupetti. 2009. Electron-tomographic analysis of intraflagellar transport particle trains in situ. *J Cell Biol.* 187:135-48.

Piperno, G., and K. Mead. 1997. Transport of a novel complex in the cytoplasmic matrix of Chlamydomonas flagella. *Proc Natl Acad Sci U S A.* 94:4457-62.

Piperno, G., E. Siuda, S. Henderson, M. Segil, H. Vaananen, and M. Sassaroli. 1998. Distinct mutants of retrograde intraflagellar transport (IFT) share similar morphological and molecular defects. *J Cell Biol.* 143:1591-601.

Pytela, R., and G. Wiche. 1980. High molecular weight polypeptides (270,000-340,000) from cultured cells are related to hog brain microtubule-associated proteins but copurify with intermediate filaments. *Proc Natl Acad Sci U S A.* 77:4808-12.

Qin, H., D.T. Burnette, Y.-K. Bae, P. Forscher, M.M. Barr, and J. Rosenbaum. 2005. Intraflagellar transport is required for the vectorial movement of TRPV channels in the ciliary membrane. *Curr Biol*. 15:1695-9.

Qin, H., D.R. Diener, S. Geimer, D.G. Cole, and J. Rosenbaum. 2004. Intraflagellar transport (IFT) cargo: IFT transports flagellar precursors to the tip and turnover products to the cell body. *J Cell Biol*. 164:255-66.

Qin, H., J.L. Rosenbaum, and M.M. Barr. 2001. An autosomal recessive polycystic kidney disease gene homolog is involved in intraflagellar transport in C. elegans ciliated sensory neurons. *Curr Biol*. 11:457-61.

Qin, H., Z. Wang, D.R. Diener, and J. Rosenbaum. 2007. Intraflagellar transport protein 27 is a small G protein involved in cell-cycle control. *Curr Biol*. 17:193-202.

Raja, M., and E. Vales. 2011. Improved technique for reconstituting incredibly high and soluble amounts of tetrameric K(+) channel in natural membranes. *J Membr Biol*. 241:141-4.

Ratelade, J., M.C. Miot, E. Johnson, J.M. Betton, P. Mazodier, and N. Benaroudj. 2009. Production of recombinant proteins in the lon-deficient BL21(DE3) strain of Escherichia coli in the absence of the DnaK chaperone. *Appl Environ Microbiol*. 75:3803-7.

Reese, T.S. 1965. Olfactory Cilia in the frog. *Journal of Cell Biology*. 25:209-230.

Rezniczek, G.A., C. Abrahamsberg, P. Fuchs, D. Spazierer, and G. Wiche. 2003. Plectin 5'-transcript diversity: short alternative sequences determine stability of gene products, initiation of translation and subcellular localization of isoforms. *Hum Mol Genet*. 12:3181-94.

Rezniczek, G.A., J.M. de Pereda, S. Reipert, and G. Wiche. 1998. Linking integrin alpha6beta4-based cell adhesion to the intermediate filament cytoskeleton: direct interaction between the beta4 subunit and plectin at multiple molecular sites. *J Cell Biol*. 141:209-25.

Rial, D.V., and E.A. Ceccarelli. 2002. Removal of DnaK contamination during fusion protein purifications. *Protein Expression and Purification*. 25:503-7.

Ringo, D.L. 1967. Flagellar motion and fine structure of the flagellar apparatus in Chlamydomonas. *J Cell Biol*. 33:543-71.

Rix, S., A. Calmont, P.J. Scambler, and P.L. Beales. 2011. An Ift80 mouse model of short rib polydactyly syndromes shows defects in hedgehog signalling without loss or malformation of cilia. *Hum Mol Genet*. 20:1306-14.

Robert, A., G. Margall-Ducos, J.E. Guidotti, O. Bregerie, C. Celati, C. Brechot, and C. Desdouets. 2007. The intraflagellar transport component IFT88/polaris is a

centrosomal protein regulating G1-S transition in non-ciliated cells. *J Cell Sci.* 120:628-37.

Rosenbaum, J., and G.B. Witman. 2002. Intraflagellar transport. *Nat Rev Mol Cell Biol.* 3:813-25.

Satir, P. 1995. Landmarks in cilia research from Leeuwenhoek to us. *Cell Motility and Cytoskeleton.* 32:90-94.

Satir, P., and S.T. Christensen. 2007. Overview of structure and function of mammalian cilia. *Annu Rev Physiol.* 69:377-400.

Satir, P., and S.T. Christensen. 2008. Structure and function of mammalian cilia. *Histochem Cell Biol.* 129:687-93.

Schafer, J.C., M.E. Winkelbauer, C.L. Williams, C.J. Haycraft, R.A. Desmond, and B.K. Yoder. 2006. IFTA-2 is a conserved cilia protein involved in pathways regulating longevity and dauer formation in Caenorhabditis elegans. *J Cell Sci.* 119:4088-100.

Sedmak, T., and U. Wolfrum. 2010. Intraflagellar transport molecules in ciliary and nonciliary cells of the retina. *J Cell Biol.* 189:171-86.

Seifert, G.J., D. Lawson, and G. Wiche. 1992. Immunolocalization of the intermediate filament-associated protein plectin at focal contacts and actin stress fibers. *Eur J Cell Biol.* 59:138-47.

Sevcik, J., L. Urbanikova, J. Kost'an, L. Janda, and G. Wiche. 2004. Actin-binding domain of mouse plectin. Crystal structure and binding to vimentin. *Eur J Biochem.* 271:1873-84.

Shah, A.S., Y. Ben-Shahar, T.O. Moninger, J.N. Kline, and M.J. Welsh. 2009. Motile cilia of human airway epithelia are chemosensory. *Science.* 325:1131-1134.

Shapiro, J., J. Ingram, and K.A. Johnson. 2005. Characterization of a molecular chaperone present in the eukaryotic flagellum. *Eukaryot Cell.* 4:1591-4.

Shinkuma, S., J.R. McMillan, and H. Shimizu. 2011. Ultrastructure and molecular pathogenesis of epidermolysis bullosa. *Clin Dermatol.* 29:412-9.

Signor, D., K.P. Wedaman, L.S. Rose, and J.M. Scholey. 1999. Two heteromeric kinesin complexes in chemosensory neurons and sensory cilia of Caenorhabditis elegans. *Mol Biol Cell.* 10:345-60.

Silflow, C.D., X. Sun, N.A. Haas, J.W. Foley, and P.A. Lefebvre. 2011. The Hsp70 and Hsp40 chaperones influence microtubule stability in Chlamydomonas. *Genetics.* 189:1249-60.

Silva, D.A., X. Huang, R.H. Behal, D.G. Cole, and H. Qin. 2011. The RABL5 homolog IFT22 regulates the cellular pool size and the amount of IFT particles

partitioned to the flagellar compartment in Chlamydomonas reinhardtii. *Cytoskeleton (Hoboken, NJ)*.

Silverman, M.A., and M.R. Leroux. 2009. Intraflagellar transport and the generation of dynamic, structurally and functionally diverse cilia. *Trends in Cell Biology*. 19:306-16.

Sonnenberg, A., A.M. Rojas, and J.M. de Pereda. 2007. The structure of a tandem pair of spectrin repeats of plectin reveals a modular organization of the plakin domain. *J Mol Biol*. 368:1379-91.

Sorokin, S. 1962. Centrioles and the formation of rudimentary cilia by fibroblasts and smooth muscle cells. *J Cell Biol*. 15:363-77.

Sorokin, S.P. 1968. Reconstructions of centriole formation and ciliogenesis in mammalian lungs. *J Cell Sci*. 3:207-30.

Steinböck, F.A., and G. Wiche. 1999. Plectin: a cytolinker by design. *Biol Chem*. 380:151-8.

Steinhoff, H.-J. 2002. Methods for study of protein dynamics and protein-protein interaction in protein-ubiquitination by electron paramagnetic resonance spectroscopy. *Front Biosci*. 7:c97-110.

Steinhoff, H.J., N. Radzwill, W. Thevis, V. Lenz, D. Brandenburg, A. Antson, G. Dodson, and A. Wollmer. 1997. Determination of interspin distances between spin labels attached to insulin: comparison of electron paramagnetic resonance data with the X-ray structure. *Biophys J*. 73:3287-98.

Svitkina, T.M., A.B. Verkhovsky, and G.G. Borisy. 1996. Plectin sidearms mediate interaction of intermediate filaments with microtubules and other components of the cytoskeleton. *J Cell Biol*. 135:991-1007.

Taschner, M., S. Bhogaraju, and E. Lorentzen. 2011. Architecture and function of IFT complex proteins in ciliogenesis. *Differentiation; research in biological diversity*.

Taylor, C.M., and A.E. Keating. 2005. Orientation and oligomerization specificity of the Bcr coiled-coil oligomerization domain. *Biochemistry*. 44:16246-56.

Terwilliger, T.C., P.D. Adams, R.J. Read, A.J. McCoy, N.W. Moriarty, R.W. Grosse-Kunstleve, P.V. Afonine, P.H. Zwart, and L.W. Hung. 2009. Decision-making in structure solution using Bayesian estimates of map quality: the PHENIX AutoSol wizard. *Acta Crystallogr D Biol Crystallogr*. 65:582-601.

Tsuruta, D., T. Hashimoto, K.J. Hamill, and J.C. Jones. 2011. Hemidesmosomes and focal contact proteins: functions and cross-talk in keratinocytes, bullous diseases and wound healing. *J Dermatol Sci*. 62:1-7.

Tyler, K.M., A. Fridberg, K.M. Toriello, C.L. Olson, J.A. Cieslak, T.L. Hazlett, and D.M. Engman. 2009. Flagellar membrane localization via association with lipid rafts. *J Cell Sci*. 122:859-66.

Uitto, J., and G. Richard. 2004. Progress in epidermolysis bullosa: genetic classification and clinical implications. *Am J Med Genet C Semin Med Genet*. 131C:61-74.

Urbanikova, L., L. Janda, A. Popov, G. Wiche, and J. Sevcik. 2002. Purification, crystallization and preliminary X-ray analysis of the plectin actin-binding domain. *Acta Crystallogr D Biol Crystallogr*. 58:1368-70.

Wagschal, K., B. Tripet, P. Lavigne, C. Mant, and R.S. Hodges. 1999. The role of position a in determining the stability and oligomerization state of alpha-helical coiled coils: 20 amino acid stability coefficients in the hydrophobic core of proteins. *Protein Sci*. 8:2312-29.

Walko, G., N. Vukasinovic, K. Gross, I. Fischer, S. Sibitz, P. Fuchs, S. Reipert, U. Jungwirth, W. Berger, U. Salzer, O. Carugo, M.J. Castañón, and G. Wiche. 2011. Targeted proteolysis of plectin isoform 1a accounts for hemidesmosome dysfunction in mice mimicking the dominant skin blistering disease EBS-Ogna. *PLoS Genet*. 7:e1002396.

Walter, T.S., C. Meier, R. Assenberg, K.-F. Au, J. Ren, A. Verma, J.E. Nettleship, R.J. Owens, D.I. Stuart, and J.M. Grimes. 2006. Lysine methylation as a routine rescue strategy for protein crystallization. *Structure*. 14:1617-22.

Wang, Z., Z.-C. Fan, S.M. Williamson, and H. Qin. 2009. Intraflagellar transport (IFT) protein IFT25 is a phosphoprotein component of IFT complex B and physically interacts with IFT27 in Chlamydomonas. *PLoS ONE*. 4:e5384.

Wiche, G. 1989. Plectin: general overview and appraisal of its potential role as a subunit protein of the cytomatrix. *Crit Rev Biochem Mol Biol*. 24:41-67.

Wiche, G. 1998. Role of plectin in cytoskeleton organization and dynamics. *J Cell Sci*. 111 (Pt 17):2477-86.

Wiche, G., D. Gromov, A. Donovan, M.J. Castanon, and E. Fuchs. 1993. Expression of plectin mutant cDNA in cultured cells indicates a role of COOH-terminal domain in intermediate filament association. *J Cell Biol*. 121:607-19.

Wiche, G., R. Krepler, U. Artlieb, R. Pytela, and H. Denk. 1983. Occurrence and immunolocalization of plectin in tissues. *J Cell Biol*. 97:887-901.

Wiche, G., and L. Winter. 2011. Plectin isoforms as organizers of intermediate filament cytoarchitecture. *Bioarchitecture*. 1:14-20.

Witman, G.B., J. Plummer, and G. Sander. 1978. Chlamydomonas flagellar mutants lacking radial spokes and central tubules. Structure, composition, and function of specific axonemal components. *J Cell Biol*. 76:729-47.

Yoder, B.K., X. Hou, and L.M. Guay-Woodford. 2002. The polycystic kidney disease proteins, polycystin-1, polycystin-2, polaris, and cystin, are co-localized in renal cilia. *J Am Soc Nephrol*. 13:2508-16.

9   Appendix A: Bioinformatic tools & Databases

BLAST   http://blast.ncbi.nlm.nih.gov/Blast.cgi

Coils   http://www.ch.embnet.org/software/COILS_form.html

EMBOSS Transseq   http://www.ebi.ac.uk/Tools/st/emboss_transeq/

MultAlin   http://multalin.toulouse.inra.fr/multalin/multalin.html

PSIPRED v3.0   http://bioinf.cs.ucl.ac.uk/psipred/

ProtParam   http://web.expasy.org/protparam/

Protein data bank   http://www.pdb.org/pdb/home/home.do

PubMed   http://www.ncbi.nlm.nih.gov/pubmed/

Sequence Editor   http://www.fr33.net/seqedit.php

10 Appendix B: *Curriculum Vitae*

PERSONAL DATA

Name	Mag. Clara Pleban
Address	Grünentorgasse 2/9, 1090 Wien
Telephone	0650 217 44 41
E-Mail	*clara.pleban@univie.ac.at*
Nationality	Austria
Date of Birth	12. January 1983

EDUCATION

Date	*August 2008 – October 2012*
Type of Education	**University/PhD in Molecular Biology**
Institute	Max F. Perutz Laboratories
Details	
	Supervisor: **Dr. Gang Dong**

Date	*Oktober 2001 - April 2007*
Type of Education	**University/Master in Molecular Biology**
Institute	University of Vienna
Details	Study of Molecular Biology
	Specialized in:
	Biochemistry, Bioinformatic/Structural Biology, Organic Chemistry
Graduation	with **Honors**
Diploma Thesis	"Bioinformatische Markerproteinidentifikation aus genomischen Daten" (Bioinformatics-based identification of marker proteins based on genomic data)
	Supervisor: Dr. Bernd Mayer

Date	*September 1993 – June 2001*
Institute	Lise-Meitner Bundesrealgymnasium
Graduation	A-levels with Honors

INTERNSHIP AND RELATED EXPERIENCES

Date	*April 2007 – July 2007*
Type	**Scientific Collaboration Project**
Company	emergentec
Details	Analysis of gene expression data with the help of bioinformatic methods

Date	*November 2005 – May 2007*
Type	**Tutor**
Institute	University of Vienna
Field of action	Organic-chemistry course for molecular biologists
Details	Due to my specialization on organic chemistry I was offered the change to work as a tutor for the "Organic chemistry course for molecular biologists".

Date	*August 2001*
Type	**Internship in a Pharmacy**
Company	Apotheke im Hatlerdorf, Dornbirn, Vorarlberg
Field of Action	Ordering of Medicaments, Lab work

Date	*1997 - 2001*
Type	**Coaching**
Field	Mathematics, Physics, Chemistry
Details	During the last four years of school I was coaching fellow students in math, physics and chemistry.

PERSONAL SKILLS AND COMPETENCES

First Language	German
Other Languages	English: Fluently
	Spanish: Basic Knowledge
EDV Knowledge	OS Systems MacIntosh, Windows, Linux
	Office Programs MS Office (Word, Excel, Powerpoint)
	Open Office

Other	Adobe Suite (Illustrator, Photoshop)
Programming Language	Basic Python

PUBLICATIONS AND CONGRESS CONTRIBUTION

Congress Contribution	Poster **"Cloning and characterization of *Trypanosoma brucei* IFT complex B core"**/ Cilia in Development and Disease, Cilia 2012; London, UK; 16. – 18. May 2012
Workshop	**LRZ Life-Science Molecular Modeling Workshop and Demo**/ Munich, Germany; February 2012
Workshop	EMBO Course **"Structural Characterization of macromolecular complexes"**/ Grenoble, France; 31.May - 5. June 2010
Reference	Aydin S, Signorelli S, Lechleitner T, Joannidis M, Perco P, Pleban C, Pfaller W, and Jennings P: **The influence of microvascular endothelial cells on transcriptional regulation of proximal tubular epithelial cells.** *Am J Physiol Cell Physiol 2008 Feb*, **294**(2):C543-54
Reference	Perco P, Pleban C, Kainz A, Lukas A, Mayer G, Mayer B, Oberbauer R: **Protein Biomarkers associated with acute renal failure and chronic kidney disease.** *Eur J Clin Invest* 2006, **36**(11): 753-763
Reference	Perco P, Pleban C, Kainz A, Lukas A, Mayer B, Oberbauer R: **Gene expression and biomarkers in renal transplant ischemia reperfusion injury.** *Transplant International* 2007, **20**(1): 2-11
Congress	"Evolution of Biomolecular Structure" Universität Wien; Mai 2006